

République Algérienne Démocratique et Populaire
Ministère de l'Enseignement Supérieur et de la Recherche Scientifique
Université des Sciences et de Technologie d'Oran Mohamed Boudiaf



Faculté de Génie Électrique

Département d'Électronique

Thèse

Présentée en vue de l'obtention du diplôme de Doctorat d'État

Spécialité : Systèmes Photovoltaïques

Présentée par

MOKEDDEM Abdelmalek

Intitulée

**Pompage d'Eau par Énergie Photovoltaïque :
Expérimentation et Simulation**

Soutenue le, 03/07/ 2012, devant le jury composé de :

HAMZAOUI Saad	Président	Pr. USTO-MB
MIDOUN Abdelhamid	Rapporteur	Pr. USTO-MB
ABIDRI Boualem	Examinateur	Pr. UDL-SBA
HIADSI Said	Examinateur	Pr. USTO-MB
KHALDI Abdelkrim	Examinateur	MCA. USTO-MB

Photovoltaic Water pumping Experimentation and Simulation

by

ABDELMALEK MOKEDDEM

A thesis submitted in partial fulfillment of the
requirements for the degree of

DOCTORAT D'ETAT
Option: Systemes Photovoltaïques

at the

UNIVERSITY OF SCIENCE AND
TECHNOLOGY-MB – ORAN

2012

Abstract

This research evaluated the experimental study carried out to investigate the performance of a simple, directly coupled dc photovoltaic (PV) powered water pumping system. The system comprises of a 1.5 kWp PV array, D.C. motor and a centrifugal pump. The centrifugal pump is from local market and designed for fixed voltage. The D.C. motor is of permanent magnet brushed type used for educational purposes. As part of this research a working directly coupled PV water pumping system is produced. The experiment was conducted under a variable dc power source with the aim of calculating different motor parameters and all measuring equipment calibration. The system was tested and monitored for its performance outdoor for short periods under different climatic conditions and varying solar irradiance and ambient temperature with two static head configurations. A second objective was to model one by one all components of the PV water pumping system to describe its performance. The calculated flow rate, head generated by the pump and the efficiency of the system as function of solar irradiance and time were compared with field-measured data. The performance of the system is assessed using field data recorded at USTO. The centrifugal pump operation is analyzed by the torque equation and its variations as a function of the rotational speed and flow rate. The pump had to be dismantled for its impeller parameters and dimensions. The recorded hourly solar irradiance at UST Oran site are arranged into four clusters representing four types of sky conditions for every month of the year. An unsupervised neural network clustering method is used (Self Organizing Map). No attempt is made to estimate the solar irradiance since the issue was previously treated by the author (in previous research work), but also because professional

softwares are fairly available via World Wide Web (SoDa). Although the motor-pump efficiency did not exceed 30%, which is typical for directly-coupled photovoltaic pumping systems, such a system is clearly suitable for low head irrigation in the remote areas, not connected to the national grid and where access to water comes as first priority issue than access to technology. The system operates without battery and complex electronic control, therefore not only the initial cost is low but also maintenance, repairing and replacement cost can be saved. The study showed that directly coupled system attains steady state soon after any abrupt change. The increasing need for water pumping, especially for irrigation and domestic use in arid and remote areas (Sahara, steppes), together with the rising fuel costs, encouraged the development of photovoltaic water pumps.

Acknowledgments

I dedicate this work to the four women who mean the most to me, my mother, my wife and my two daughters Afnène and Moona .

I would like to thank my advisor, Professor Abdelhamid Midoun for his support and encouragement but above all for his patience with me.

I wish to acknowledge Power Electronic and Solar Energy Laboratory for providing the funding to build the pumping test rig.

I want to thank all members of Professor Midoun team within the Power Electronic and Solar Energy Laboratory (Room 9221) for their support and encouragements.

Lastly, I owe special thanks to my friends and colleagues of the department of physics for helping the best way they could.

Table of Contents

Abstract.....	i
Acknowledgments.....	iii
Table of Contents.....	iv
List of Figures.....	viii
List of Tables.....	xvii
Nomenclature.....	xviii
1.0 INTRODUCTION.....	1
1.1 Background.....	1
1.2 Literature review.....	2
1.3 Objectives and perspectives.....	5
2.0 PHOVOLTAIC PUMPING SYSTEMS.....	8
2.1 Introduction.....	8
2.2 Photovoltaic Technologies.....	10
2.2.1 Photovoltaic cell production.....	12
2.2.2 Photovoltaic cell performance.....	14
2.3 Motor-Pump Subsystem.....	17
2.3.1 D.C. motor technology.....	19
2.3.2 Pump technology.....	21
2.3.3 Pumping system configurations.....	23
3.0 SOLAR RADIATION DATA MEASUREMENTS.....	25
3.1 Introduction.....	25

3.2 Components of solar radiation.....	25
3.3 Measurements of solar radiation.....	28
3.3.1 Typical meteorological year.....	30
3.3.2 Neural network solar data clustering.....	33
4.0 PHOTOVOLTAIC CELL (MODULE) PERFORMANCE MODEL DESCRIPTION.....	43
4.1 Introduction.....	43
4.2 Electrical circuit modeling.....	43
4.2.1 Photovoltaic effect basics.....	43
4.2.2 Photovoltaic solar cell equivalent circuit.....	46
4.2.3 Series resistance effects.....	51
4.2.4 Shunt resistance effects.....	52
4.2.5 High temperature effect on PV cell performance.....	54
4.3 Photovoltaic cell (module) performance final Model.....	57
5.0 D.C. MOTOR PERFORMANCE MODELING.....	61
5.1 Introduction.....	61
5.2 D.C. motor theory.....	61
5.2.1 Motor torque constant.....	63
5.2.2 Rotational speed constant (or back e.m.f constant).....	64
5.3 Motor performance.....	65

5.3.1 Rotational speed characteristic.....	66
5.3.2 Rotational speed torque characteristic.....	66
5.3.3 Calculation of K_{Tp} and K_{Sp}	67
5.4 D.C. motor and PV array direct coupling.....	67
5.4.1 Optimum load matching in direct coupled PV systems.....	71
6.0 CENTRIFUGAL PUMP PERFORMANCE MODELING.....	77
6.1 Introduction.....	77
6.2 Pump characteristic.....	77
6.2.1 Total head produced by the pump.....	77
6.2.1.1 Velocities triangles.....	79
6.2.1.2 Ideal head equation.....	80
6.2.1.3 Actual head equation.....	81
6.2.2 Pump torque.....	84
6.3 Hydraulic system head and operating Point.....	86
7.0 PV PUMPING SYSTEM FINAL MODEL AND EXPERIMENTAL TESTING.....	92
7.1 Introduction.....	92
7.2 Methodology.....	92
7.3 Components parameters measurements.....	100
7.3.1 The PV array characteristics.....	101

7.3.2 The D.C. motor characteristics measurements.....	103
7.3.3 The centrifugal pump characteristics.....	104
7.4 The experimental test bench.....	106
7.5 Testing procedure and analysis.....	110
GENERAL CONCLUSIONS AND PERSPECTIVES.....	123
REFERENCES.....	126

List of Figures

- Figure 2.1** Graph showing component costs of PV system and price reduction over time. (IEA PVPS, annual report 2008).....
- Figure 2.2 Energy band concepts diagram.(Twidell.JW, AD. Weir, 1986).....
- Figure 2.3 Spectral distribution of extraterrestrial solar radiation and spectral response of a silicon solar cell (Duffie.JA, WA. Beckman, 1980).....
- Figure 2.4 A monocrystalline silicon cell (left) (Xinchang, 2009), a polycrystalline silicon cell (middle) (Xinchang, 2009), and a thin-film amorphous silicon module (right) (not to scale) (Kaneka, 2009).....
- Figure 2.5 Research cell efficiencies of various technologies and their progression over the previous thirty years (Nozik, 2005).....
- Figure 2.6 I-V characteristic of a photovoltaic module at a given irradiance and cell temperature (Duffie. JA, WA. Beckman, 2006).....
- Figure 2.7 I-V characteristics a Kyocera LA 361 K 51 Module at different solar irradiance values and given temperature (PVSYST V5_0, 2011).....

- Figure 2.8 Power against voltage of a Kyocera LA 361 K 51 Module at different solar irradiance values and given temperature, with maximum power line(PVSYST V5_0, 2011).....
- Figure 2.9 Photovoltaic array I-V characteristics for different irradiance levels with the locus of operating points (load curve)(recorded at USTO).....
- Figure 2.10 D.C. motors construction (a) brushed D.C. motor
(b) brushless D.C. motor
(www.Orientalmotor.com).....
- Figure 2.11 Typical centrifugal pump characteristics (Halcrow.W, 1981).....
- Figure 2.12 Submerged multistage centrifugal motor pumpset.....
- Figure 2.13 Submerged pump with surface mounted motor.....
- Figure 2.14 Reciprocating positive displacement pump.....
- Figure 2.15 Floating motor pump sets.....
- Figure 2.16 Surface suction pump sets.....
- Figure 3.1 Schematic illustration of solar radiation components.....
- Figure 3.2 Mean hourly irradiance measured and estimated (SoDa).....
- Figure 3.3 Mean hourly irradiance measured against estimated (SoDa).....

- Figure 3.4 Typical solar irradiance measurements at USTO adopted from (Mokeddem. A et al, 2007).....
- Figure 3.5 Monthly averaged daily total irradiation for January (Std.dev=0.23), in [KJ/m²/day]x10⁻⁴
- Figure 3.6 The architecture of a 4x5 SOM
- Figure 3.7 BMU adaptation to its neighborhood.....
- Figure 3.8 Diurnal patterns of global irradiation (4 clusters), December.....
- Figure 3.9 Diurnal patterns of global irradiation (4 clusters), February.....
- Figure 3.10 Diurnal patterns of global irradiation (4 clusters), June.....
- Figure 3.11 Diurnal patterns of global irradiation (4 clusters), September.....
- Figure 3.12 Diurnal patterns of global irradiation (4 clusters), May.....
- Figure 3.13 (a) Solar irradiation distribution for cluster1 box chart, May.....
- Figure 3.13 (b) Solar irradiation distribution for cluster2 box chart, May.....
- Figure 4.1 Spectral distributions of solar irradiance received above the atmosphere and at sea level, about half the irradiance occurs in the visible region (0.4–0.7μm) (Duffie and Beckman, 2006).....

- Figure 4.2(a) Physical set-up of a solar cell. (b) Photovoltaic p-n junction characteristic (Twidell.JW, AD. Weir, 2006).....
- Figure 4.3 Ideal photovoltaic solar cell model (Twidell.JW, AD. Weir, 2006).....
- Figure 4.4 Photovoltaic solar cell equivalent circuit (Twidell.JW, AD. Weir, 2006).....
- Figure 4.5 Typical I-V characteristic of a Silicon module (Kyocera LA361 K 51 manufacturer data sheet)....
- Figure 4.6 Short circuit current versus solar irradiance at two R_S Values (Wolf.M, H. Rauschenbach, 1963).....
- Figure 4.7 Series resistance effect on PV characteristic (simulation).....
- Figure 4.8 Effect of series resistance on Kyocera LA 361K51 module(Manufacturer test data sheet).....
- Figure 4.9 Schematic illustration of the fill factor.....
- Figure 4.10 Effect of R_S and R_{Sh} on cell characteristic and on fill factor in particular (National Instruments LabVIEW for photovoltaic Solar Cell characterization web site).....
- Figure 4.11 Solar cells theoretical efficiency versus band gap at 25 °C and 100 °C (Twidell. JW, AD. Weir, 2006).....

Figure 4.12	Temperature effect on open circuit voltage (array scale).....
Figure 4.13	I-V characteristics for different temperatures (simulation).....
Figure 4.14	Array temperature against irradiance (recorded at USTO).....
Figure 5.1	Equivalent circuit of a DC motor.....
Figure 5.2	Motor rotational speed-torque characteristics $R_a=2.8 \Omega$ (simulation).....
Figure 5.3	Motor speed-torque characteristics for two different values of armature resistance (simulation).....
Figure 5.4	Motor speed-torque characteristics for constant voltage source (simulation).....
Figure 5.5	Electrical plan showing relative position of load line to the maximum power line, $R_a=2.4$ (Thesis simulation).....
Figure 5.6	I-V characteristic of Kyocera module, locus of maximum power region is represented by the vertical dashed lines (Thesis simulation).....
Figure 5.7	I-V characteristics and load curves for three values of motor armature resistance (Thesis simulation)
Figure 6.1	A centrifugal pump radial impeller (adopted from Grundfos technical sheet).....

Figure 6.2	Velocity triangles positioned at the impeller inlet and outlet (adopted from Grundfos technical sheet).....
Figure 6.3	Velocities triangle at the impeller inlet.....
Figure 6.4	Pump and system characteristics.....
Figure 6.5	Moody chart showing friction factor k_f as function of Reynold's number and surface roughness for laminar and turbulent flows (adopted from Grundfos technical sheet).....
Figure 7.1	PV pumping system performance curves (Mokeddem.A et al, 2011).....
Figure 7.2	Photovoltaic pumping system model block diagram.....
Figure 7.3	PV pumping system calculation structure
Figure 7.4	sub-system efficiency for two static heads (recorded at USTO).....
Figure 7.5	PV supply and fixed power supply performance comparison (recorded at USTO).....
Figure 7.6	Load curve for two system configurations (recorded at USTO).....
Figure 7.7	Predicted against measured load curve (recorded at USTO).....

Figure 7.8	Predicted against measured flow rate values (recorded at USTO).....
Figure 7.9	Predicted values of flow rate for two hydraulic system configurations (simulation).....
Figure 7.10	PV array insulation measuring equipment on top of roof at University of Science & Technology of Oran.....
Figure 7.11	IV curve fitting for a clear day recorded at UST Oran.....
Figure 7.12	DC motor (LEROY SOMER) elements.....
Figure 7.13	Centrifugal pump used in this work (ELECTROPOMP ECM100) all dimensions in mm.....
Figure 7.14	Manufacturer pump characteristics.....
Figure 7.15	Schematic diagram of the closed loop test bench at UST Oran.....
Figure 7.16	pressure transmitter 7 MF 1563 all dimensions in mm (inch).....
Figure 7.17	Flow rate Kobold DF dimensions.....
Figure 7.18	Flow meter calibration graph.....
Figure 7.19	Daily solar irradiance recorded at UST Oran.....

- Figure 7.20 a Daily mean solar irradiation distribution over a year recorded at UST Oran.....
- Figure 7.20b Daily mean solar irradiation distribution for a Typical Meteorological Year recorded at UST Oran.....
- Figure 7.21 I-V characteristics of the PV array measured at UST Oran.....
- Figure 7.22 Daily flow rate for two static heads (Mokeddem. A et al, 2011).....
- Figure 7.23 Flow rate variation with power motor-pump power input (Mokeddem. A et al, 2011).....
- Figure 7.24(a) Flow rate versus solar irradiance (recorded at USTO).....
- Figure 7.24(b) Flow rate versus solar irradiance (recorded at USTO).....
- Figure 7.25 Motor-pump flow rate versus operating voltage (Mokeddem. A et al, 2011).....
- Figure 7.26(a) Pump head developed as function of the motor voltage input (recorded at USTO).....
- Figure 7.26(b) Pump head developed as function of the motor voltage input (recorded at USTO).....
- Figure 7.27 Subsystem efficiency as function of the power input Mokeddem. A et al, 2011).....

Figure 7.28 Flow rate versus rotational speed comparison with
(Benlarbi et al, 2004).....

Liste of Tables

Table 1.1	Solar energy potentials in Algeria.....
Table 2.1	Motor efficiencies (less than 1 kW of power) (Smith.D.V, Allison.S.V, 1978).....
Table 3.1	Solar radiation components techniques of measurement (Twidell. JW, Weir. AD, 2006).....
Table 4.1	Characteristics of PV module "KYOCERA LA 361K51" at Standard Conditions (25°C,1000 W/m²).....
Table 5.1	Utilization factor $\eta = P_{in}/P_{max}$
Table 6.1	Head loss coefficients for a range of pipe fitting (Douglas. JF, Gasiorek. JM, Swaffield. JA, 1985)...
Table 7.1	Measuring instruments and their approximate accuracy.....

Nomenclature

A	Diode factor (-)
B	Magnetic flux density (Tesla)
C	Absolute velocity of water (m/s)
	Curve-fitting constant (V)
C_u	Tangential component of absolute velocity of water (m/s)
C_r	Radial component of the absolute velocity of water (m/s)
D	Pump impeller diameter (m)
E	Electromotive force generated in the conductor (V)
E_g	Band gap (eV)
FF	Fill factor (-)
G	The effective irradiance (kW/m^2)
H	Actual head developed by the pump (m)
H_{ST}	Static head (m)
H_{vir}	Virtual head for finite number of blades (m)
$H_{vir,\infty}$	Virtual head for an infinite number of blades (m)
I	Cell terminal current, load current (A)
I_0	Saturation current (A)
I_a	Motor armature current (A)
I_D	Dark current (diode) (A)
I_g	Generation current (A)
I_L	Light (photon)-generated current (A)
I_{MP}	Current corresponding to maximum power point (A)
I_r	Recombination current (A)
I_{OP}	Optimum current corresponding to the maximum power point (A)
I_{oc}	Cell short circuit current (A)
K_m	Pump impeller dimensions constant (Kgm^2)
K_{SP}	Motor rotational speed constant (Vs/rad)

K_{TP}	Motor torque constant (Nm/A)
L	Effective length of the conductor (m)
M_P	Pump impeller torque (Nm)
P_{max}	Maximum power that can the array deliver (W)
P_P	Pfleiderer correction factor (-)
Q	Flow rate (m^3/s)
R	Pump impeller radius, motor-rotor shaft (m)
R_a	Motor armature resistance (Ω)
R_e	Reynolds number (-)
R_S	Series resistance (Ω)
R_{sh}	Parallel (shunt) resistance (Ω)
T	Absolute temperature (K)
T_a	Ambient temperature (K)
T_c	Cell temperature ($^{\circ}C$)
T_L	Load torque (Nm)
T_M	Motor torque (Nm)
T_{SP}	Torque at stall condition (Nm)
U	Pump impeller tangential velocity (m/s)
V	Cell terminal voltage (V)
V_M	Voltage supplied to the motor (V)
V_{MP}	Voltage corresponding to maximum power point (V)
V_{oc}	Open-circuit voltage (V)
V_{op}	Optimum voltage corresponding to maximum power point (V)
V	Array terminal voltage (V)
W	Velocity of water relative to pump impeller (m/s)
Z	Total number of conductors (-)

Lower case letters

b	Impeller width (m)
d	Pipe internal diameter (m)

e	Charge of electron (1.6×10^{-19} C)
h	Planck constant (6.63×10^{-34} Js)
h_f	Hydraulic system resistive head (m)
k	Boltzmann constant (1.3854×10^{-23} J/K)
k_f	Friction factor (-)
l	Pipe length (m)
v	Speed (m/s)
z	Final number of impeller blades (-)

Greek letters

α	Blade angle formed by C and U (degree)
a	Short circuit current temperature coefficient (mA/°C)
β	Blade angle formed by W and U (degree)
β	Slope (tilt) angle (degree)
β	Open-circuit voltage coefficient (mV/°C)
ω	Rotor rotational speed (rad/s)
ω_0	Ideal no-load rotational speed (rad/s)
Φ	Electric potential difference between the Fermi level and the valence or conduction band as appropriate (V)
ϵ_p	Pump head correction factor (-)
η	Array utilization factor (P_{IN}/P_{MAX}) (-)
η_h	Pump hydraulic efficiency (-)
λ	Light wavelength of (μm)
ν	Frequency (1/s)
ρ	Water density (kg/m^3)

Subscript

1,2	Pump inlet and outlet (-)
-----	---------------------------

CHAPTER 1.0

INTRODUCTION

1.1 Background

The global demand for energy and more specifically clean energy is growing rapidly. Renewable energies are harmless to health and without pollution for the environment. The international community recognizes the vital importance of renewable energies, the actual total cost of renewable energy remains high compared to fossil fuels, although it continues to fall. World energy use increased more than tenfold over the 20th century, predominantly from fossil fuels (i.e. coal, oil and gas) and with the addition of electricity from nuclear power. In the 21st century, further increases in world energy consumption can be expected, much for rising industrialization and demand in previously less developed countries, aggravated by gross inefficiencies in all countries. Whatever the energy source, there is an overriding need for efficient generation and use of energy.

Increasing the global share of renewable energy would not only bring environmental benefits, but also enhance overall energy security by diversifying energy supply. There, the concept of sustainable development has taken all its importance. Sustainable development can be broadly defined as living, producing and consuming in a manner that meets the needs of the present without compromising the ability of future generations to meet their own needs. It has become a key guiding principle for policy in the 21st century. Worldwide, politicians, industrialists, environmentalists, economists and theologians affirm that the principle must be applied at international, national and local level. Actually applying it in practice and in detail is of course much harder (Twidell. JW, Weir. T, 2006).

It is common knowledge that the non renewable sources of energy such as oil, coal, gas and uranium are being depleted. As a result, renewable source of energy such as hydro, wind, biomass, geothermal, oceanic and solar have become increasingly more important.

There are two forms of sunlight conversion which result in usable energy. These two forms are thermal and photon activated (commonly called photovoltaic); the first has been in use much longer than the second. In nearly a century and a half, since the photovoltaic effect was first observed in 1839, the technology has grown from an experimental curiosity into a fully developed science.

More than one out of six people lack access to safe drinking water, namely 1.1 billion people, and more than two out of six lack adequate sanitation, namely 2.6 billion people (Estimation for 2006, by the [WHO/UNICEF Joint Monitoring Programme, 2004](#)). While the world's population tripled in the 20th century, the use of renewable water resources has grown six-fold. Within the next fifty years, the world population will increase by another 40 to 50 %. This population growth - coupled with industrialization and urbanization - will result in an increasing demand for water and will have serious consequences on the environment (www.worldwatercouncil.org/). Food production is by far the most important activity and in many regions irrigation is essential, or could increase crop yield, and barren land could be fertile if supplied with water. Water pumping, is therefore a basic need for a large proportion of the world's rural population. Since the majority of this rural population live in the sunny tropics or Saharan (steppe) area, to use the sun's energy is an attractive way for providing these vital energy needs. Traditionally, water is provided by hand, with the assistance of animals or combustion engine motor-pump set. Solar energy may also be used as supplement to classical power grid.

1.2 Literature review

Long history of water pumping led to the development of many methods for pumping water with minimum efforts and energy. The techniques

range from a simple hand pump to high efficiency electric pumps. In remote rural areas where access to electric supply is not practical, the use of diesel pumps is very common. However, the system suffers with number of problems, such as fuel supply, technical knowhow and of course the operating cost. Photovoltaic (PV) operated water pumping system provides an alternative. Various systems have been developed and tested around the world (Moechtaar. M et al, 1991), (Hamid. M et al, 1996), (Grassie. T et al, 2002) and (Ghoneim. AA et al, 2006). Their performance has been assessed under varying climatic conditions and insolation. These systems are operated with ac or dc, directly coupled or battery operated, using various pumps, running under different climatic conditions. The PV systems are becoming increasingly popular, especially in remote areas where power from a grid is not available or is too costly to be installed. Also the progress made in the world market of photovoltaic emphasizes the maturity of investments realized, guarantees the reliability of the technology utilized and makes it competitive for a variety of applications to meet the energy demands (Kaldellis. JK et al, 2009). It is estimated that a single PV station of area 250 km^2 or 12 decentralized stations each 72 km^2 would be enough to meet the year 2020 world electricity requirement (Muneer. T et al, 2003). The water pumping systems are frequently used for irrigation, livestock watering and in households' water supplies and in many cases are cost effective. A study carried in Namibia shows that a PV powered system can operate at about half the life cycle cost to that of a diesel pumping (Ministry of mines and energy, 2008). However, two major issues – high initial investment and low efficiency, limit the wide spread use of PV system. The achievable efficiency in the conversion of solar radiation to electricity by solar cells is still low, 9–12% under real conditions (Muller. JC, 2007) and (Oleksiy. N, 2005). The initial cost of a PV system is about three times more than that of a diesel pumps with the same performance (Short. TD, Oldach. R, 2003).

Most African, South Asian and Latin American countries are exposed to sun almost throughout the year, where the solar intensity is quite high (Ramos. JS, Ramos. HM, 2009). Among these countries Algeria is the one blessed with a geographical location that holds one of the highest reservoirs where topography and local climate favors its use. The insolation time over the quasi-totality of the national territory exceeds 2000 h annually and may reach 3900 h (high plains and Sahara). The daily irradiation on a horizontal surface is 5 kWh/m² over the major part of the territory (1700 kW h/m²/year in the north and 2263 kW h/m²/year in the south of the country), as shown in Table 1.2.1, (Ministry of energy and mines, 2008). The interest towards the development of renewable energy in Algeria was perceived as early 1962 with the establishment of "Solar Energy Institute". Algeria intends to produce 6% to 7% of its power from renewable energy including solar and wind as main sources, by the year 2020 that represents at least 450MW (APRUE, 2008). To achieve the target a number of initiatives have been taken that include a comprehensive solar rural electrification program of 20 villages and 150MW hybrid solar-gas project at Hassi R'mel (Ministry of energy and mines, 2008). Since commissioning, over 1000 households have been electrified through this program. The performance of PV pumping systems is influenced by local weather conditions. It varies with variation in cloud covers, temperature, wind speed etc... Potential sites for solar application are however mainly characterized by stable insolation. Fortunately these sites coincide with those parts of the earth where the need for water pumping is the greatest (Anis. WR, Nour. MA, 1994) and the same applies to Algeria. PV water pumping systems have been introduced in Algeria quite some time ago. The use of PV pumping at small-scale irrigation in isolated regions of Algeria has increased considerably in the last few years, which lead to a growth of technical knowledge (know-how) within the local population composed mainly of small farmers. They also have the experience of using diesel or gasoline pumps. They tend to deal with such systems in the same way as they use to do with a diesel or gazoline

unit i.e. being able to intervene whenever necessary to repair a pump, without seeking external technical assistance. This slightly compensates to relatively high initial investment. The system under study was restricted to the basic PV pumping system configuration, which is, a PV panel directly connected to a dc motor-pump and a piping system. The developed system does not need battery for intermediate energy storage and also no electronic control systems is added that would lead to high initial cost and maintenance complexity (Short. TD, Oldach. R, 2003) and (Firatoglu. ZA, Yesilata. B, 2004).

Table 1.1
Solar energy potentials in Algeria.

Areas	Coastal area	High plateaus	Sahara
Surface (%)	4	10	86
Average sunshine (H/year)	2650	3000	3500
Average energy received (kWh/m ² /year)	1700	1900	2650

In terms of renewable energies, Algeria hopes to increase production to 6% of national electricity consumption by the year 2015. In 2006, this was only 0.02% (5 GWh). Algeria was ranked (in 2006-2007) the third country in the world in terms of capacity of renewable energy. Its potential is estimated at more than 6,000 megawatts. It is preceded by Germany, whose resources are around 18,000 MW and Spain, which has 15 000 Mw. The energy potential of Algeria is the equivalent of 4 times the World Annual power consumption. It is therefore necessary to better valorize this potential, according to experts (www.neal-dz.net).

1.3 Objectives and perspectives

The primary objective of this work is to build a test bed simulating a real PV pumping system. The system had to be simplified to its simplest form, namely, a centrifugal pump driven by a DC motor connected directly to a PV panel. Water is pumped through a closed loop circuit from a lower tank to an upper tank. Neither batteries nor complex electronic components such as maximum power point tracker are added.

Each element of the system is modeled separately from the PV panel to the hydraulic system. The complete mathematical model of the total system consists then of mathematical equations describing each element for itself. It has to be said that all elements of the system had to be locally available and not specially designed for photovoltaic solar pumping application except for solar panels.

In chapter 4 the photovoltaic cell (module) model is described, the cell model is essentially made up from I-V characteristics which describe the current and voltage output of the cell (module) under different irradiance values and temperature. The model is derived from the basic theory of semiconductors and the photovoltaic effect; the PV array characteristics for different irradiance level were drawn by using a simple model developed on the basis of the analogy that exists between the I-V characteristics of a solar cell and the rise of current in an inductive circuit. The equations which describe the motor operation and the factors influencing its operating point are presented in chapter 5. Only permanent magnet brushed DC motor is considered.

The mathematical expression for the torque required for pumping a given quantity of water is developed in chapter 6 which considers centrifugal pumps only. The torque expression is derived from the Newton equation of moment of momentum involving the pump impeller characteristics (dimensions). The pumping system model and all elements interaction is described in chapter 7. Chapter 3 deals with solar irradiance data recorded and its arrangement. A comparison is made between mean hourly

irradiance data, Typical Meteorological Year data and a novel artificial neural network classification method of solar irradiance data. The method consists of a self organizing map based on Kohonon's unsupervised learning algorithm (Kohonen. T, 1995).

The complete photovoltaic water pumping system was finally tested at the university of UST Oran. The test itself was used as a mean of evaluating different elements model and to show that, to a certain extent, off the shelf components, such as DC motor and centrifugal pump can be used for photovoltaic pumping application.

CHAPTER 2.0

PHOTOVOLTAIC PUMPING SYSTEMS

2.1 Introduction

Photovoltaic water pumping systems (PVWP for short) are conceptually divided into three parts:

- The PV array which converts solar radiation energy to d.c. electrical energy.
- The motor and pump subsystem in which the array electrical output is converted into mechanical and then hydraulic energy.
- The hydraulic system which delivers water to its point of use.

Various degrees of sophistication may be incorporated into the system such as, a maximum power point tracker (MPPT) to maintain the highest power output from the PV array in varying conditions of insolation. An inverter has to be used in the case where an A.C. motor is used to power the pump. One major difficulty facing the use of PV pumps is that the energy required for pumping a certain quantity of water is not available on demand and does not necessarily coincide with the peak water demand. Solar irradiance varies continuously, which means that for some locations with successive cloudy periods it may be prudent to consider storage of surplus of water pumped on clear periods, for use on cloudy days. Another way of tackling the problem of non availability of solar energy when mostly needed, is to incorporate a battery bank in the system to store electrical energy to be used when necessary enabling the system to start pumping any moment including at night. However, electrical energy storage has proved to be very demanding in maintenance time and costs. Also batteries can increase considerably the overall initial system cost.

PVWP systems are similar to any other pumping system, only the power source is solar energy. Photovoltaic arrays in PVWP are fixed mounted or sometimes placed on trackers to increase pumping time and volume. AC and DC motors with centrifugal or displacement pumps are used with PV pumping systems. The most inexpensive PV pumps cost less than \$1,500, while the large systems can run to over \$20,000. Most PV water pumps rarely exceed 2 horsepower in size. Well installed quality PV water pumping systems can provide over 20 years of reliable and continuous service ([El Paso Solar Energy Association](#), 2007). PV modules on the market today are guaranteed by manufacturers from 10 to 20 years, while many of these should provide over 30 years of useful life. A well-designed PV system will operate unattended and requires minimum periodic maintenance. PV conversion efficiencies and manufacturing processes will continue to improve, causing prices to gradually decrease, however no dramatic overnight price breakthroughs are expected ([El Paso Solar Energy Association](#), 2007). For the past and future trends in component costs of PV systems see Figure 2.1.

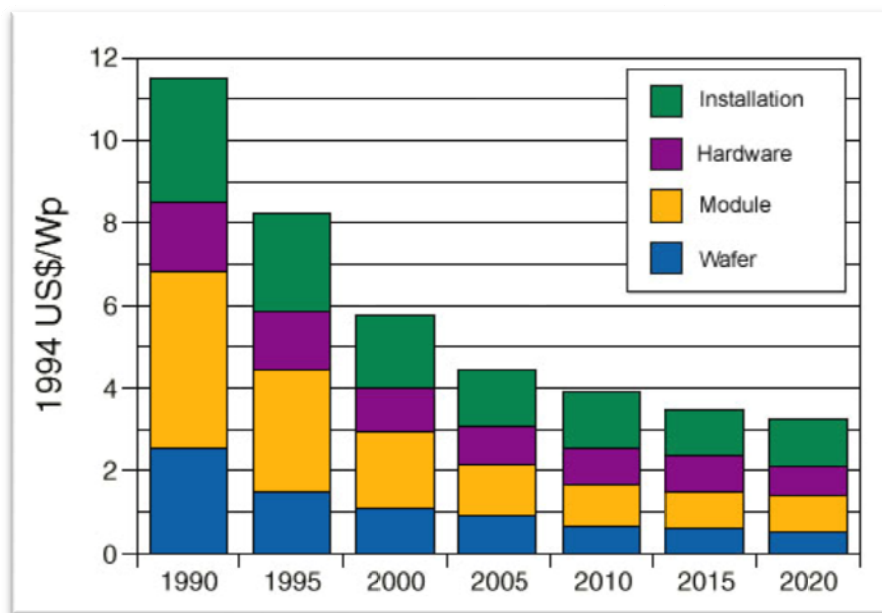


Figure 2.1 Graph showing component costs of PV system and price reduction over time. (IEA PVPS, annual report 2008).

Although PVWP systems cannot yet compete with efficient conventional central generating plants such as diesel units, gas turbine generators units, the vast majority of PVWP installations to date have been for relatively low-power applications (less than 2 kW) in locations, which do not have complete access to a mains electricity grid. In such cases, PV has been selected because it offers a secure and reliable power supply, and is often the cheapest power option.

2.2 Photovoltaic Technologies

A PV cell is the building brick of a PV module, and a module is in turn a building brick of a PV array (panel concept may be referred to as a module or a number of modules brought together in a particular way). A PV solar cell directly converts solar radiation to electricity, using no moving parts or heat power. Photovoltaic cells are composed of layered semiconductors in contact with metal electrodes and covered by a protective transparent glazing. When the semiconductor material absorbs photons with an energy level greater than its band gap energy, electrons are freed and carried away by metal electrodes. Power is produced by connecting the electrodes to an external load. The semiconductor material used in cells is predominantly silicon because the band gap energy of silicon results in a theoretical efficiency very near to the maximum for solar radiation (Luque, 2003). Silicon (Si) is in group IV of the periodic table. Free Si atoms need four extra electrons to make up the number of eight (closed shell configuration), the additional electrons may be obtained by the formation of a crystal in which every atom of the lattice is surrounded by eight electrons, all of which are shared with neighboring atoms. The whole crystal remains electrically neutral because the total number of charges of its constituent atoms has not changed. If an electron obtains enough energy to leave its shell, it becomes mobile inside the crystal. The minimum energy required to free an electron is equal to the band gap

$E_g = 1.14 \text{ eV}$ corresponding to a light wavelength of $\lambda = 0.97 \mu\text{m}$ at a temperature of 27°C . In semiconductors, when the temperature is close to absolute zero, the valence band is completely occupied, whereas the conduction band is completely empty. Only electrons in the conduction band are mobile due to the necessary moving space that exists in that band. Symmetrically, holes are mobile only the valence band (Figure 2.2). The maximum efficiency of a PV cell can be increased further if multiple semiconductor layers, or junctions, are stacked. In this case, the band gap of each layer is optimized for a different range of photon energies, thereby taking advantage of a greater range of the solar spectrum and improving the overall cell efficiency. Figure 2.3 shows a typical spectral selective response of silicon solar cell, which does not correspond to the maximum power region of the solar spectrum.

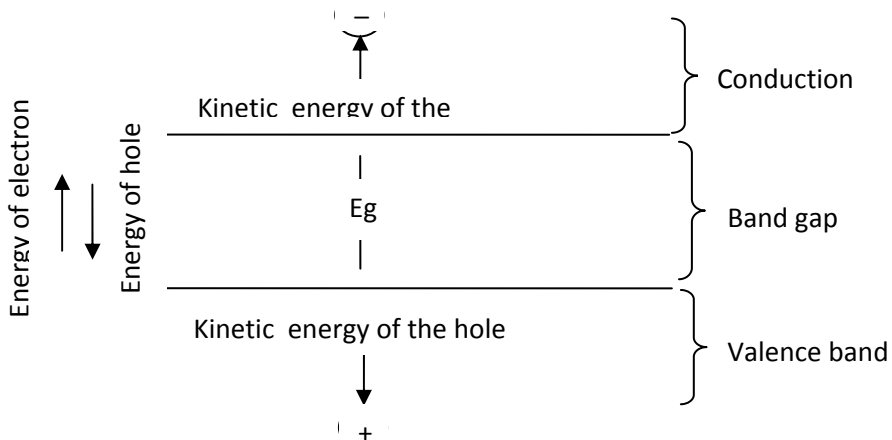


Figure 2.2 Energy band concepts diagram.(Twidell.JW, AD. Weir, 1986).

Detailed and well illustrated concept and technology can be found in the second edition of "renewable energy resources" by (Twidell.JW, and AD. Weir, 2006).

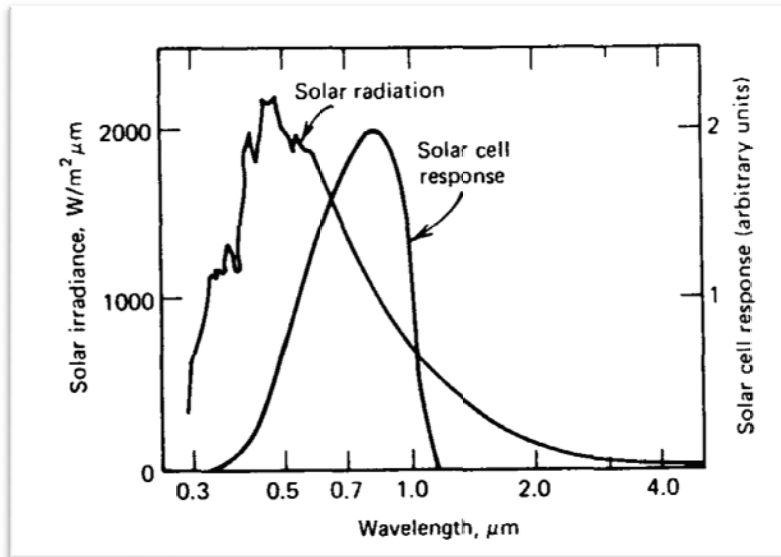


Figure 2.3 Spectral distribution of extraterrestrial solar radiation and spectral response of a silicon solar cell (Duffie JA, WA. Beckman, 1980).

2.2.1 Photovoltaic cell production

Terrestrial use of photovoltaic cells for power production is quite recent, even though the photovoltaic effect has been known since 1839. The main type of cells used commercially for solar water pumping (and indeed for most terrestrial photovoltaic applications at present) is the monocrystalline silicon cell. However other types such as polycrystalline and amorphous silicon cells are being increasingly used. The main producers of PV cells and panels include Sharp, Kyocera, BP Solar, Siemens Solar, Astropower, Sanyo, Photowatt, ASE, Mitsubishi and Isofoton. Details of the products available from these companies can be obtained from the company websites. Monocrystalline silicon is grown as a single crystal into cylindrical ingots and cut into thin wafers. These monocrystalline silicon wafers are often cut into squares or squares with rounded corners to maximize the power area density, the cells made from these wafers are therefore quite distinguishable, as shown in Figure 2.4.

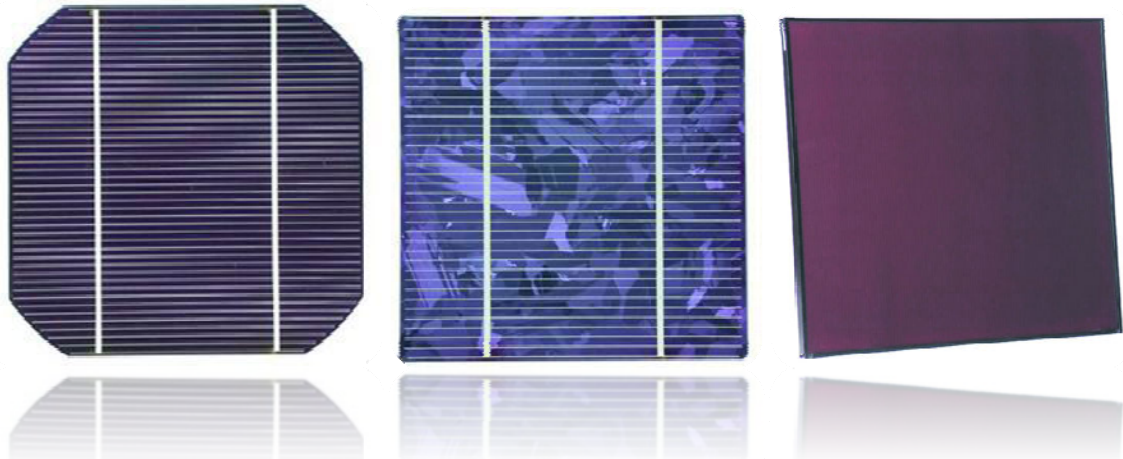


Figure 2.4 A monocrystalline silicon cell (left) (Xinchang, 2009), a polycrystalline silicon cell (middle) (Xinchang, 2009), and a thin-film amorphous silicon module (right) (not to scale) (Kaneka, 2009).

Polycrystalline silicon is produced by melting and crystallization, block-casting, or drawing into ribbons, where multiple crystals grow from numerous nucleation sites (Luque, 2003). These processes are typically more economical than that used for monocrystalline silicon, but the resulting cells have lower efficiencies, as shown in Figure 2.5 (Nozik, 2005). Amorphous silicon and other thin-film technologies are produced by substrate deposition processes and result in noncrystalline materials (Luque, 2003). These deposition processes are also used to produce multiple junction cells. Thin-film cells have some of the lowest production costs, and efficiencies vary, as shown in Figure 2.5.

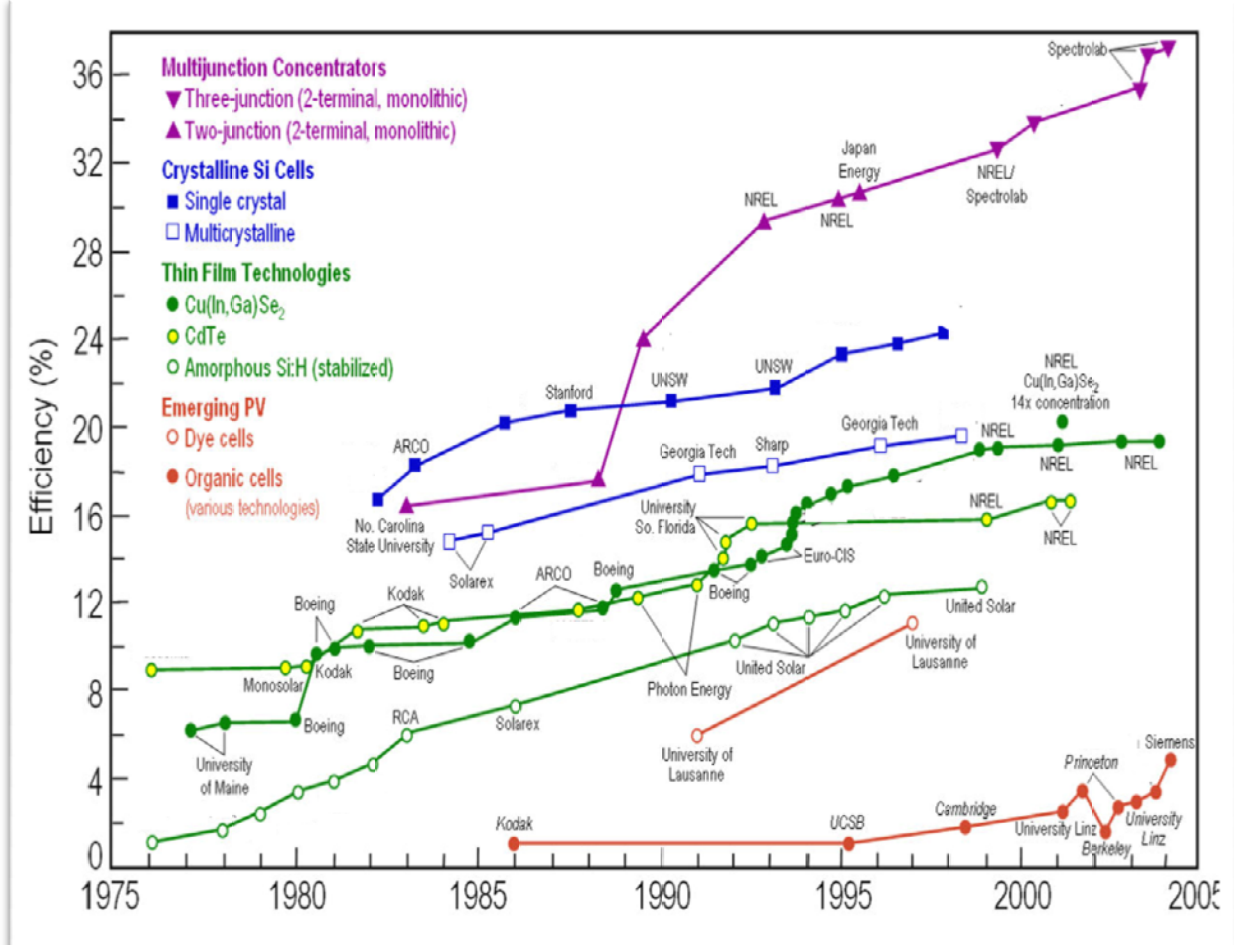


Figure 2.5 Research cell efficiencies of various technologies and their progression over the previous thirty years (Nozik, 2005).

2.2.2 Photovoltaic cell performance

Photovoltaic solar arrays are often assembled from a combination of individual modules. Each module is itself a combination of cells. Modules are electrically connected in series and parallel to give suitable voltages and currents for a particular application. A typical module is sized about 1m by 0.3m by 50mm thick and contains usually 36 cells, thereby producing an output of 30-50 watts at 12 volts in bright sunshine.

The performance of PV solar cells is dependent on the voltage of the load, the amount of radiation absorbed by cell, and the cell temperature. Photovoltaic cells operate like a direct current source that rapidly decreases above a certain operating voltage, with the voltage dictated by

the load. The *maximum power* (P_{max}) output of a cell, at a given radiation level and temperature, occurs near the bend in the current-voltage (I-V) curve, as shown in Figure 2.6. The current at zero voltage is termed the *short-circuit current* (I_{sc}) and the voltage point at zero current is termed the *open-circuit voltage* (V_{oc}). The current and voltage of a PV cell are both dependent on radiation and temperature, however, the current is primarily dependent on the radiation in a near-linear relationship at short-circuit conditions and the voltage is primarily dependent on the temperature in a near-linear relationship at open-circuit conditions.

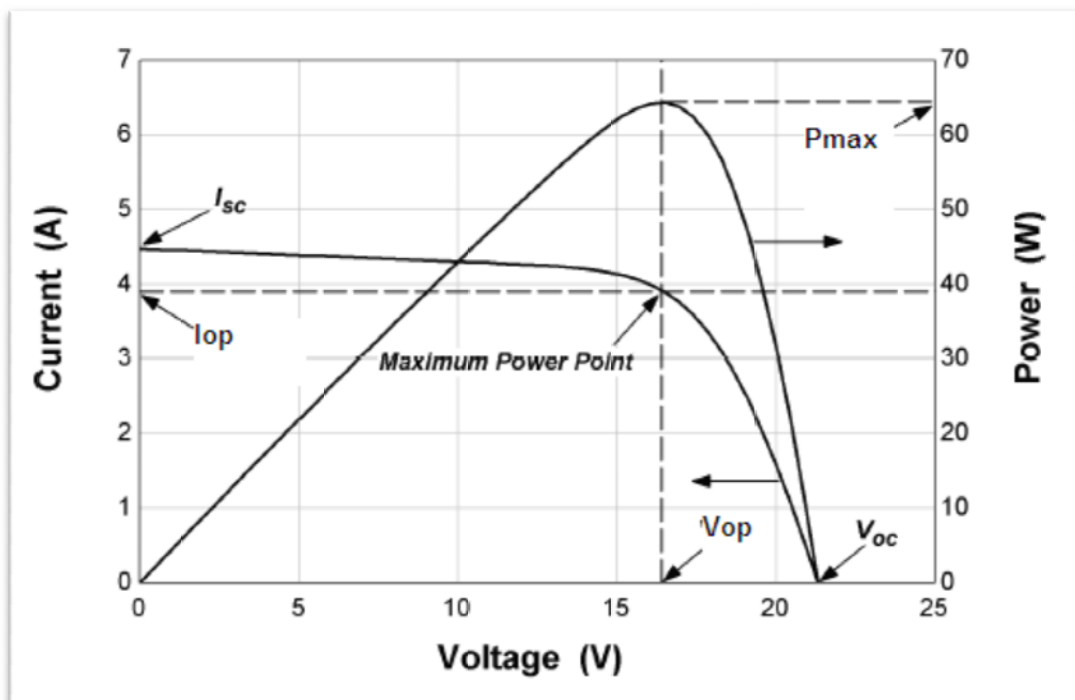


Figure 2.6 I-V characteristic of a photovoltaic module at a given irradiance and cell temperature
(Duffie. JA, WA. Beckman, 2006).

Cells are encapsulated with special materials so that they can withstand environmental effects. Module (array) support has also to withstand climate stress, e.g. wind, sand, snow and birds dejections, hence the use of galvanised steel, aluminium or chemically treated wood as common materials for the module (array) support. Arrays are usually fixed in position and mounted on concrete foundations. Some arrays can follow

the apparent motion of the sun and so intercept more energy, but this can also increase cost and complexity.

The most common measure of output of photovoltaic module (array) is the “peak power”. This is the maximum power that can be delivered under standard conditions of 1000W/m^2 solar irradiance at 25°C .

The “peak power” is usually referred to as the peak watts (W_p). To give an idea of power and surface area of cells, if the cell efficiency is 10%, a 1kW_p array would contain a cell area of 10 m^2 . The packing factor is the ratio of cell area to module area, for circular cells this factor is about 75% giving a gross area of 13.3 m^2 for a kW_p array. Modules with square cells have a much more higher packing factor, about 90%.

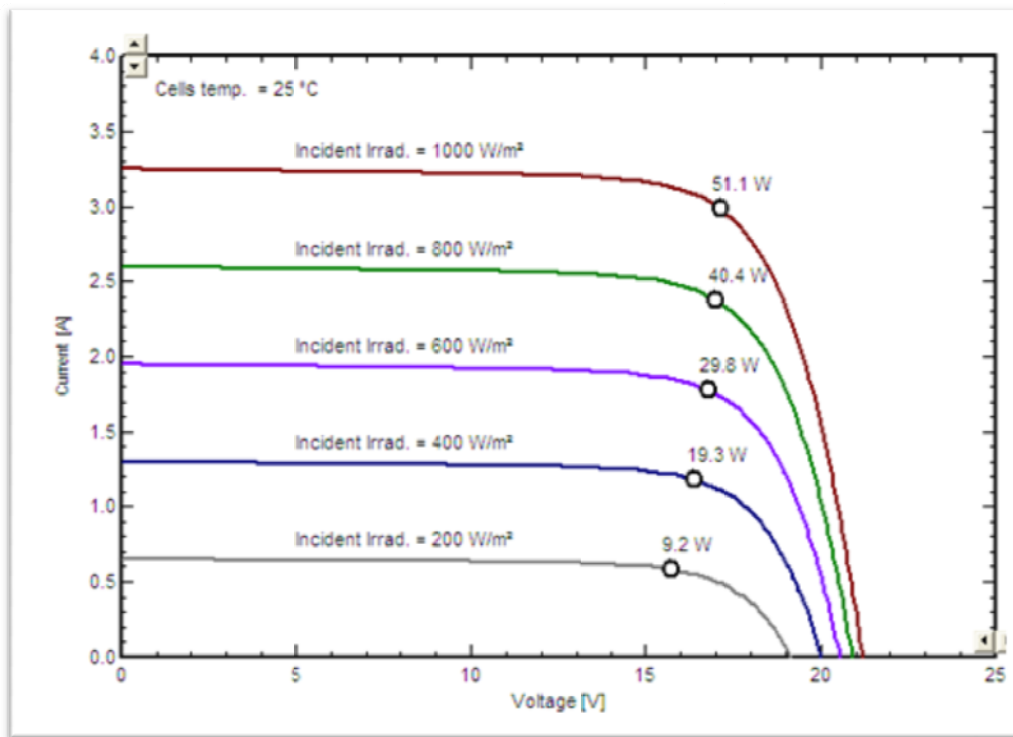


Figure 2.7 I-V characteristics a Kyocera LA 361 K 51 Module at different solar irradiance values and given temperature (PVSYST V5_0, 2011).

From the figure above it can also be seen the maximum power point position (at the knee of the I-V characteristic) for different solar irradiance values. By joining these points we can have what is called the maximum power line, as illustrated in figure 2.8.

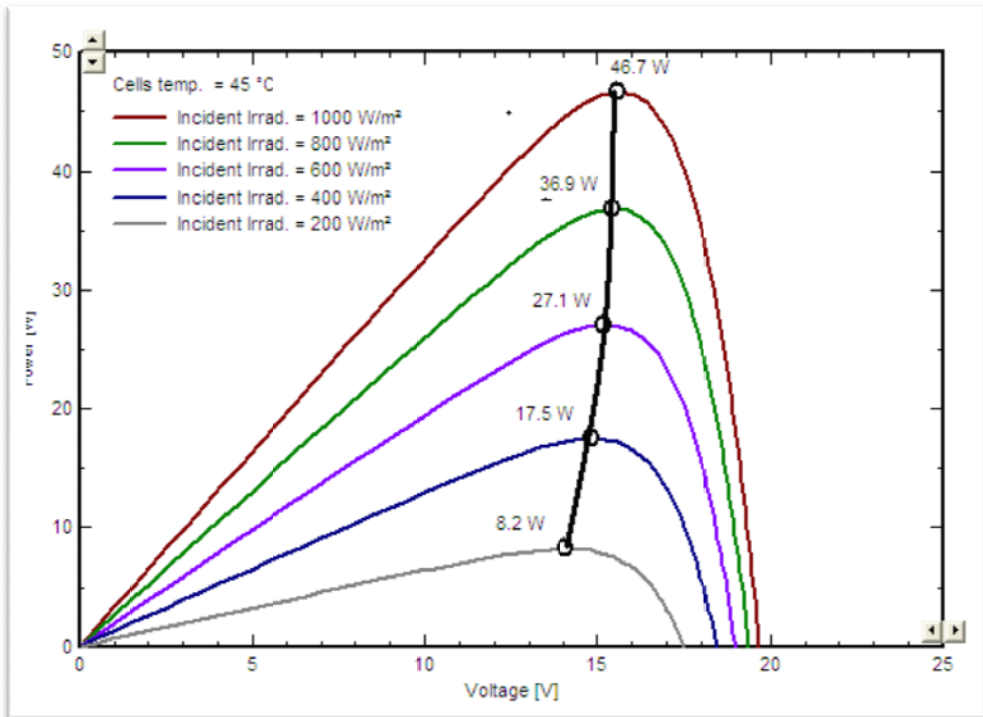


Figure 2.8 Power against voltage of a Kyocera LA 361 K 51 Module at different solar irradiance values and given temperature, with maximum power line(PVSYST V5_0, 2011).

2.3 Motor-Pump Subsystem

It is known that unlike conventional power driven pumping systems, photovoltaic pumping systems do not operate at a constant power. In fact This power varies constantly with the incident solar energy and ambient temperature. This means that the motor-pump subsystem is due to work over a range of voltage and current levels. Because of these variations and the resulting changes in subsystem efficiency, it is useful to define two types of efficiency:

- a- Subsystem power efficiency: This is the ratio of hydraulic output power to electrical input power, at any time. This will have a peak value when the subsystem operates at its design conditions.
- b- Subsystem energy efficiency: This is the ration of hydraulic output energy to electrical input energy over a day. It is a time average of the power efficiency, and consequently depends on the daily

variations in power efficiency and hence on the solar irradiance and temperature profile for the day.

In figure 2.7 it was shown that the power delivered by the photovoltaic array has a maximum power point for each solar irradiance level. To maximise the output from the array to a specific load, the operating point needs to be as close as possible to the knee of the array I-V characteristic (figure 2.9). Any load mismatch therefore represents a loss of efficiency. In directly coupled photovoltaic systems , provided that the level of irradiance gives a short circuit current sufficient to overcome the starting torque, the mechanical load (motor-pump) will start and the rotational speed will increase until the power absorbed by the load plus the losses, is equal to the power output of the array. Any increase of irradiance will result in an increased speed to maintain this balance of power. A well optimised system is not only a system which operates efficiently but also a system which can operate at low solar irradiance level, hence a system with low starting torque characteristic.

This will enable it to start operating early morning.

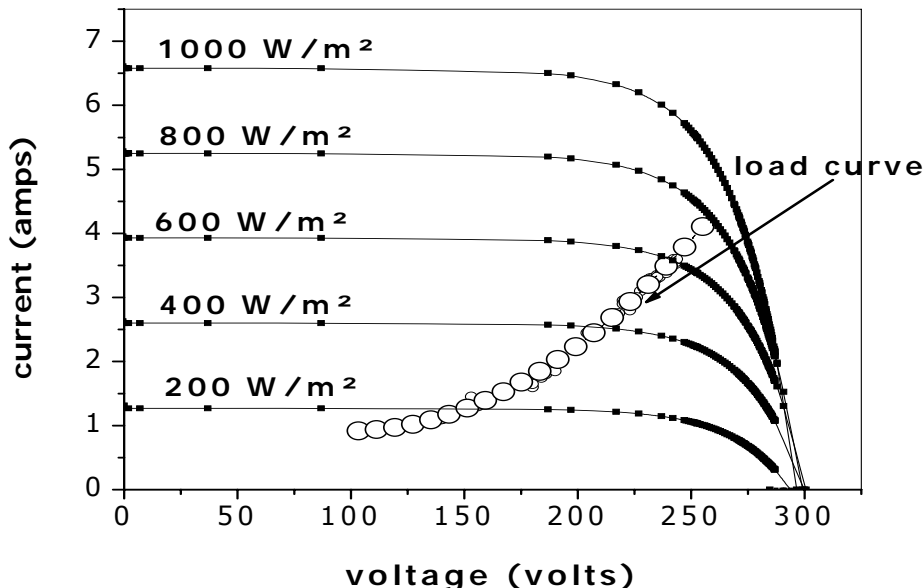


Figure 2.9 Photovoltaic array I-V characteristics for different irradiance levels with the locus of operating points (load curve) (work of this thesis).

2.3.1 D.C. motor technology

The three main motors that have been extensively used in photovoltaic water pumping are:

- i- Brushed type permanent magnet D.C. motors
- ii- Brushless permanent magnet D.C. motors
- iii- A.C. motors

D.C. motors are of course the most attractive solution because the array provides a D.C power supply. Only D.C. motors are considered in this work, A.C. motors are cited for comparison purpose only.

In table 2.1 are listed some types of motors with their respective efficiency. From this table it can be seen that permanent magnet motors are more suitable for photovoltaic pumping than the other types of motors. However, and for high power applications A.C. motors in conjunction with D.C-A.C inverters present some advantages: (a) they present to the designer of PVWP a wide range of choice, due to the extensive use of A.C. motors in electrical systems and (b) their prices are less than D.C. motors.

Table 2.1 Motor efficiencies (less than 1 kW of power) (Smith.D.V, Allison.S.V, 1978)

MOTOR TYPE	EFFICIENCY
AC INDUCTION - SPLIT PHASE	27% - 46%
- 3 PHASE	35% - 50%
- PERMANENT SPLIT CAPACITOR	28% - 64%
AC/DC UNIVERSAL	46% - 51%
DC PERMANENT MAGNET	69% - 86%

It has to be noted that for small photovoltaic systems with power less than ½ kW the savings made by using a low cost A.C. motor maybe offset

by the inevitable cost of an inverter (based on the UNDP/world bank phase I report)(Halcrow.w, 1981). In the first stages of our case study and despite all efforts not a single local electrical machine supplier was found. Brushed D.C. motors generally requires new brushes at intervals of the order of 2000-4000 hours, otherwise, certain models can suffer irreparable damage. Fail-safe brush design, may prevent the machine to be definitively destroyed by stopping it once brushes are too warm. Brushes are a source of energy loss due to resistive losses and due to friction with the commutators surface. The buildup of carbon dust that arises from brushes is another problem linked with brushed D.C.motors. An alternative solution is brushless permanent magnet type motors, with the magnets in the rotor and an electronically commuted stator (figure 2. 10). In principle, such machines are more attractive than brushed machines, since their only wearing parts are the bearings and any seals. Although early problems with the electronics have been corrected, the electronic circuitry is still vulnerable to overheating due to the high temperature that can be reached when the motor runs for long periods, especially in high plateaus and sahara. The laboratory testing program completed during the first phase of the UNDP/world bank project indicated that the best D.C. permanent magnet motors, in the 250 to 500 W range are capable of optimum efficiencies of around 85% and even at half load their efficiencies should exceed 75%.

D.C. motors utilize permanent magnets so none of their energy needs to be used in the creation of an electromagnet as in A.C. motors. The energy used by A.C. motors to create the electromagnet decreases the efficiency of the A.C. motor in comparison to the D.C. motors. At the same time, brushless D.C. motors are considered more energy efficient than brushed D.C. motors. This means for the same input power, a brushless D.C. motor will convert more electrical power into mechanical power than a brushed motor, mostly due to absence of friction of brushes. A brushless D.C. motor, for the same mechanical work output, will usually be smaller

than a brushed D.C. motor, and always smaller than an A.C. induction motor. The brushless D.C. motor is smaller because its body has less heat to dissipate. From that standpoint, brushless D.C. motors use fewer raw materials to build, and are better for the environment (Orientalmotor constructor web site).

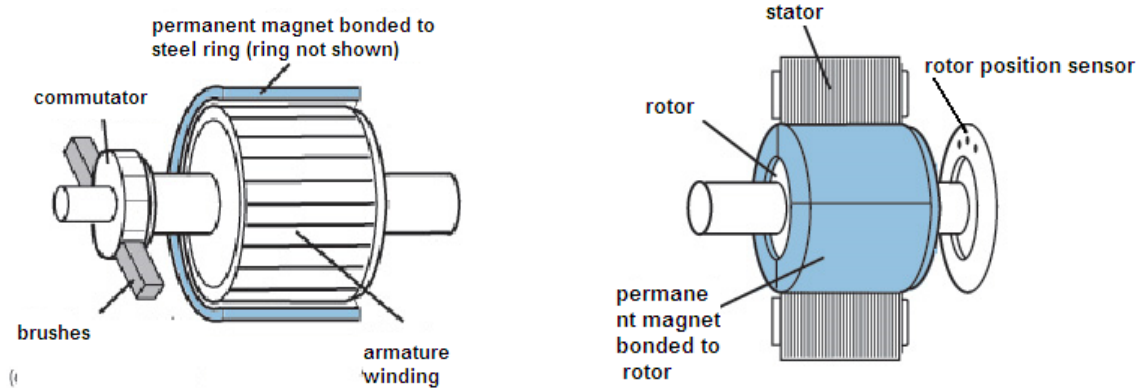


Figure 2.10 D.C. motors structure (a) brushed D.C. motor
 (b) brushless D.C. motor (www.Orientalmotor.com).

2.3.2 Pump technology

Pumps used in photovoltaic pumping are basically divided into two different categories: centrifugal and positive displacement pumps.

Centrifugal pumps:

They are mainly used for low suction lift (less than 5m). The water output increases with rotational speed. Centrifugal pumps are studied at their so-called design conditions; i.e. at the head and capacity (flow rate) condition at rated speed at which maximum efficiency is obtained. The flow delivered by a centrifugal pump varies directly with the impeller rotational speed, while the developed head varies as the square of the impeller rotational speed, thus the power required to drive a centrifugal pump varies as the third power of the rotational speed, which gives centrifugal pumps the capability of achieving a close natural match with a photovoltaic array over a broad range of operating conditions. To

overcome their principal problem which is priming, centrifugal pumps can reliably be operated in submerged floating motor-pump sets.

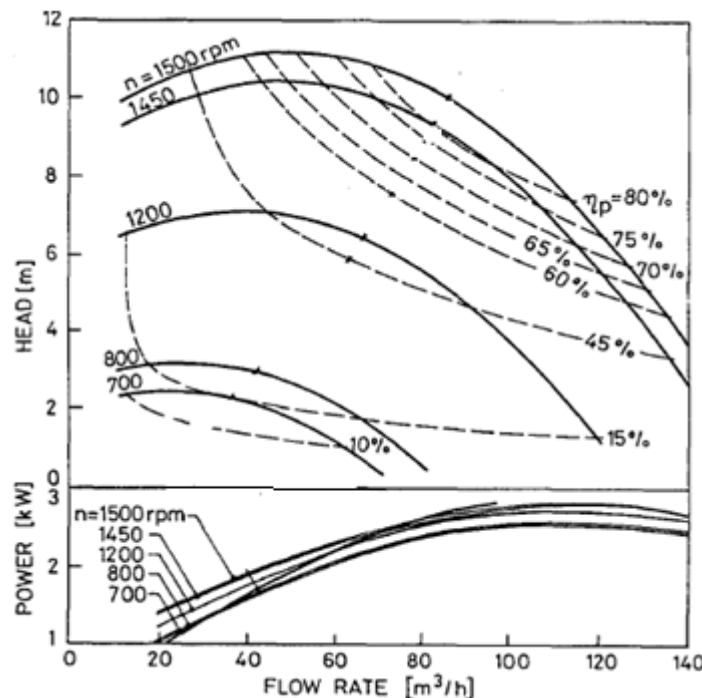


Figure 2.11 Typical centrifugal pump characteristics (Halcrow.W, 1981)

Positive displacement pumps:

They are totally different from centrifugal pumps. One much known type is the reciprocating pump, which consist essentially of a piston moving in a cylinder. Reciprocating pumps present an almost vertical characteristic. This means that the capacity (flow rate) output is practically independent of the head, but directly proportional to the speed. The efficiency of such a pump (of fixed piston diameter) increases with the head. Therefore for optimum efficiency, different diameter pumps need to be used for different heads. At high heads, the frictional forces become small relative to the hydrostatic forces, and consequently at high heads positive displacement pumps can be more efficient than centrifugal pumps. At low heads, the total hydrostatic forces are low in relation to the frictional forces and hence positive displacement pumps are less efficient and less likely to be used. It was concluded, in (Halcrow.W, 1981), that (a) reciprocating pumps cannot be operated effectively directly coupled to a

photovoltaic array, (b) that careful system design must be employed to achieve efficient use of the photovoltaic array. The standard solution to these problems has been to add a battery between the array and the pump set.

2.3.3 Pumping system configurations

Photovoltaic pumping is used principally for three applications: village water supply, livestock watering or irrigation. Photovoltaic pumping systems are broadly configured in five types described below:

- (a) Submerged multistage centrifugal motor pumpset (Figure 2.12).
- (b) Submerged pump with surface mounted motor (Figure 2.13).
- (c) Reciprocating positive displacement pump (Figure 2.14).
- (d) Floating motor pump sets (Figure 2.15).
- (e) Surface suction pump sets (Figure 2.16).

Each system configuration is suited to a particular range of head and flow.

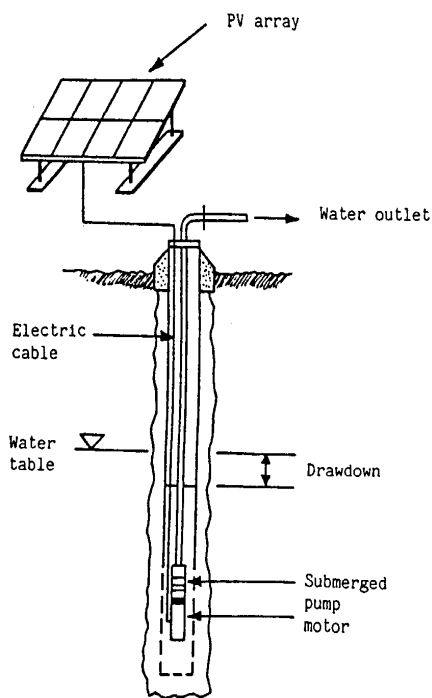


Figure 2.12

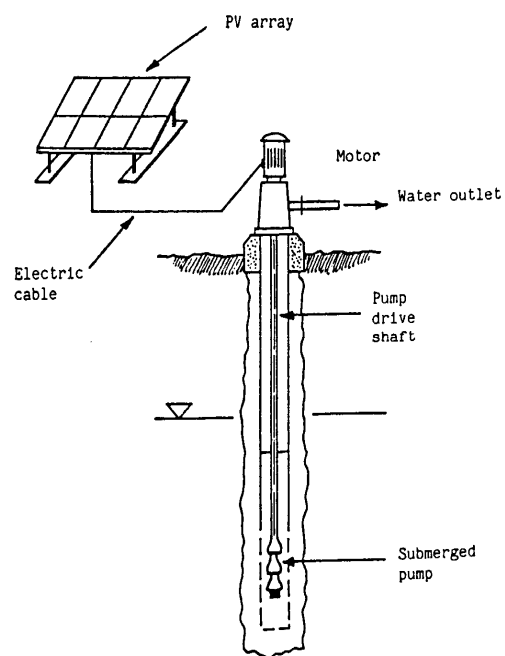


Figure 2.13

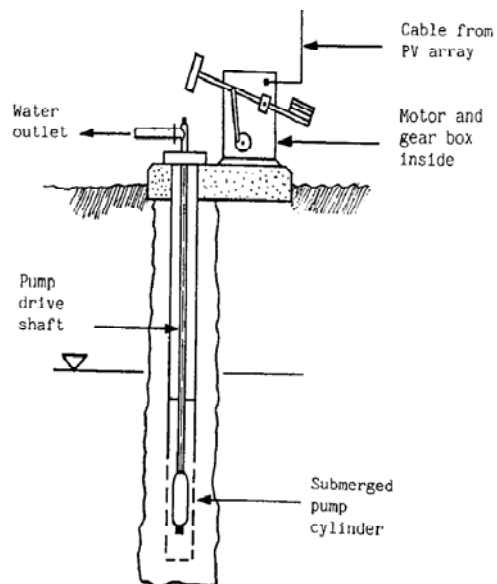


Figure 2.14

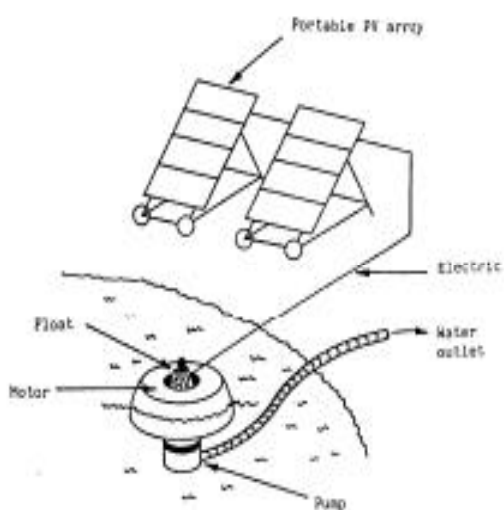


Figure 2.15

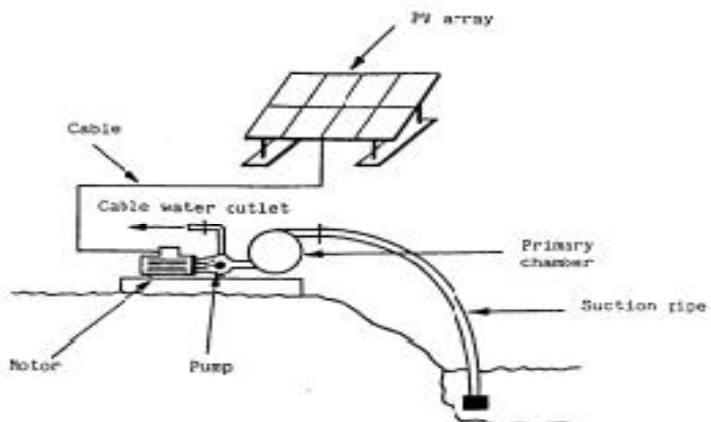


Figure 2.16

CHAPTER 3.0

SOLAR RADIATION DATA MEASUREMENTS

3.1 Introduction

One of the most important requirements in the design of any solar energy conversion system is the information on the intensity of solar radiation at a given location. Such data are required in many applications ranging from design of photovoltaic systems, solar collector systems, solar crop drying systems and building sciences. Solar radiation data is available either by direct measurement or estimation of its different components in different forms. In order to understand or use these data, we must bear in mind whether they are instantaneous measurements (irradiance) or values integrated over some period of time (irradiation) (usually hour or day), the time or time period of measurements used, the receiving surface orientation (usually horizontal, sometimes inclined at a fixed slope, or normal to the beam radiation), and, if averaged, the period over which they are averaged (e.g. monthly averages of daily radiation) (Duffie. JA, Beckman. WA, 1980).

Even though modeling is an economical and essential tool for the estimation of solar radiation, the accuracy of such models depends on long-term measurements of the data used. Though less accurate, modeling is a better tool for the estimation of solar radiation at places where measurements are not available but have similar climatic conditions to the measured location.

3.2 Components of solar radiation

Solar radiation incident on the atmosphere from the direction of the Sun is the solar extraterrestrial beam radiation. Beneath the atmosphere, at the Earth's surface, the radiation will be observable from the direction of the

Sun's disc in the *direct beam*, and also from other directions as *diffuse radiation* figure 3.1 is a schematic illustration of this (Twidell. JW, Weir. AD, 2006). It must be noted that even on a clear sky, clouds free sky, there is always at least 10% diffuse irradiance from the different particles suspended in the atmosphere. The practical distinction between the two components (beam and diffuse) is that, only the beam radiation can be focused (concentrated). The ratio between the beam (direct) irradiance and the total irradiance thus varies from about 0.9 on a clear day to zero on a completely overcast day (Twidell. JW, Weir. AD, 2006). Identifying various components of the solar radiation is a very important task as well as the plane (tilt angle) on which the irradiance is being measured.

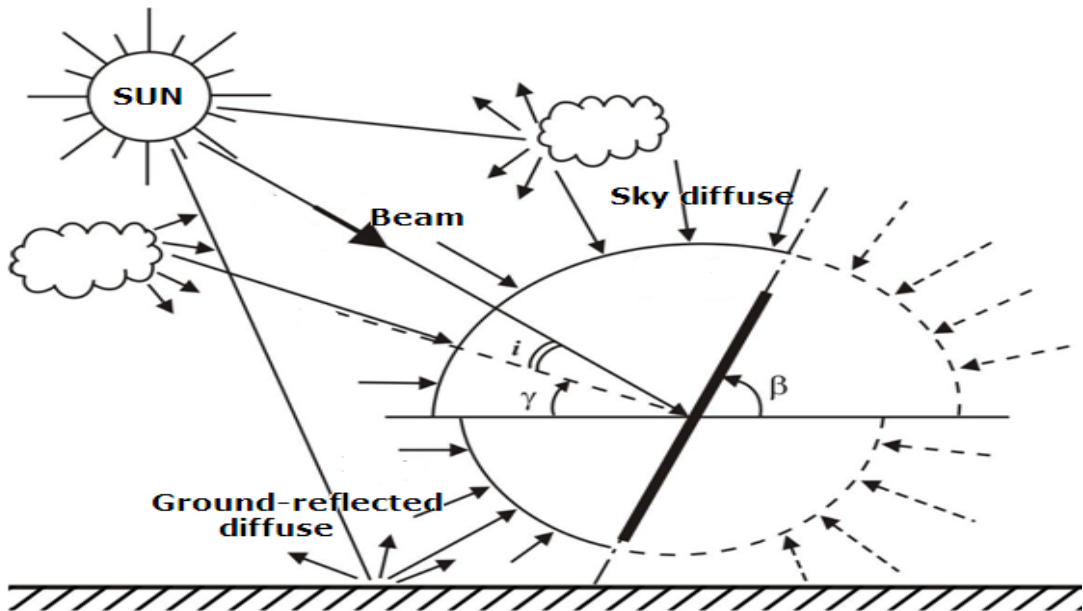
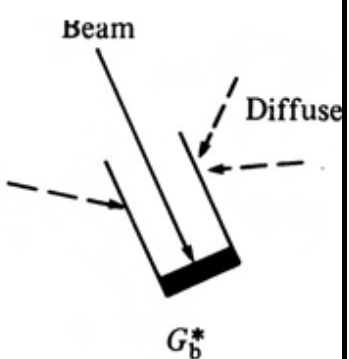
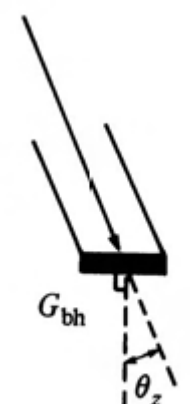
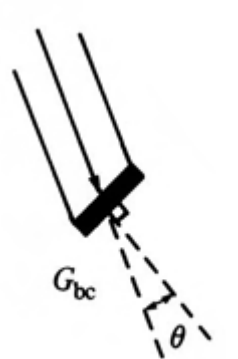
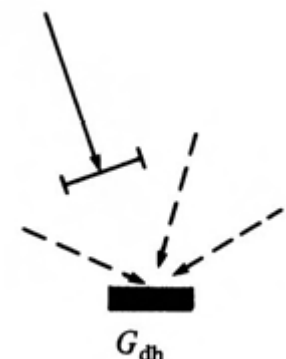
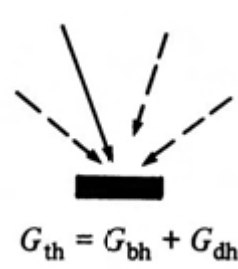
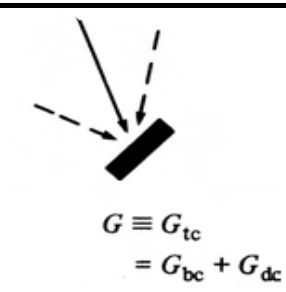


Figure 3.1 Schematic illustration of solar radiation components.

Techniques to measure various components of solar radiation are summarized in table 3.1. Subscripts are used in the following manner: b is used for beam, d for diffuse, t for total, h for the horizontal plane and c for the plane of tilted surface (collector). The asterisk * denotes the plane perpendicular to the beam. Subscript 0 denotes values outside the atmosphere. If no subscripts are given, c and t are assumed then, so that $G=G_{tc}$.

Table 3.1 Solar radiation components techniques of measurement
 (Twidell. JW, Weir. AD, 2006)

	Perpendicular to the sun's beam	Horizontal	At the slope of a collector
Diffuse blocked			
Beam blocked			
Total			

From the table above we can write:

$$G_{bc} = G_b^* \cos\theta \quad (3.1)$$

Where θ is the angle between the beam and the normal to the collector (e.g. PV module or panel) surface. In particular,

$$G_{bh} = G_b^* \cos\theta_z \quad (3.2)$$

Where θ_z is zenith angle between the beam and the vertical. The total irradiance on any plane is the sum of the beam and diffuse components.

$$G_t = G_b + G_d \quad (3.3)$$

3.3 Measurements of solar radiation

The most common instruments used to measure solar radiation are the pyroheliometer which measures the beam irradiance G_b^* , and the pyranometer or solarimeter which measures the total irradiance G_{tc} .

In our case, only the total on the PV panel surface (global) irradiance was measured by means of a Kipp & Zonen CM11 pyranometer. Detailed specifications and characteristics can be found in (Mokeddem. A et al, 2011).

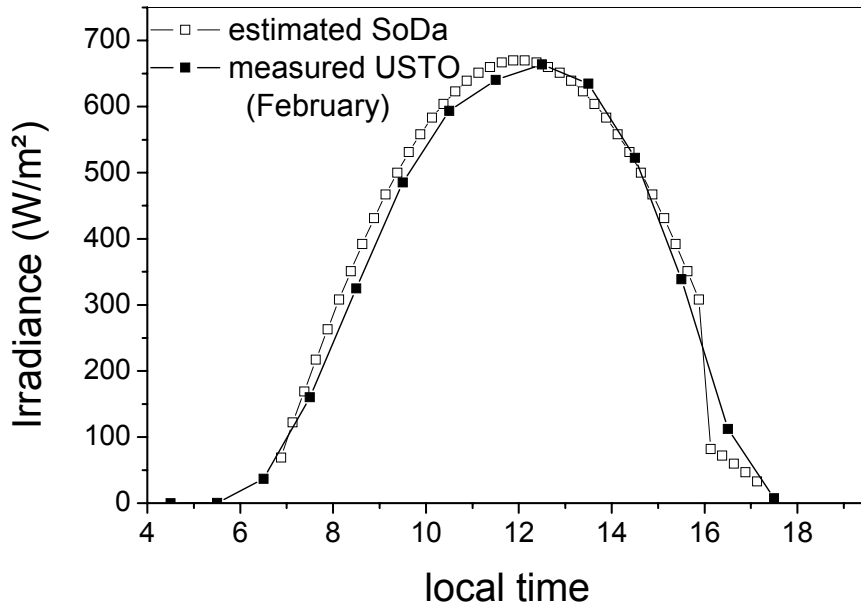


Figure 3.2 Mean hourly irradiance measured and estimated (SoDa).

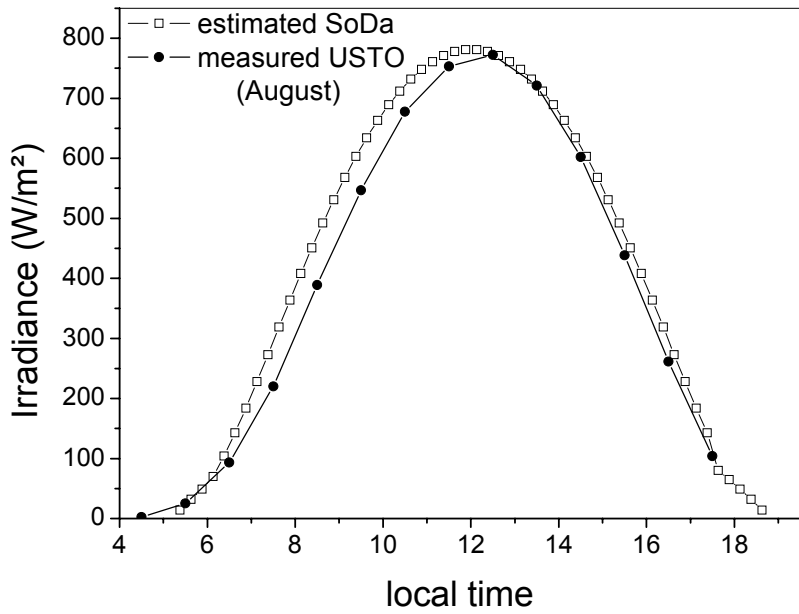


Figure 3.3 Mean hourly irradiance measured against estimated (SoDa).

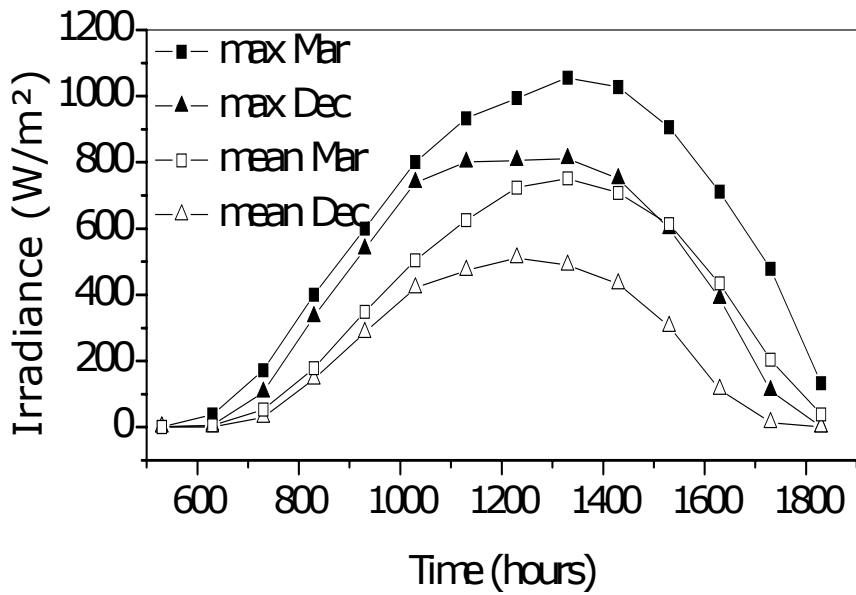


Figure 3.4 Typical solar irradiance measurements at USTO adopted from (Mokeddem. A et al, 2007)

In figures 3.2 and 3.3 are plotted mean values of solar irradiance measured at the university of science and technology site from 1993 to 1997 more less continuously. The data were recorded via data acquisition

system. The graphs show a fairly good match with the SoDa (<http://www.soda-is.com>) estimations. The SoDa solar irradiance prediction uses the Heliosat modeling procedure, which consists of statistical modeling procedures combined with terrestrial measurements and satellite observation. It can be noticed that the SoDa, Heliosat combined method tends to overestimate the hourly total irradiance on tilted south facing surfaces, especially in the first half of day period. Figure 3.4 shows a comparison between means and maximum values of total irradiance on tilted surface for two months, the tilt angle was taken equal to the latitude of Oran (USTO).

3.3.1 Typical meteorological year

Solar systems simulation faces a major problem which is the very important quantity of meteorological data needed in order to estimate long term performance. A long term has been defined as a period of time sufficient to describe the system performance in a climate, generally a period of one or more years.

Meteorological data needed for a simulation is closely linked to what the simulation does. In a design simulation for instance, long term refers to a period equivalent to, representative of, the expected life of the system. This may be ten to twenty years. Nowadays a variety of computer simulations and simplified procedures exist (e.g. PVSYST). Comparison between different computer codes is difficult, unless the same parameters and data are used (Tiba. C, Barbosa. EM, 2002). Since it is seldom that more than one year of weather data is used in any of those simulations, it would be advantageous if a common weather year would be agreed upon.

Klein, et al (Klein. SA, Beckman. WA, Duffie. JA, 1975) have investigated the problem of the amount of meteorological data required by the simulation in order to estimate long term performance of a solar heating system. They examined the simulated performance of four systems calculated at half hourly intervals for a period of eight years using

meteorological data for Madison Wisconsin. They then compared the average performance of each system for the eight year period with the performance calculated for an average year of the eight years. They found that the eight year average performance of a small system was reasonably close for all months to that calculated for the average year. However, as the system size was increased, the differences between the eight year average and the average year values increased.

The most common data for describing the local solar climate is through what is called Typical Meteorological Year data (TMY). To determine TMY data, various meteorological measurements are made at hourly intervals over a number of years to build up a picture of the local climate. A simple average of the yearly data underestimates the amount of variability, so the month that is most representative of the location is selected. For each month, the average radiation over the whole measurement period is determined, together with the average radiation in each month during the measurement period. The data for the month that has the average radiation most closely equal to the monthly average over the whole measurement period is then chosen as the TMY data for that month. This process is then repeated for each month in the year. The months are added together to give a full year of hourly samples.

In selecting a representative year we must bear in mind that, regardless of how the represented year is selected, it cannot be expected to have the same weather sequences as those occurring in the long term. The simulated performance for a typical year may provide a good estimate of the long term system performance, firstly if the weather sequences in the typical year are representative of those occurring in the term, secondly if the system performance is independent of the weather sequences.

TMY data is used for a wide variety of meteorological applications and therefore a large amount of data is usually irrelevant for photovoltaic applications. Of the parameters given, usually only the time and

irradiation figures are used. However, more advanced models also use the temperature and wind speed.

From the data recorded at the University of Science and technology of Oran (latitude angle equal to 35.69° north) during the period 1993-1997, representing hourly irradiance on an inclined plane (35°) facing south, we added up the hourly values for each day, then we added the daily values for each month, and we divided by the number of days in the month. We selected, for each month of the year, that month of data from the multi-year period which most closely corresponds to the monthly averaged daily irradiation. The result is a TMY composed of: January 1996; February 1995; March 1995; April 1996; May 1996; June 1997; July 1996; August 1995; September 1995; October 1995; November 1996; December 1996. Table 3.2 contains values of the monthly averaged daily irradiation, the TMY is identified by bolded value of the chosen month.

Table 3.2 Monthly averaged daily total irradiation on tilted PV panel plane (tilt angle=latitude of USTO, Oran), in $[KJ/m^2/day] \times 10^{-4}$.

Year	Jan	Feb	Mar	Apr	May	Jun	Jul	Aug	Sep	Oct	Nov	Dec
1994	1.43	1.75	2.06	2.16	2.14	2.19	2.13	2.08	2.02	1.47	1.49	1.47
1995	1.42	1.63	1.84	2.11	2.13	2.01	2.16	2.02	1.93	1.68	1.38	0.99
1996	1.06	1.35	1.69	1.80	1.99	2.13	2.01	1.95	1.76	1.78	1.48	1.00
1997	0.99	1.77	2.07	1.66	1.88	2.03	1.83	—	—	—	—	—
Average	1.22	1.62	1.91	1.93	2.04	2.09	2.03	2.01	1.90	1.64	1.45	1.16
Std.dev	0.23	0.18	0.18	0.24	0.12	0.08	0.15	0.06	0.13	0.15	0.06	0.27

The standard deviation is used as a mean to measure the deviation of the solar irradiation value from the average value. The operation is repeated for all months. An example is shown in figure 3.5 for the month of January.

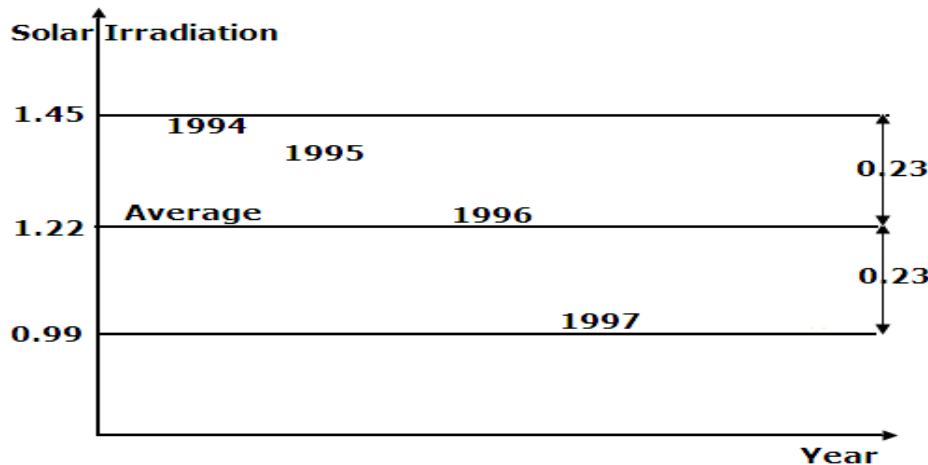


Figure 3.5 Monthly averaged daily total irradiation for January
(Std.dev=0.23), in [KJ/m²/day]x10⁻⁴

3.3.2 Neural network solar data clustering

Another alternative to the construction of TMY is the use of artificial neural network (ANN) which has received wide interest in recent years. Neural networks present another approach to nonlinear data analysis. The idea is to try to find out a way to reduce solar data input to photovoltaic solar system design or system performance analysis, by gathering identical data sequences in a sort of grouping process.

It is used to treat problems not easily affordable by linear methods or by algebraic equations. A neural network consists of a set of elementary processors (neurons), which are connected to each other and are able to exchange information through the connections between them. Connections are directional and to each neuron is associated a real number called weight of the connection, or synaptic weight, which is a measure of the link. To determine the weight a learning process is used. In the learning process, a set of N data statistically representative of the problem is used to specialize the network. When we try to teach a neural network the functional link between two sets of data, learning is said supervised. However, when we seek to analyze the structures of a single data set, learning is said unsupervised, because no prior indication is given to the neural network.

The self-organizing map (SOM) is a kind of artificial neural network that is trained using unsupervised learning to produce a low-dimensional (typically two dimensional) representation of the input space of the training samples, called a map (Kohonen. T, 1995). The Self-Organizing Map (SOM), first introduced by Teuvo Kohonen of Helsinki University of Technology in 1981 (Kohonen. T, 1982) is often used to classify inputs into different categories.

A map in a Kohonen neural network consists of two layers fully connected. The input layer takes the value of vector z (z_1, \dots, z_n) and is used only to introduce the features that each input vector contains to the network for classification, the second layer is a regular lattice (grid) in two or three dimensions, and each of nodes is a linear neuron. This lattice (grid) is a discrete space of small size d , with a topology generated by its structure. We define a discrete distance δ : for any pair of neurons (c, r) of the "map" M , $\delta(c, r)$ is the length of the shortest path between r and c . For each neuron, this discrete distance defines the notion of neighborhood of d order of c , we say then: $V_c(d) = \{r \in M, \delta(c, r) \leq d\}$. The geometry of the lattice (grid) (figure 3.6) defines the type of neighborhood of each neuron.

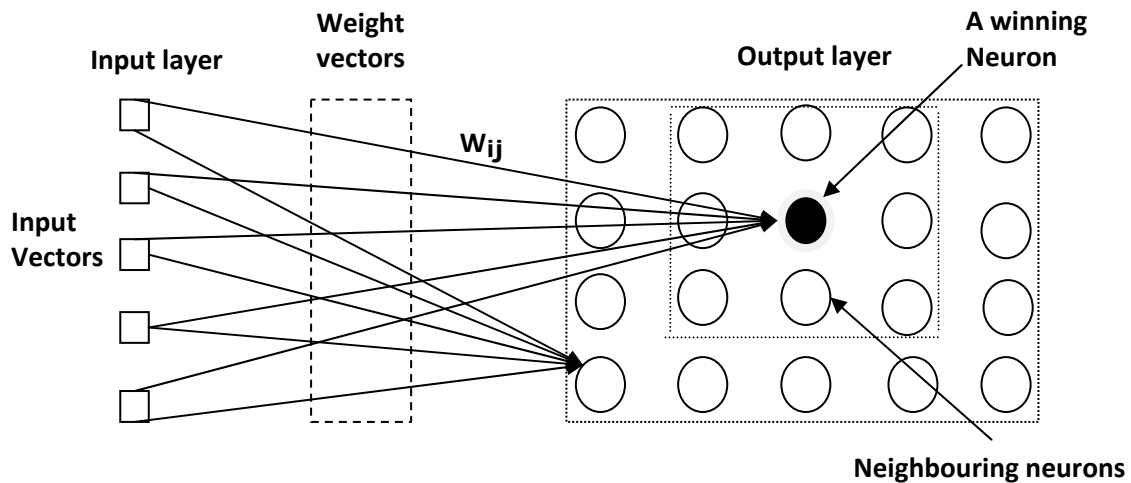


Figure 3.6 The architecture of a 4x5 SOM

Learning:

A Kohonen layer is composed of neurons that compete with each other in a winner-take-all strategy. Inputs are fed into each of the neurons in the Kohonen layer (from the input layer). Each neuron determines its output according to a weighted sum formula:

$$\text{Output} = \sum w_{ij} x_i \quad (3.4)$$

The weights and the inputs are usually normalized, which means that the magnitude of the weight and input are set equal to one. The neuron with the largest output is the winner. This neuron has a final output of 1. All other neurons in the layer have an output of zero. Differing input patterns end up firing different winner neurons. Similar or identical input patterns classify to the same output neuron. We get then, like inputs clustered together (Rao. VB, 1995). This phase is done in an iterative manner. After a random initialization of the weights, an iterative process will take place in two stages: a stage of competition between neurons that determines the region of the lattice that will be adjusted, and a stage of weights adaptation of the selected area to observe projected.

Competition:

At iteration t , neurons of the lattice calculate their state in parallel from a randomly selected observation, $x(t)$, presented as input. Only the most "active" region of the map will have its own weights adjusted. This region is defined by the neighborhood of the closest neuron in the sense of Euclidean distance, the observation $x(t)$. This neuron is called "winner neuron", often noted BMU (Best Matching Unit), and is obtained by:

$$\text{BMU}(t) = \arg(\min_r ||x(t) - w_r||) \quad (3.5)$$

where r is a neuron of the lattice and w_r its referent vector.

Adaptation:

During learning, the BMU neighborhood size, which determines the active zone decreases with time. The change applied to the chosen neighborhood consists of bringing closer weight vectors previously selected. This modification or adaptation of the weights of the active region of the map follows the equation (Xu. R, Wunsch. DC, 2009):

$$w_c^{t+1} = w_c^t + \alpha(t)K^T (\delta(c, BMU(t))) (x(t) - w_c^t) \quad 3.6)$$

Where α is the learning rate which decreases with t and is less than one. The figure (3.7) below illustrates this adaptation phase.

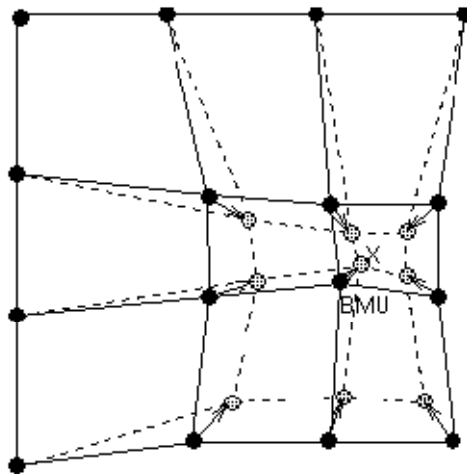


Figure (3.7) BMU adaptation to its neighborhood.

It was aimed in the beginning of this section to find a way to reduce solar data input to the photovoltaic performance global model. One form of reducing data input to the model is to use the TMY to evaluate the yearly performance of any photovoltaic system (Duffie. JA, Beckman. WA, 1980). Despite the fact that TMY represents the most utilized process to estimate long term performance of quite wide range of solar systems. We believe that, in accordance with the fixed objectives of the present research, the TMY data inputs is still a large data feeding to the model, not only in terms of computing time consuming, but also from the fact that we had to have a very fast approach to assess the behavior of the photovoltaic water pumping system. From what have been said, it was decided to have resort

to the neural network clustering technique with the aim of reducing solar irradiance data input to the global model. The self organizing map clustering method is used by means of a simple excel application called TANAGARA (Ricco Rakotomalala, 2005). Other applications have been tested such as NNclust.xls (Saha Angshuman, 2001) and the public domain software package SOM_PAK from the Helsinki University of Technology, laboratory of computer and information science, neural networks research center (Kohonen. T, Hynninen. J, Kangas. J, and Laaksonen. J, 1996). TAGARA offered the best guaranty of convergence with a succession of subroutines to normalizing and preparing data. The SOM clustering processing is a repeated trial procedure which consists of determining an appropriate proximity measure and constructing a criterion function. Intuitively, data objects are grouped into different clusters according to whether they resemble one another or not. Almost all clustering algorithms are explicitly or implicitly connected to some particular definition of proximity measure (Xu. R, Wunsch. DC, 2009). Because of substantial daily amplitude of main meteorological parameters (air temperature, wind speed, solar radiations etc.), it is of interest to get insight into the deviation statistics for diurnal values. Conventional methods of statistical analysis such as, correlation functions and regression analysis ensure exposition only of linear relations. At the same time, most meteorological processes and relationships are referred by their nature to non-linear. The final aim is then, to describe these non-linear processes by modern mathematical methods. The first step should be the classification of basic meteorological parameters diurnal patterns by means of neural networks and fuzzy logic (Pokrovsky. OM, 1998). As mentioned earlier in this chapter, the basis of our research was recorded hourly data for the site of USTO (Oran) during 1993-97. The Input data arrays concerning global solar irradiance on an inclined plan were presented for each month. Each row of the matrix (array) contains diurnal distributions for a certain day of 14 hours, the calculations on a partition of initial sample on a number of classes by means of cluster analysis

described above, were carried out. Calculations allowed us to allocate each class as a set of distributions. The results of the classification are presented below. Average for 4 classes (clusters) distributions are shown in figures 3.8-12, for December, February, June, September and May for comparison. From the obtained results we can formulate the following simple interpretation. The upper curve corresponds to conditions of clear sky, and the lower one to overcast cloud covered sky. Intermediate curves corresponds to conditions of a partly cloud cover, which can vary during the day (e.g. partly cloudy during the first half of a day, and almost clear sky in the afternoon).

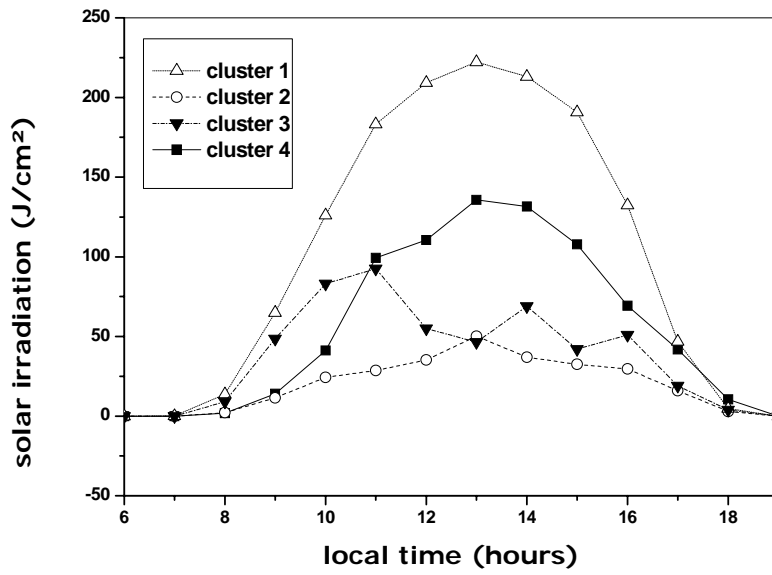


Figure 3.8 Diurnal patterns of global irradiation (4 clusters), December

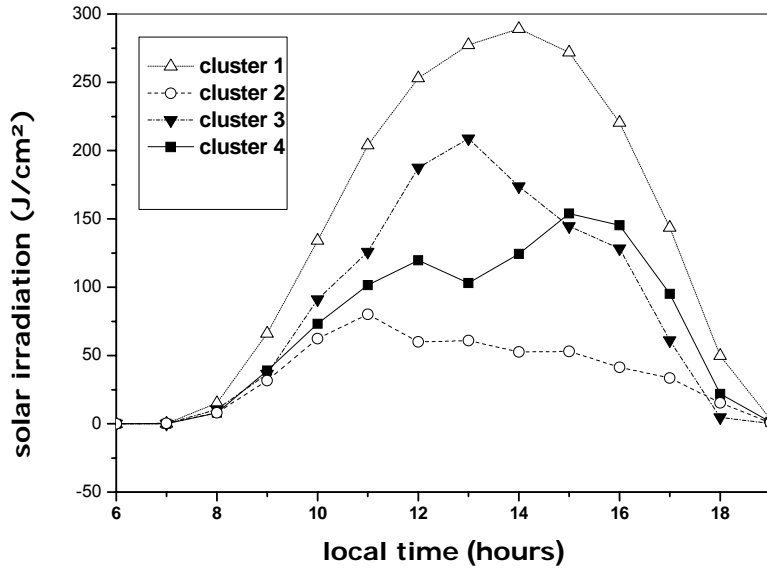


Figure 3.9 Diurnal patterns of global irradiation (4 clusters), February

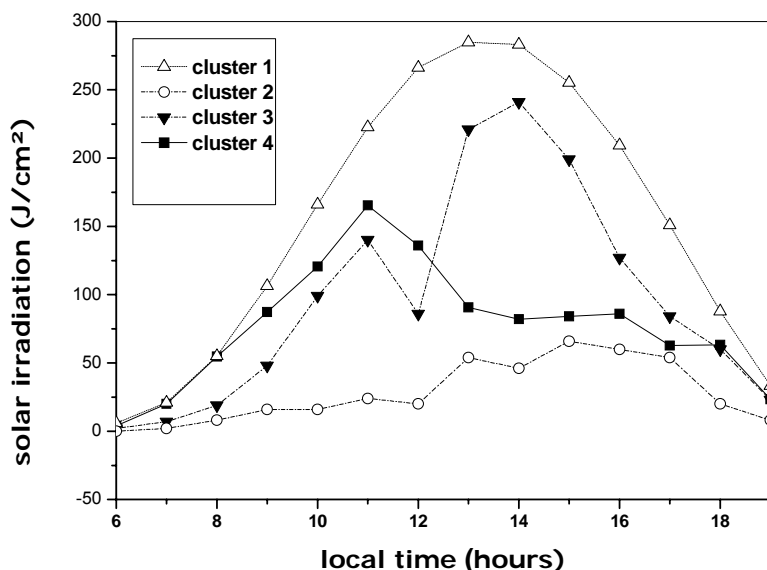


Figure 3.10 Diurnal patterns of global irradiation (4 clusters), June

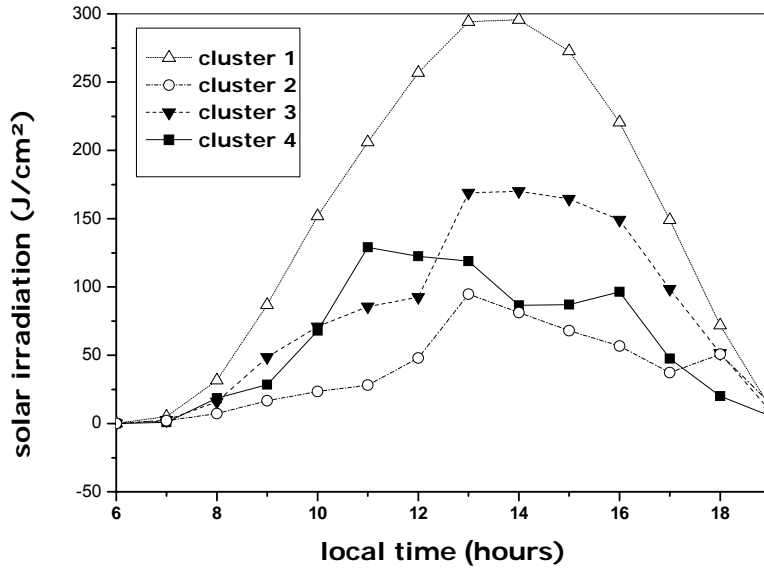


Figure 3.11 Diurnal patterns of global irradiation (4 clusters), September

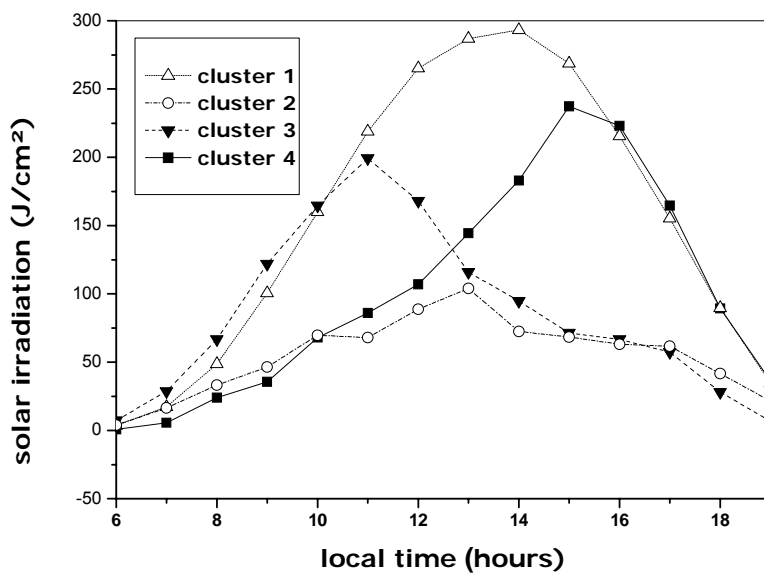


Figure 3.12 Diurnal patterns of global irradiation (4 clusters), May

Classification can be considered representative, not only if the class (cluster) elements have minimal deviation from the centre (mean hourly irradiation for a day), but also if they have the same structure (i.e. maximum and time gradient values). Figures 3.13 (a) and (b) show statistical distribution of the solar irradiance for two different clusters, their centres were given in figure 3.12 above.

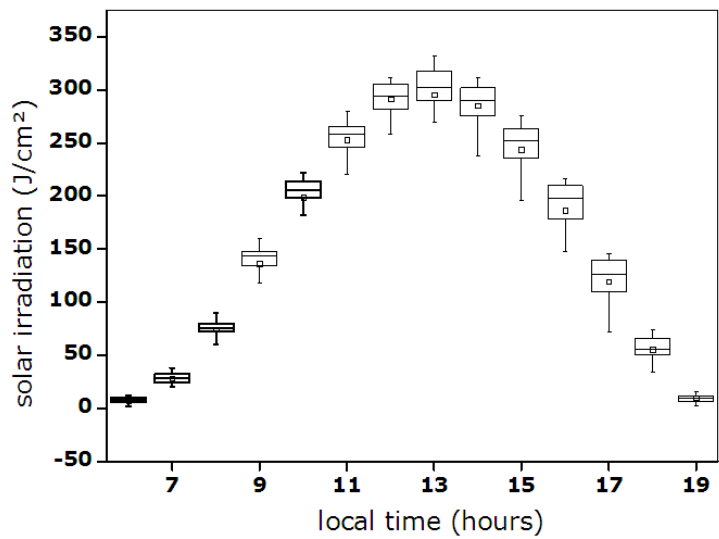


Figure 3.13 (a) Solar irradiation distribution for cluster1 box chart, May.

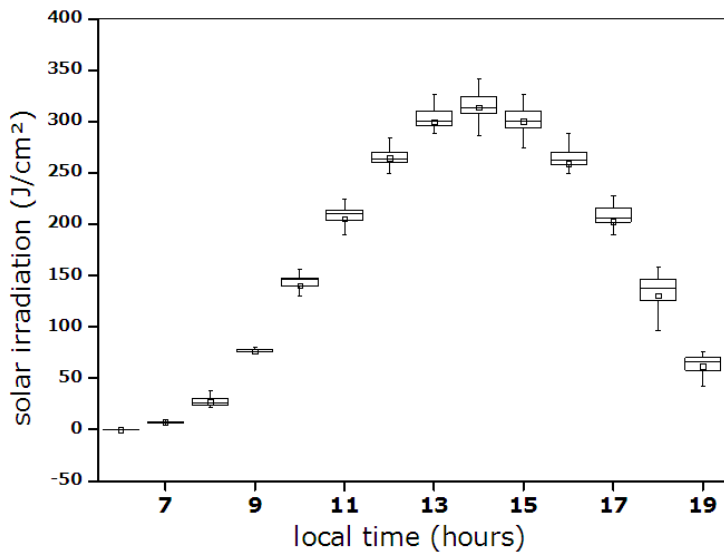


Figure 3.13 (b) Solar irradiation distribution for cluster2 box chart, May.

CHAPTER 4.0

PHOTOVOLTAIC CELL (MODULE) PERFORMANCE MODEL

4.1 Introduction

In any photovoltaic system it is the cell that represents the basic element and not the module; therefore it is necessary to know how photovoltaic cell operates, having said that, we shall consider (as first assumption) through this whole chapter, that all cells of the same module are perfectly identical. The mismatch phenomenon that may take place in photovoltaic panels will not be considered here. The main aim of this chapter is to find a mathematical model describing the behavior of photovoltaic cell, hence module, under different conditions of solar irradiance and cell temperature.

There are many existing models that predict the output of photovoltaic devices. Most of these models need inputs of absorbed radiation and cell temperature. The absorbed radiation can be modeled by a number of radiation models (Duffie and Beckman, 2006). A detailed solar radiation modeling and estimation was realized by the author in his MPhil study. Cell temperature is either assumed equal to the backside panel temperature which is measured, or approximated using empirical (King, 1996), semi-empirical (Skoplaki, 2008), (Del Cueto, 2000), or theoretical (Davis, 2000) heat transfer models.

4.2 Electrical circuit modeling

4.2.1 Photovoltaic effect basics

We will give here, a brief description of the basic processes involved in the photovoltaic effect without going further in details. The definitions and

explanations were compiled from different sources and are meant to be as simple as possible to enable the reader to have a clear idea about photovoltaic effect, knowing that the properties of semiconductor material are described in an ample range of solid state physics and electronics text, (Twidell. JW, AD. Weir, 2006) is one of the numerous references in literature, and one can refer to them whenever the need for greater details is felt.

The electron current flowing from n to p type region in a P-n junction is typically characterized by an exponential dependence, typical for a Boltzmann distribution. This current is referred to as the recombination current, I_r (Van Overstraeten. RJ, RP. Mertens, 1986)

$$I_r = I_0 \exp(-e\Phi/kT) \quad (4.1)$$

Where e is the charge of the electron (1.6×10^{-19} C), Φ is the electric potential difference between the Fermi level and the valence or conduction band as appropriate, k is the Boltzmann constant (1.3854×10^{-23} J/K), I_0 is the saturation current (equals the generation current I_g controlled by temperature. However I_r can be varied by external bias), for good solar cells $I_0 \approx 10^{-8}$ Am $^{-2}$, and T is the absolute temperature.

The Shockley equation (in the dark, no illumination) describes the total dark current as:

$$I_D = I_r - I_g = I_g [\exp(eV/kT) - 1] \quad (4.2)$$

Usually written as:

$$I_D = I_0 [\exp (eV/kT) - 1] \quad (4.3)$$

Sunlight contains photons with energies at wavelength ranging from $0.3\mu\text{m}$ to several μm , figure 4.1 shows solar spectrums.

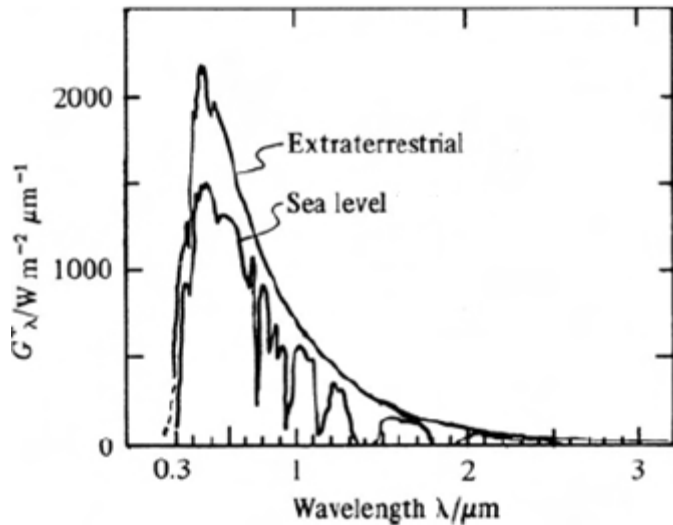


Figure 4.1 Spectral distributions of solar irradiance received above the atmosphere and at sea level, about half the irradiance occurs in the visible region (0.4–0.7 μm) (Duffie and Beckman, 2006).

The energy of any particular photon is given by the product $h\nu$ where h is the Planck constant ($6.63 \times 10^{-34} \text{ Js}$), and ν is the radiation frequency. When $h\nu > E_g$ (E_g band gap) the photon is absorbed by the semiconductor and an electron excited to a level higher by the amount $h\nu$ than its previous level. When the photon energy is less than the band gap, no photoelectric absorption occurs, whereas at photon energy greater than the band gap the excess photon energy is transformed into thermal energy. Band gap absorption occurs at frequencies within the solar spectrum, for silicon (Si) this occurs when:

$$V > E_g/h = \frac{(1.1 \text{ eV})(1.6 \times 10^{-19} \text{ J.eV}^{-1})}{6.63 \times 10^{-34} \text{ J.s}} = 0.27 \times 10^{15} \text{ Hz} \quad (4.4)$$

$$\lambda = \frac{3.0 \times 10^8 \text{ m.s}^{-1}}{0.27 \times 10^{15} \text{ s}^{-1}} = 1.1 \mu\text{m} \quad (4.5)$$

As a conclusion we should say that, generation of carriers in sunlight adds to, and dominates, the thermal generation already present. In dark conditions, of course, only the totally negligible thermal generation occurs. The p-n junction with photon absorption is therefore a DC source of current and power, with positive polarity at the p-type material. Power

generation from a solar cell corresponds to conditions of diode forward bias, as illustrated in figure 4.2 (Twidell.JW, AD. Weir, 2006).

The solar cell current I is determined by subtracting the photon-generated current I_L from the diode dark current I_D (figure 4.2).

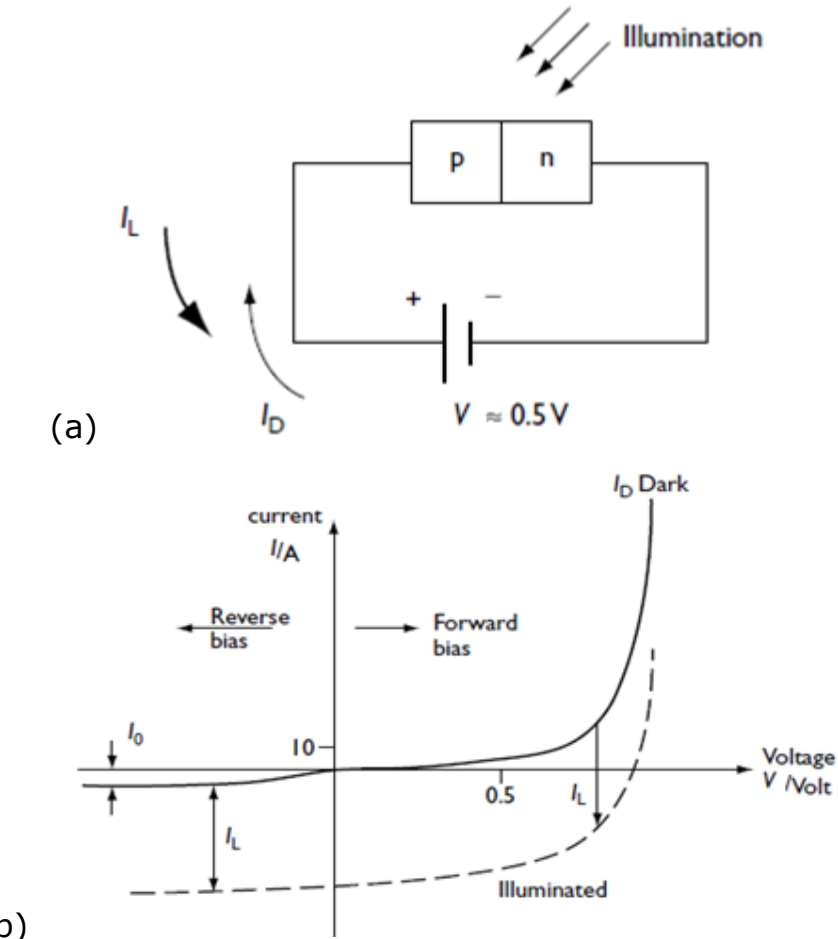


Figure 4.2 (a) Physical set-up of a solar cell. (b) Photovoltaic p-n junction characteristic (Twidell.JW, AD. Weir, 2006).

4.2.2 Photovoltaic solar cell equivalent circuit

In what was said in the previous part of this chapter, we have considered an idealized photovoltaic solar cell. The simplest photovoltaic solar cell model consists of a diode and current source connected in parallel as illustrated in figure 4.3. Current source current (I_L) is directly proportional

to the solar radiation. Diode represents the p-n junction of the photovoltaic solar cell. The ideal photovoltaic solar cell model is then:

$$I = I_L - I_D = I_L - I_0 [\exp(eV/kT) - 1] \quad (4.6)$$

Where: I_L is the photocurrent (A), I_0 is the reverse saturation current (A) (approximately 10^{-8} A/m²), V_D is the diode voltage (V), (kT/e) is the thermal voltage (see equation above).

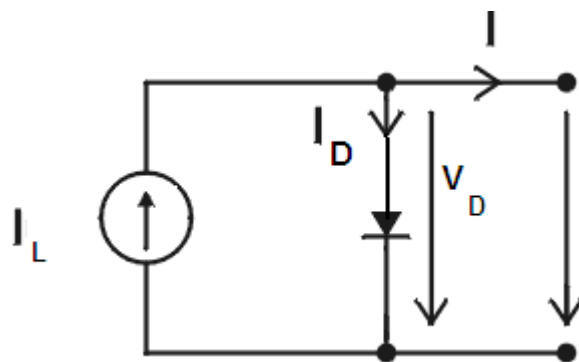


Figure 4.3 Ideal photovoltaic solar cell model (Twidell.JW, AD. Weir, 2006).

In practice however, we must take into account internal resistances such as the series resistance R_s and the parallel (shunt) resistance R_{sh} . The consequence of such consideration is a voltage drop as shown in the figure below.

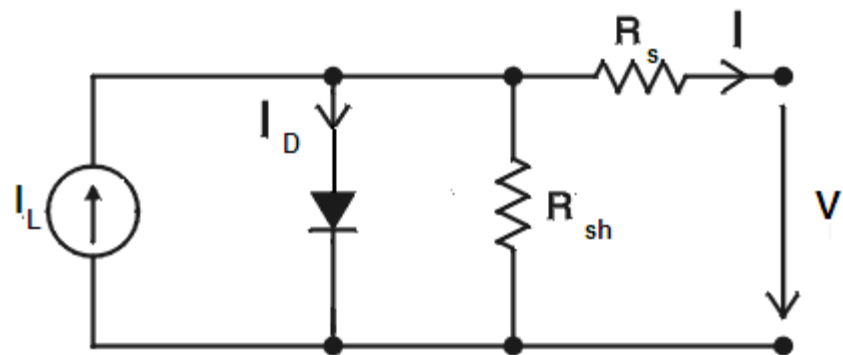


Figure 4.4 Photovoltaic solar cell equivalent circuit (Twidell.JW, AD. Weir, 2006).

From the equivalent circuit (figure 4.4), and from Kirchoff's law of electrical circuits, the output voltage of the photovoltaic solar cell may be expressed as follows:

$$I = I_L - I_D - \frac{V + IR_S}{R_{sh}} \quad (4.7)$$

Following equations 4.6 and 4.7 and by including the voltage drop across R_S we can write:

$$I = I_L - I_O [exp(e(V + IR_S)/AkT) - 1] - \frac{V + IR_S}{R_{sh}} \quad (4.8)$$

Diode factor "A", representing deviation from ideal diode characteristics is introduced at this stage since its inclusion models more exactly actual performance. For most photovoltaic cells $A \geq 1$. For most commercial photovoltaic solar cells $A=1.5$ or 2 . Higher values of "A" produce more curved I-V characteristics, hence, reducing maximum power.

Equation (4.8) is a non-linear function. It is known as the single exponential lumped-constant parameters model and has been accepted as being operationally sufficient to describe the I-V output characteristics of solar cells. The determination of the solar cell equation parameters is important, and must be done, first, if equation (4.8) is to be used in design calculations of PV systems. However, such determination is mathematically difficult and inevitably has to be solved numerically. By looking at the I-V characteristics in figure (4.5) it can be seen that for a particular solar irradiance level, there are two points where the power output from the PV array is nil. When the PV array terminals are disconnected, the current output is equal to zero and voltage is the maximum voltage that the PV array can deliver, and it is called open circuit voltage V_{oc} . When the PV array terminals are shorted and the voltage output is equal to zero, the current is at its maximum and is called short circuit current I_{sc} . Maximum power points for different solar

irradiance are represented by the broken line in figure (4.5), which also represents the optimum line (Peak power line).

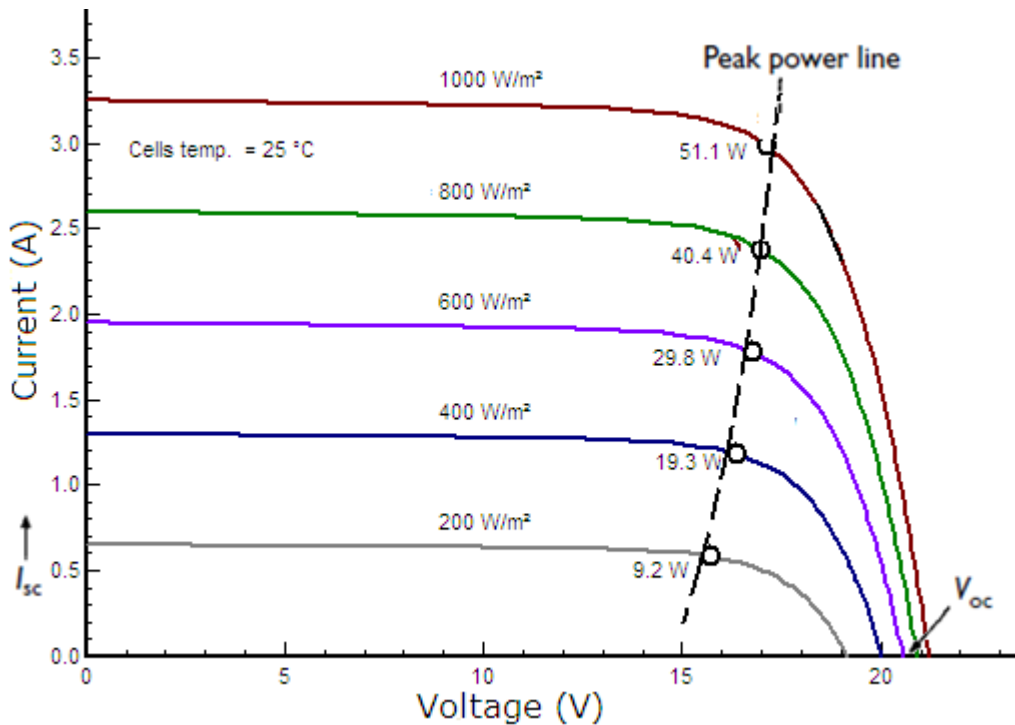


Figure 4.5 Typical I-V characteristic of a Silicon module (Kyocera LA 361 K 51 manufacturer data sheet)

By rearranging equation (4.8) we can suggest an expression of voltage as follows:

$$V = -IR_S + \frac{AkT}{e} \ln \left[\frac{I_L - \left(1 - \frac{R_S}{R_{Sh}}\right)I - \frac{V}{R_{Sh}}}{I_O} + 1 \right] \quad (4.9)$$

Usually, for most cells R_{Sh} is caused by structural defects across and at the edge of the cell, present technology has reduced these to a negligible effect, so shunt resistance may be considered infinite, so that the factor R_S/R_{Sh} and V/R_{Sh} are omitted, therefore

$$V = -IR_S + \frac{AkT}{e} \ln \left[\frac{I_L - I}{I_O} + 1 \right] \quad (4.10)$$

By setting $V=0$, we obtain the following short circuit current expression

$$I_{SC} = I_L - I_O \left[\exp \left(\frac{e}{AkT} I_{SC} R_S \right) - 1 \right] \quad (4.11)$$

In their three methods measurements, Wolff and Rauschenbach found that light generated current I_L is proportional to the intensity of incident radiation up to extremely high light intensities. However, numerous measurements undertaken in order to check this relationship appeared to show deviations, caused by the effect of the series resistance on the short circuit current which had been measured instead of the light generated current. (Wolf. M, H. Rauschenbach, 1963). In conclusion of this study, I_L may be substituted by I_{SC} only in the case of an ideal solar cell with zero R_s or in the case of real solar cell at sufficiently low light intensities only (figure 4.6). At light intensities high enough so that the product of internal series resistance and terminal current exceeds 250 mV, the short circuit current can no longer be considered identical to the light generated current.

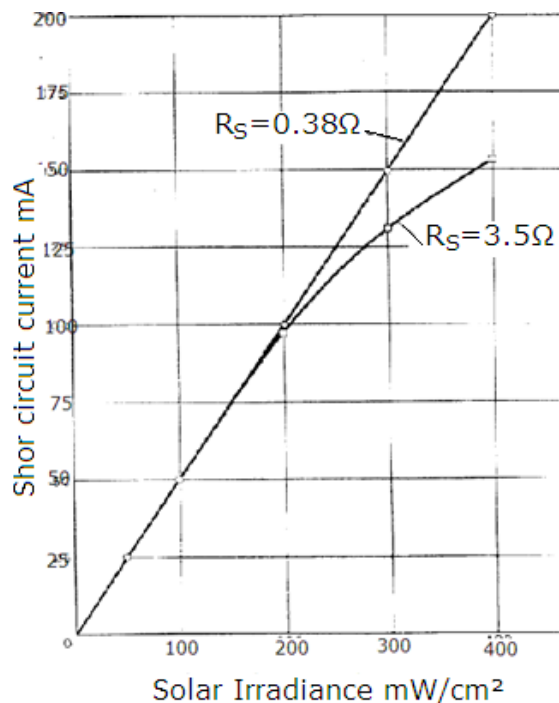


Figure 4.6 Short circuit current versus solar irradiance at two R_s Values (Wolf.M, H. Rauschenbach, 1963)

4.2.3 Series resistance effects

Series resistance can arise from the connecting lead and the metal contact grid. Current collected at the p-n junction must flow in the thin top layer to the closest metal grid line, and this is the resistance path that usually dominates. The path way to the lower layer is less resistive because the contact is of plate geometry covering the whole rear surface of the cell. At high light levels, the effects of series resistance consist in a flattening of the photovoltaic characteristic and hence, a drop in the maximum power point voltage (Takahashi K, Konagai M, 1983). Significant improvements have now been made in forming these contacts, for instance forming laser-cut channels into which thin contacts can be formed, and arranging the surface layout to minimize the top surface series resistance to $\sim 0.1\Omega$ in a cell resistance (Twidell JW, Weir AD, 2006).

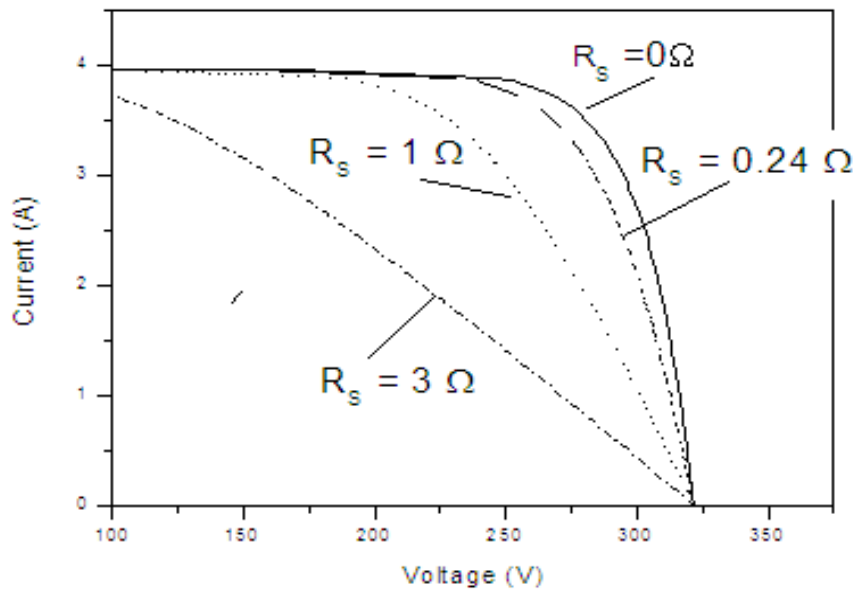


Figure 4.7 Series resistance effect on PV characteristic (simulated)

Figure 4.7 shows the effect of series resistance on the PV characteristic of the whole array at 600 W/m^2 solar irradiance value (the array used in this work is made from 15×15 kyocera modules with a manufacturer series resistance value equals to 0.24Ω). It can be seen that low series resistance array has a more square characteristic. This means that there

is a high power output, at low series resistance because there is less energy loss, the PV characteristic knee where the maximum power point is localized has square shape. We can say that, R_S has a more localized influence around the maximum power point. Values of 1 and 3 Ω series resistance values are utilized for comparison. In figure 4.8 below, manufacturer experimental test results investigating the series resistance effect on module IV characteristic at 1000 W/m^2 irradiance value and 40°C module temperature are shown. It can be noticed that no excessive values for R_S are taken ($0.2 \Omega \leq R_S \leq 1.0 \Omega$).

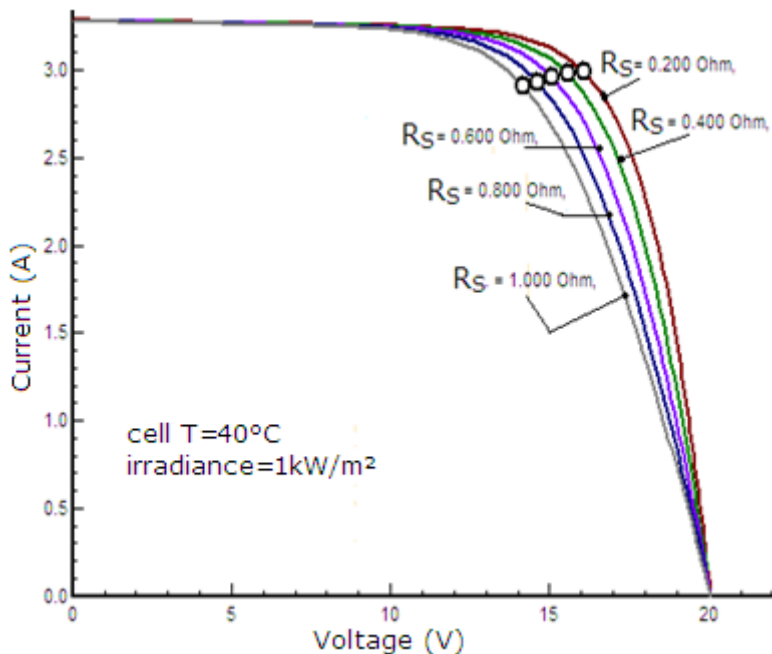


Figure 4.8 Effect of series resistance on Kyocera LA 361K51 module(Manufacturer test data sheet)

4.2.4 Shunt resistance effects

Parallel or “shunt” resistance occurs between the terminals of each photovoltaic cell, it can be described as the cell proper resistance. If shunt resistance, as most manufacturers confirm, is too low, so-called shunt currents appear and flow in the cell itself without leaving it. In fact the term “shunt” is used to describe all types of local leakage currents in solar cells. Low shunt resistance act on bending the cell I-V characteristic

downwards, thus, reducing the fill factor "FF". The fill factor illustrated in figure (4.9) could be written as follows:

$$FF = \frac{I_{MP} \cdot V_{MP}}{I_{SC} \cdot V_{OC}}$$

In their newly inaugurated (2011) outdoor test facility in Aachen (Germany), PHOTON laboratories have been looking closely to the effect of series and shunt resistance on photovoltaic solar cells efficiency, the modules tested were of different technology, they came out with the conclusion that shunt resistance(considered as defect) is mainly caused by poor edge insulation, small cracks in the cell, aluminum particles on the surface or accumulations of contaminants at grain boundaries in multicrystalline cells. Shunt resistance relatively negative influence on cell efficiency appears at low solar irradiance levels in particular. In our case shunt resistance effect was neglected considering that the value of R_{Sh} was sufficiently high 350Ω , so that the term $\frac{V+IR_s}{R_{sh}}$ in equation (4.8) could be omitted. Comparison of the effect of series resistance and shunt resistance on the photovoltaic solar cell characteristic is illustrated in figure (4.10). Other methods to calculate series and shunt resistance can readily be found in literature, one of the simplest, though, is to measure solar I-V characteristic slopes at V_{OC} and I_{SC} , to get approximate values of R_s and R_{Sh} respectively.

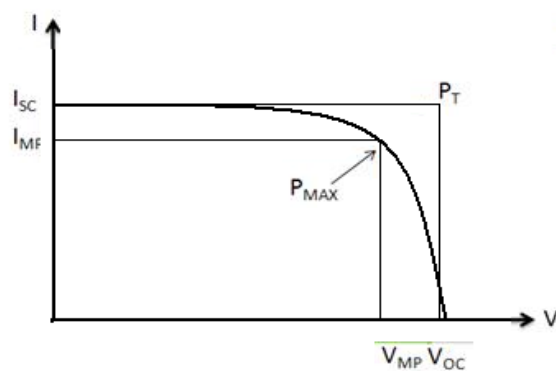


Figure 4.9 Schematic illustration of the fill factor.

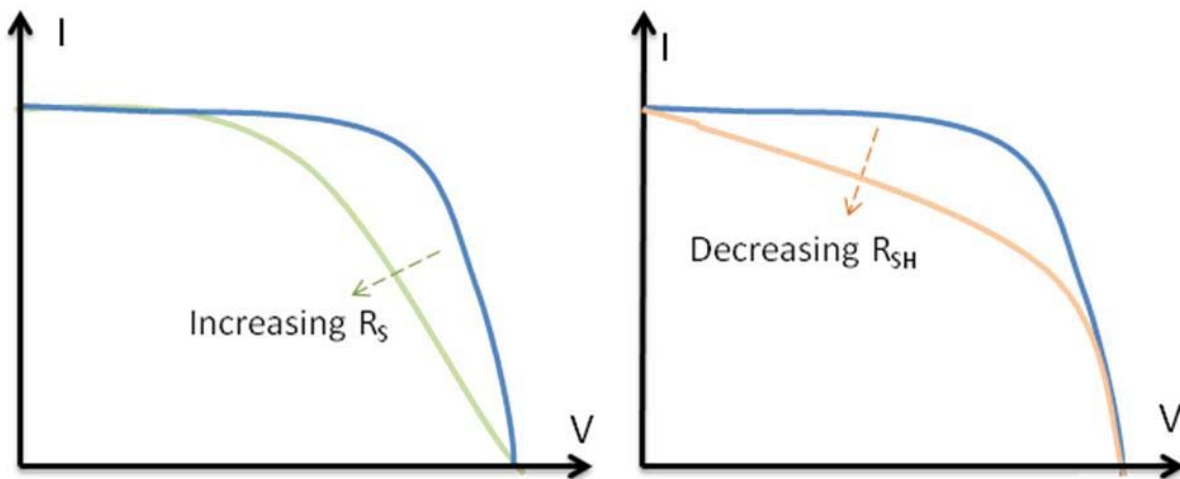


Figure 4.10 Effect of R_s and R_{sh} on cell characteristic and on fill factor
in particular (National Instruments LabVIEW for photovoltaic
Solar Cell characterization web site)

4.2.5 High temperature effect on PV cell performance

It is useful to understand the effect of the irradiance and temperature on the solar cell and module performance, in order to estimate their performance under various climate conditions. Manufacturers' data sheets normally show the rated performances for cell temperature of about 25°C and global irradiance values of 1000 kW/m² (e.g. table 4.1), which under real climatic conditions is rather unrealistic.

Temperature effect on cell performance (efficiency in particular) differ from one cell material to another, when the surface of the cell is hit by solar irradiation, the excess photon energy not contributing in current generation is transformed into heat, rising by then the cell temperature, an indicative relationship is depicted in figure 4.11, where a decrease in cell efficiency with increasing temperature is noticeable.

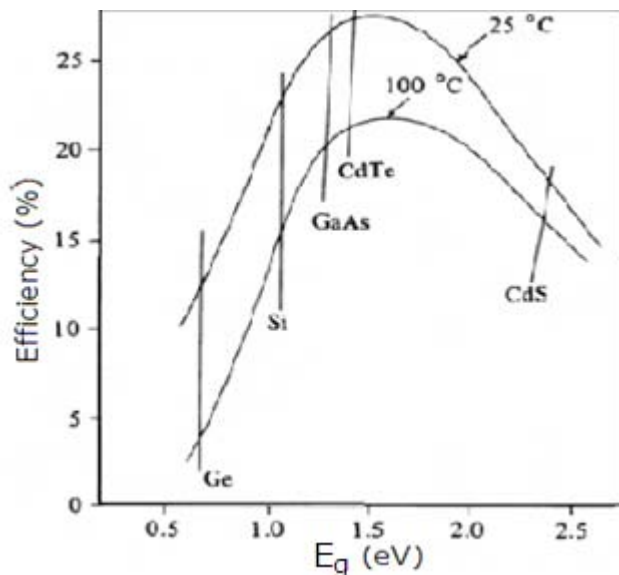


Figure 4.11 Solar cells theoretical efficiency versus band gap at 25 °C and 100 °C (Twidell. J. W, A. D. Weir, 2006)

Table 4.1 Characteristics of PV module "KYOCERA LA 361K51" at Standard Conditions (25 °C, 1000 W/m²)

Short circuit current	3.25 A
Open circuit voltage	21.2 V
Maximum power point voltage	16.9 V
Maximum power point current	3.02 A
Maximum power	51 W
Temperature coefficient (short circuit current)	2.3 mA/°C
Temperature coefficient (open circuit voltage)	-76 mV/°C
Diode quality factor	1.35
Series resistance	0.24 Ω
Shunt resistance	350 Ω
Efficiency (module area)	11.7 %
Fill factor	0.742

Like all other semiconductor devices, solar cells are sensitive to temperature. Increases in temperature reduce the band gap of a semiconductor, thereby effecting most of the semiconductor material parameters. The decrease in the band gap of a semiconductor with increasing temperature can be viewed as increasing the energy of the electrons in the material. Therefore increasing the temperature reduces the band gap. The short-circuit current, I_{SC} , increases slightly with temperature, since the band gap energy, E_g , decreases and more photons have enough energy to create electron-hole pairs. However, this is a small

effect. The parameter most affected by an increase in temperature is the open-circuit voltage. The open-circuit voltage decreases with temperature because of the temperature dependence of I_O from equation 4.10 if I is set equal to zero, then the open circuit voltage is:

$$V_{OC} = \frac{AkT}{e} \ln \left[\frac{I_L}{I_O} + 1 \right] \quad (4.12)$$

It was found in the very extensively available documentation on semiconductors and materials that I_O and E_g are exclusively material dependant parameters, and that for silicon solar cells near room temperature, I_O approximately doubles for every 10 °C increase in temperature. The dependency of V_{OC} on temperature for silicon could be expressed by: $\frac{dV_{OC}}{dT} \approx -2.2 \text{ mV/}^\circ\text{C}$ (4.13)

The short circuit dependence on temperature, however may be written in the following form: $\frac{1}{I_{SC}} \frac{dI_{SC}}{dT} \approx 6.10^{-4} \text{ per } ^\circ\text{C}$ (4.14)

The cell temperature must be determined experimentally and depends on the solar insolation, the ambient temperature, the wind speed and the type of encapsulation. A comprehensive study is presented by King (King. DL, 1996), other simple approximations for the determination of the operation temperature have been published (Schott T, 1985), (Risser et al, 1983), (Siegel MD, Klein SA and Beckman WA, 1981) and (Khallat MA, Rahman S, 1986), in our research, we restricted the effect of weather conditions on cell (module, array) temperature to the solar irradiance and ambient temperature only.

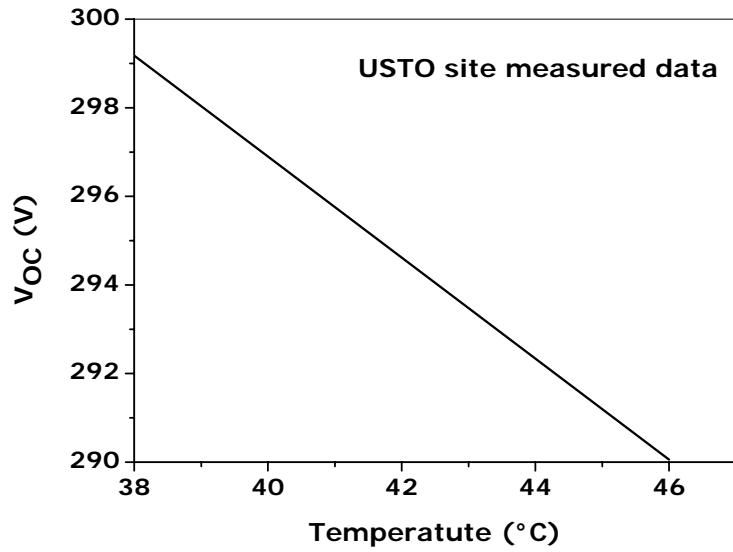


Figure 4.12 Temperature effect on open circuit voltage (array scale)

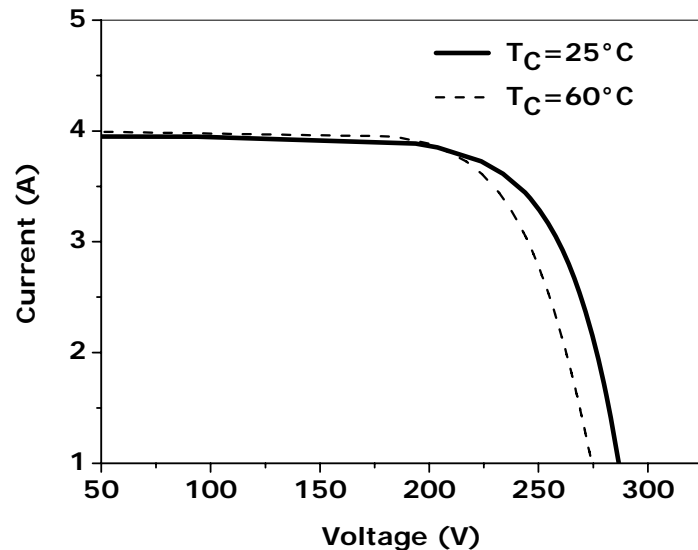


Figure 4.13 I-V characteristics for different temperatures (simulated)

4.3 Photovoltaic performance final model

The behavior of a solar cell was described by equation (4.8) if we make the following assumptions:

- The photocurrent is equal to the short circuit current (for moderate series resistance)
- The factor $\frac{V+IR_S}{R_{sh}}$ is negligible (shunt resistance very large)
- The saturation current I_0 and diode factor A used in equation (4.8) are constant
- The standard conditions are 25°C for cell temperature and 1000kW/m² for solar irradiance

Then equation (4.8) reduces to:

$$I = I_{SC} - I_0[\exp(e(V+IR_S)/AkT)-1] \quad (4.15)$$

Applying open-circuit conditions to equation (4.15), eliminates the effect of R_S which is the main cause of deviation between the experimental and theoretical I-V curves. Since the photocurrent in a non-concentrating optical system equals the short-circuit current and is proportional to solar irradiance (Hsiao YR, Blevins BA, 1984) we can then, write the following equation:

$$V_{OC}(G,25) = (1/B)\ln[G I_{SC}(1,25)/I_0] \quad (4.16)$$

Where G is the effective irradiance, $B=e/AkT$. The reverse saturation current can I_0 be calculated only once, since it represents the dark diode junction property, hence, independent of irradiance. Again by imposing the open-circuit conditions on equation (4.3.1) at STC we obtain:

$$I_0 = I_{SC}(1,25) \exp[-BV_{OC}(1,25)] \quad (4.17)$$

In our case $I_0 = 137$ nA. The proposed model describes then the solar cell I-V characteristic by:

$$I = I_{SC} (1 - \exp[-(V_{OC} - V)/C]) \quad (4.18)$$

Where C is a curve-fitting constant expressed in volts and its value is chosen such that equation (4.18) satisfies the maximum power point at STC, another model (Weiner D, Levinson A, 1996) used two curve-fitting constants. At maximum power point $I=I_m$, $V=V_m$, equation (4.18) solved for C, gives:

$$C = (V_{OC} - V_m) / \ln[I_{SC}/(I_{SC} - I_m)] \text{ at STC} \quad (4.19)$$

The model was developed on the basis of the analogy that exists between the I-V characteristics of a solar cell and the rise of current in an inductive circuit (Hamdy MA, 1994). The reason of the choice of this model was mainly dictated by its simplicity and reliance on limited manufacturer data, the model has also shown good agreement between manufacturer and calculated data for a KYOCERA LA 361J51 module. A modification was, though introduced concerning the effect of temperature on module short circuit current, which was originally neglected.

From equations (4.18) and (4.19) it can be seen that the model requires three data characteristic points of the solar cell to be defined: V_{OC} , I_{SC} , and (V_m, I_m) . Once the value of C is calculated from equation (4.19) at STC from data provided by the manufacturer (in our case $C=1.6236$ V), C can then be substituted in equation (4.18) to generate the I-V curve of the solar cell, module or the array. This can be done simply by scaling the I-V curves of each individual cell by multiplying the voltage by the number of cells in series and the current by the number of strings in parallel.

The effect of solar irradiance and temperature on V_{OC} , I_{SC} and, hence, on I-V curves is introduced by the following equation:

$$I_{SC}(G,T) = GI_{SC}(1,25) + \alpha(T_C - 25) \quad (4.20)$$

$$V_{OC}(G,T) = (1/B) \ln[GI_{SC}(1,25)/I_0] + \beta(T_C - 25) \quad (4.21)$$

Where T_C is the cell temperature in $^{\circ}\text{C}$, the short circuit current temperature coefficient $\alpha=2.3$ mA/ $^{\circ}\text{C}$, and, the open-circuit voltage coefficient $\beta=-76$ mV/ $^{\circ}\text{C}$. T_C depends, evidently on, solar irradiance, ambient temperature T_a , and wind speed, a comprehensive study is presented by King (King DL, 1996), we restricted the effect of weather conditions on T_C to the solar irradiance and ambient temperature only, which gave rise to the following relation:

$$T_C = T_a + 30G \quad (4.22)$$

The cell temperature in equation (4.22) is used as a close approximation of the back surface temperature of the module or the array, even though, 2–3 °C difference for wind speed less than 3 m/s were recorded (King DL, 1996). Based on experimental measured data at USTO, this equation represents the linear regression of the array temperature versus the global irradiance. Mean ambient varied from 19 to 22°C during spring.

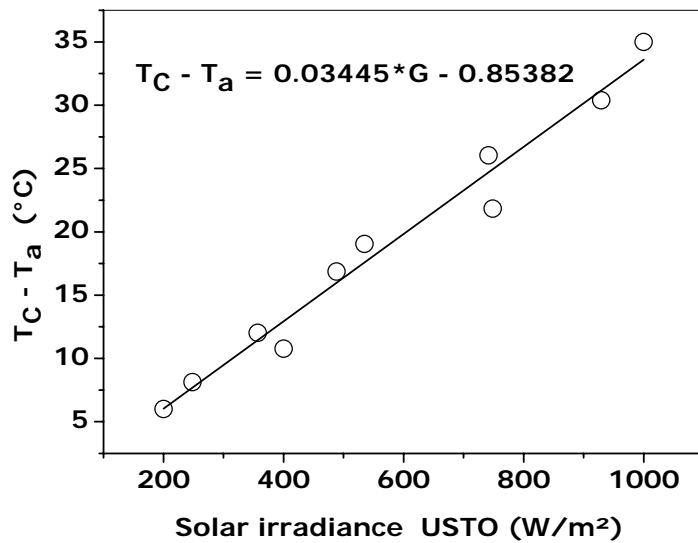


Figure 4.14 Array temperature against irradiance (recorded at USTO)

CHAPTER 5.0

D.C. MOTOR PERFORMANCE MODELING

5.1 Introduction

Although it was intended (as main goal of the LEPES research program framework) to test a wide range of operating photovoltaic pumping systems comprising, AC motors (one and three phase) and DC motors driving one and multistage centrifugal pumps, we have been able to realize only the latter form of the testing program.

Consequently, only permanent magnet DC motors are considered. Steady state operation mathematical model is presented. The motor performance is expected to be different from that with conventional constant voltage, since the photovoltaic array can be described as a nonlinear and time dependant power source with an output depending on solar irradiance. Theoretical analysis is undertaken to have a better understanding of motor operating most influential parameters.

5.2 D.C. motor theory

Direct current motors may be categorized in three types by the manner in which the field and armature circuits are connected to each other:

- (i) Separately excited, (ii) shunt and (iii) series D.C. motors. Permanent magnet DC motors are classified in the first category.

5.2.1 Motor torque constant

The rotor of a DC motor or armature is the part of the motor that carries the current that interacts with the field flux to create the torque.

The torque working on the rotor is written as follows:

$$T_M = ZRBIL = ZRB I_a / 2 \quad (5.1)$$

Where Z is the total number of conductors, B is the magnetic flux density (Tesla), L is the effective length of the conductor, R is the distance from the centre of the coil to each conductor (diameter of rotor shaft) , I is the electrical current flowing through the conductor and I_a is the current from the motor terminal which is equal to $2I$ (Kenjo T A, Nagamori S, 1985). The magnetic flux is equal to:

$$\emptyset = \pi RLB \quad (5.2)$$

From equations (5.1) and (5.2), we can write

$$T_M = \frac{Z}{\pi} \emptyset \frac{I_a}{2} \quad (5.3)$$

Z is a fixed number for a particular motor, \emptyset determines the motor dimensions and state of magnetization, the factor Z/π is a fixed value. Therefore the torque T_M can be considered as a proportional function of armature current I_a , and can be written as:

$$T_M = K_{Tp} I_a \quad (5.4)$$

K_{Tp} is defined as the torque constant and has as unit N.m.A⁻¹ .

5.2.2 Rotational speed constant (or back e.m.f constant)

A conductor placed in a magnetic field with a current flowing through it, is moved by a force at a speed v . Since the conductor now passes through the magnetic field, an electromotive force E is generated in the conductor. The magnitude of this force is:

$$E = v BL \quad (5.5)$$

Relation (5.5) is known as Faraday's law and has a direction determined by the right-hand rule, i.e. the direction in which the electrical power is generated is opposite to the direction of the current, so as to oppose its flow. If the rotor is revolving at a speed ω (rad/s) and if the total number of conductors is Z ($Z/2$ is the number of conductors in a series connection), then the total back e.m.f at the motor terminal is:

$$E = \frac{\phi Z}{2\pi} \omega \quad (5.6)$$

Where Φ is the magnetic flux and v is equal to $R\omega$.

The electromotive force changes as each conductor passes through the north and the south pole successively. The commutator and brushes make the electromotive force on each coil merges to the motor terminals. The direction of this force is opposite to the terminal voltage applied and its magnitude directly proportional to the rotational speed.

$$E = K_{Sp} \omega \quad (5.7)$$

Where $K_{Sp} = (Z/2\pi) \Phi$ is called rotational speed constant or back e.m.f constant and has as unit $V.s.rad^{-1}$, for permanent magnet DC motors K_{Tp} and K_{Sp} have the same value.

5.3 Motor performance

A permanent magnet DC motor equivalent circuit as shown in figure (5.3.1) comprises a voltage source in series with the motor's armature resistance R_a , and the back e.m.f E , generated by the rotating armature.

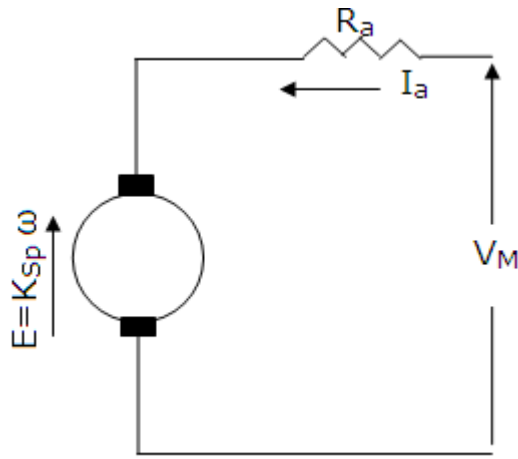


Figure 5.1 Equivalent circuit of a D.C. motor

From the equivalent circuit above, the motor can be modeled by the following equation:

$$V_M = R_a I_a + K_{Sp} \omega \quad (5.8)$$

Where R_a is the motor armature current, the armature current may be written as follows

$$I_a = \frac{V_M - K_{Sp} \omega}{R_a} \quad (5.9)$$

Therefore, equation (5.2.1.4) can be rewritten under the new following form:

$$T_M = K_{Tp} I_a = \frac{K_{Tp}}{R_a} (V_M - K_{Sp} \omega) \quad (5.10)$$

It can be noticed that the above equation encloses within it all motors parameters.

5.3.1 Rotational speed characteristic

This characteristic expresses the rotational speed as a function of the motor current and is defined from equation (5.8).

$$\omega = \frac{V_M - IR_a}{K_{Sp}} \quad (5.11)$$

V_M is the voltage applied to the motor terminals, I is the load current. From equation (5.11) it is possible to determine the motor rotational speed for a specific load current, by substituting the value of the voltage V_M into equation (5.11).

5.3.2 Rotational speed torque characteristic

This characteristic is represented by the rotational speed as a function of the torque. The current I from equation (5.11) is substituted by its value from equation (5.10) we obtain the following expression:

$$\omega = \frac{V_M - \frac{T_M}{K_{Tp}}R_a}{K_{Sp}} \quad (5.12)$$

Relation (5.12) gives the rotational speed of motor as a function of the load torque and the applied voltage.

Motor parameters are essential inputs to performance prediction, usually values such as the armature resistance R_a , the torque constant K_{Tp} and the rotational speed constant K_{Sp} are supplied under the form of technical data sheet by the manufacturer.

Since we put ourselves through this whole project in the situation where components of the system, such as the motor or the pump may be off-the-shelf, therefore their characteristics are unknown to the user. These characteristics can, nonetheless be calculated or measured.

5.3.3 Calculation of K_{Tp} and K_{Sp}

From the motor back e.m.f equation $E=K_{Sp}\omega$, it can be seen that at starting the motor back e.m.f is initially zero and builds up as the speed

builds up. The armature current may therefore be very large initially since it is limited only by the very small armature resistance R_a . Thus, at stall condition we have $E=0$ and $\omega=0$, so, from equation (5.10) we obtain the torque at stall condition, which provide us with a mean of calculating the motor torque constant from measured parameters:

$$K_{Tp} = \frac{T_{Sp}}{V_M} R_a \quad (5.13)$$

Where T_{Sp} is the torque at stall condition

At open circuit or no-load condition we have $\omega=\omega_0$, $T_M=0$ and $I_a \approx 0$, so $E=V_M$. From these conditions it is possible to compute the value of the motor rotational speed constant, which is equal to:

$$K_{Sp} = \frac{V_M}{\omega_0} \quad (5.14)$$

ω_0 is called the ideal no-load rotational speed, and can be quite high. The voltage V_M in equation (5.13) and (5.14) is the voltage supplied to the motor at stall condition and at no-load condition respectively.

5.4 D.C. motor and PV array direct coupling

It is known that photovoltaic solar module is a nonlinear and time dependent current source. Therefore, it is expected that a system powered by photovoltaic solar panels performs differently from that supplied by conventional constant voltage source. The voltage, at which a system powered by PV panels operates, is a function of the current required by the load. We shall consider throughout this work that there will be no power loss between the PV array and the DC motor, and thus

the voltage across the motor armature is equal to the voltage supplied by the photovoltaic array $V_M = V$, and the current flowing in the motor armature is the same as the current delivered by the photovoltaic array $I_a = I$.

The motor rotational speed-torque equation at steady state is given by equation (5.12), and since the photovoltaic output voltage is a nonlinear function of the current and represented by equation (4.10), we can then rewrite equation (5.12) in the following form:

$$\omega = \frac{1}{K_{Sp}} \left[\frac{AkT}{e} \ln \left(1 + \frac{I_L - I}{I_0} \right) - I(R_S + R_a) \right] \quad (5.15)$$

By substituting the current from the motor torque equation (5.10) into equation (5.15) we get:

$$\omega = \frac{1}{K_{Sp}} \left[\frac{AkT}{e} \ln \left(1 + \frac{I_L - T_M / K_{Tp}}{I_0} \right) - \frac{T_M}{K_{Tp}} (R_S + R_a) \right] \quad (5.16)$$

Relation (5.16) represents then, the permanent magnet motor rotational speed-torque characteristic with the light generated current I_L as a parameter. Since the latter is proportional to the solar irradiance, we can now define a set of curves for each value of the solar irradiance (G). Evidently these curves are drawn in the mechanical plane (ω, T_M) .

At this point it is relevant to define two particular motor rotational speed values, namely the so-called “no-load” rotational speed or the ideal speed (ideal because it is the maximum value) and the so-called “no-voltage” rotational speed. The ideal “no-load” speed is calculated by setting the current to zero in relation (5.15).

$$\omega_0 = \frac{1}{K_{Sp}} \left[\frac{AkT}{e} \ln \left(1 + \frac{I_L}{I_0} \right) \right] \quad (5.17)$$

The “no-voltage” rotational speed is obtained from relations (4.10) and (5.15). By setting V equal to zero in relation (4.10) we get:

$$I_{SC}R_S = \frac{AkT}{e} \ln \left[\frac{I_L - I_{SC}}{I_O} + 1 \right] \quad (5.18)$$

Substituting relation (4.18) in (4.15) we obtain:

$$\omega_{v=0} = \frac{1}{K_{Sp}} [I_{SC}R_S - I_{SC}(R_S + R_a)] \quad (5.19)$$

Thus, $\omega_{v=0} = -\frac{I_{SC}R_a}{K_{Sp}}$ (5.20)

It can be seen that no-voltage motor rotational speed is a negative value and corresponds to the maximum torque produced by the motor and is usually mentioned to as, the "motor plugging" (Appelbaum J, 1979).

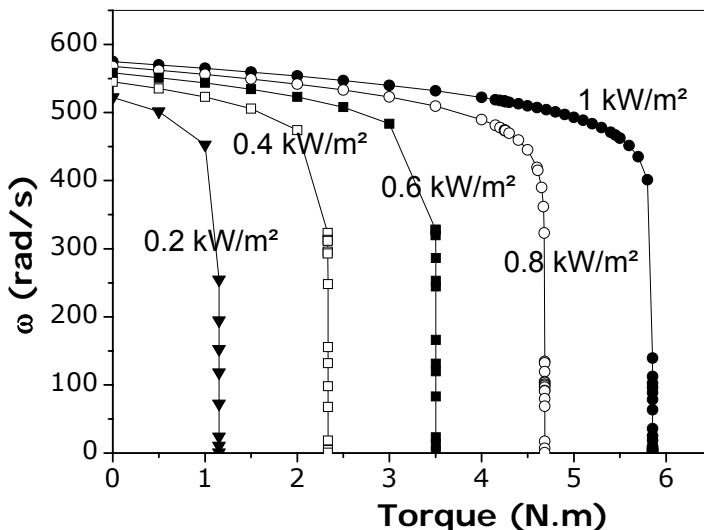


Figure 5.2 Motor rotational speed-torque characteristics $R_a=2.8 \Omega$ for different values of irradiance (simulated).

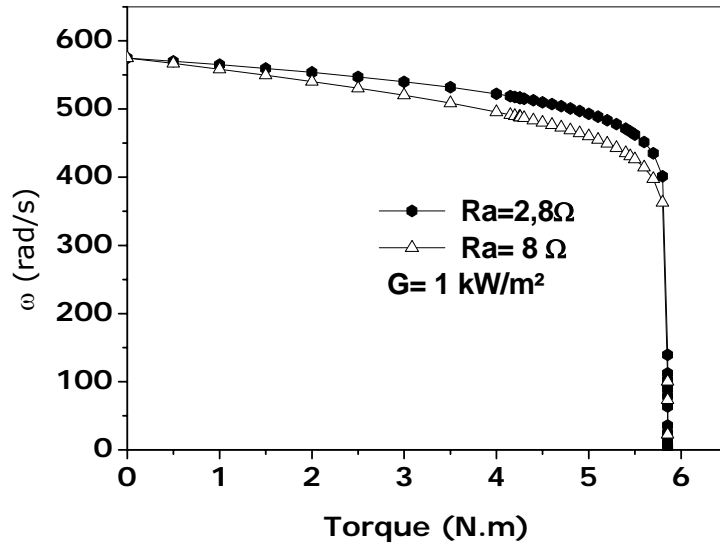


Figure 5.3 Motor speed-torque characteristics for two different values of armature resistance (simulated).

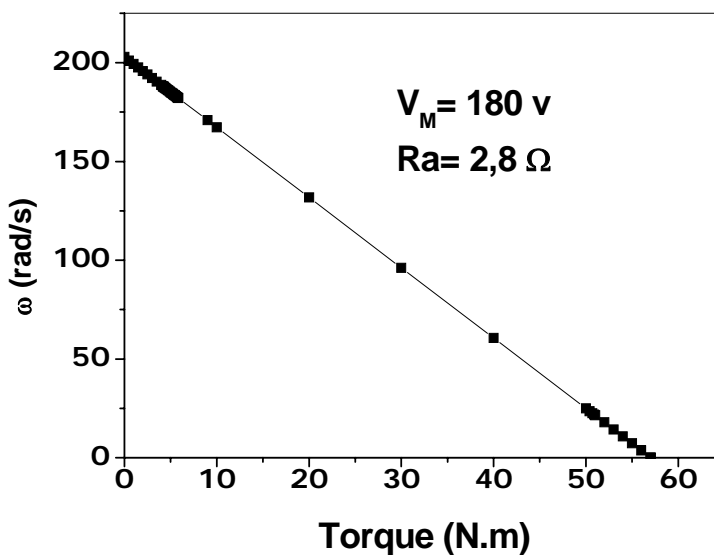


Figure 5.4 Motor speed-torque characteristics for constant voltage source (simulated).

In figure 5.2 rotational speed-torque characteristics for five solar irradiance levels are drawn for the DC motor and PV array (used in this work) characteristics. For the same motor and PV array characteristics, but with an increased armature resistance (8Ω), motor speed-torque

characteristic for two different values of armature resistance and for a solar irradiance of 1 kW/m^2 are shown in figure 5.3.

For comparison a speed-torque constant voltage supply (180 V) characteristic is drawn in figure 5.4. It has to be mentioned that 180 V is the nominal voltage of the DC motor used in this work. Figures were drawn by using equations describing the motor operation namely equations 5.12 and 5.16. It can be noticed from these equations that as the armature resistance increases for a particular solar irradiance level or a fixed voltage value, the starting torque decreases, equation (5.12). In figure (5.3) intercepts of speed-torque characteristics with axis, denoting the no-load speed and the stall torque, are hardly observed for 8Ω value of R_a , higher values would have been meaningless for the motor rating. Figure (5.3) shows also that armature resistance increase has an effect on the motor speed-torque characteristic for a particular solar irradiance, by squeezing it.

5.4.1 Optimum load matching in direct coupled PV systems

In a direct coupled system the PV array output power passes directly to the load. A battery storage may be employed to supply the load during short periods of time. The position of the load line relative to the maximum power line is a straightforward indication of the quality of matching of the system's components. Figure 5.5 is a simulation result graph of load matching components used in this work. The load considered here is a centrifugal pump. Power output of the array at 1 kW/m^2 solar irradiance value is shown in figure 5.6. The maximum power point for any particular solar irradiance level is situated at the top of the power curve. Connecting together the maximum power points, gives what is called the maximum power line. A matching factor defined as the ratio of the load energy to the array maximum energy output in a one day

period, is used as a measure for the quality of load matching (Kamel. YK, 1990). An efficient system is not only a system where the load curve coincides with the maximum power line, but it is also a system where the motor would start at the lowest possible irradiance level.

The process of matching would necessitate to bring together the load curve, initially in the mechanical plan (ω, T_M), and the PV array curves, initially the electrical plan (I, V), in one plan. (Appelbaum. J, 1981) proposed to achieve this by a combined graphical and analytical method. This method however, supposes that the photovoltaic array configuration (number of panels in series and in parallel) has been fixed before and consequently does not make it possible to determine the optimum array configuration except by repeated trial, which in some extent, correspond to our case. (Roger. JA, 1979) methods' makes it possible to draw the load curve independently of the PV array characteristics. In fact it was the PV array I-V curves that were fitted to the load curve. Figures (5.5) and (5.7) were drawn by using latter method. For each value of the rotational speed, the load torque T_L is determined by the nature of the load (in our case a centrifugal pump, where the torque is an increasing function of the rotational speed) and is equal to the motor torque equation (5.10), then V_M is obtained from equation (5.8).

A good matching could be then achieved only if the following conditions were verified (Roger. JA, 1979):

Firstly, the load curve must be as vertical as possible. Secondly, the load curve must be located in the region limited by the vertical dashed lines figure (5.6).

From the first condition it can be concluded that dV_M/dI_a must be as small as possible for all values of rotational speed, therefore from equation (5.8),

$$\frac{dV_M}{dI_a} = R_a + K_{Sp} \left(\frac{d\omega}{dI_a} \right) = R_a + K_{Sp} \left(\frac{d\omega}{dT_M} \right) \cdot \left(\frac{dT_M}{dI_a} \right) \quad (5.21)$$

From equation (5.10) we have:

$$\frac{dT_M}{dI_a} = K_{Tp} \quad (5.22)$$

Combining equations (5.21) and (5.22) we can get the following:

$$\frac{dV_M}{dI_a} = R_a + K_{Sp} K_{Tp} \left(\frac{1}{dT_L/d\omega} \right) \quad (5.23)$$

Therefore, to satisfy the first condition $dT_L/d\omega$ must be as large as possible. The second condition means that the load torque has to increase very slowly at low rotational speeds, and start increasing rapidly at high rotational speeds, so that the load curve could be situated in the region mentioned in the second condition. An ideal load torque-rotational speed curve is then characterized by the following points:

- Low value of starting torque
- $dT_L/d\omega$ low at low rotational speed values
- $dT_L/d\omega$ high at high rotational speed values

A much better judgment of the quality of the matching of the load line to the maximum power line can be seen from figure (5.5). There, the maximum power line of the PV array constituted from 15X15 series parallel Kyocera modules, and a motor-pump load line. Load line with a motor armature resistance $R_a=2.4, 4$ and 8Ω are plotted in figure (5.7), where it can be seen that as the motor armature resistance increases, the load line moves towards the maximum power region for low values of solar irradiance.

The quality of matching the load to the photovoltaic array may be visually estimated from the graphs drawn in figures 5.5 and 5.7. It may also be valued from the calculated utilization ratio for five specific solar irradiance levels, the results are summarized in table 5.1. It has to be mentioned that all figures and calculated matching factor values are the results of the first test of the sub-system model, and the simulation results were used to make the preliminary model adjustments.

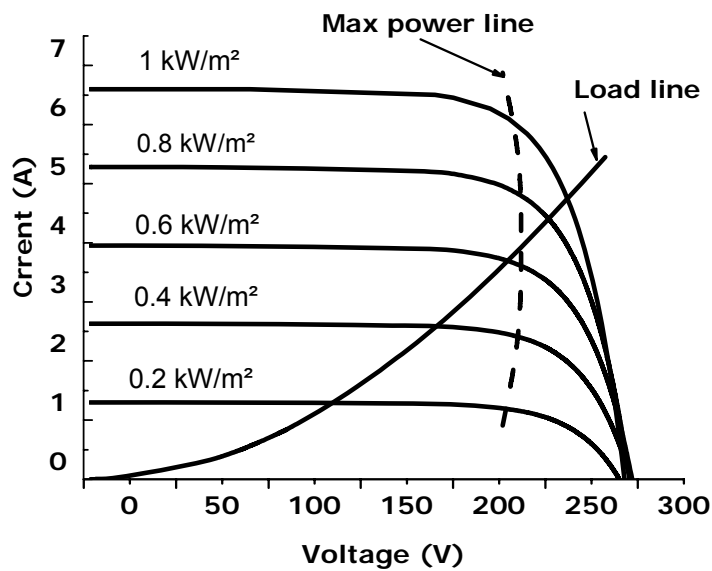


Figure 5.5 Electrical plan showing relative position of load line to the maximum power line, $R_a=2.4$ (simulation).

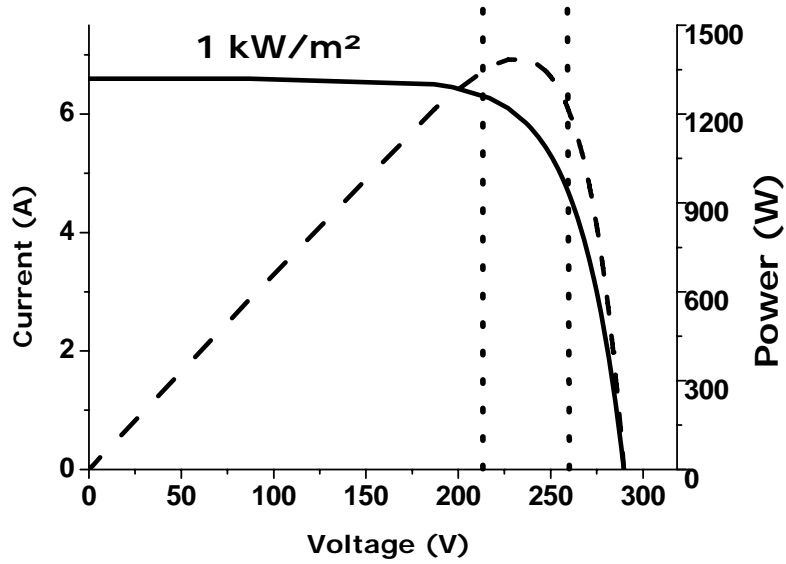


Figure 5.6 I-V characteristic of Kyocera module, locus of maximum power region is represented by the vertical dashed lines (simulation)

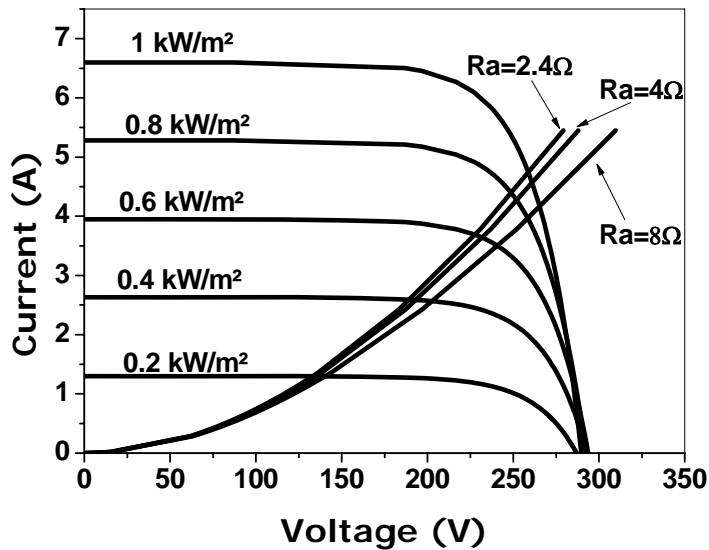


Figure 5.7 I-V characteristics and load curves for three values of motor armature resistance (simulation)

Solar (kW/m ²)	Ra=2.4 Ω			Ra=4 Ω			Ra=8 Ω		
	P _{in} (W)	P _{max} (W)	η (%)	P _{in} (W)	P _{max} (W)	η (%)	P _{in} (W)	P _{max} (W)	η (%)
0.2 kW/m ²	167.10	269.86	0.61	172.66	269.86	0.63	179.99	269.86	0.66
0.4 kW/m ²	490.50	560.90	0.87	507.18	560.90	0.90	525.66	560.90	0.93
0.6 kW/m ²	835.78	851.58	0.98	845.28	851.58	0.99	844.70	851.58	0.99
0.8 kW/m ²	1088.68	1122.43	0.96	1085.32	1122.43	0.96	1036.00	1122.43	0.92
1 kW/m ²	1224.05	1384.51	0.88	1184.81	1384.51	0.85	1103.01	1384.51	0.79

Table 5.1 Utilization factor $\eta = P_{in}/P_{max}$

CHAPTER 6.0

CENTRIFUGAL PUMP PERFORMANCE MODELING

6.1 Introduction

The purpose of this chapter is to describe the theoretical foundation of energy conversion in a centrifugal pump. Pressure head generated by the pump is expressed as a function of flow rate or capacity. Euler's equation for an ideally designed pump is used, and then correction factors are introduced to real head developed by the pump.

The torque required to pump a certain quantity of water is developed from the moment of momentum equation and presented as a function of rotational speed of the pump shaft and the pump impeller dimensions. This procedure presents the advantage to be applicable to any centrifugal pump provided that the impeller dimensions are known. Impeller dimensions are seldom given by the constructor, the pump should be dismantled for that purpose then. Also the principle of obtaining the operating point of the pump is given.

The hydraulic losses in the suction and delivery pipes are modeled by the Darcy equation and the total head against which the pump has to work is considered to be made up from these hydraulic losses and the static head.

6.2 Pump characteristic

6.2.1 Total head produced by the pump

A centrifugal pump comprises one or more impellers with vanes or blades, figures 6.1 and 6.2. The impeller rotates in an enclosure. The pump shaft

on which the impeller is mounted is driven by an electric motor (in this study the motor is a DC permanent magnet motor). When the blades rotate they produce an impulse on the fluid mass and set it into motion. The rotating blades cause a decreased pressure in the eye of the impeller and an increased pressure on the fluid at the edge of the blades. This is mainly due to the curvature of the blades and the increase of the peripheral velocity.

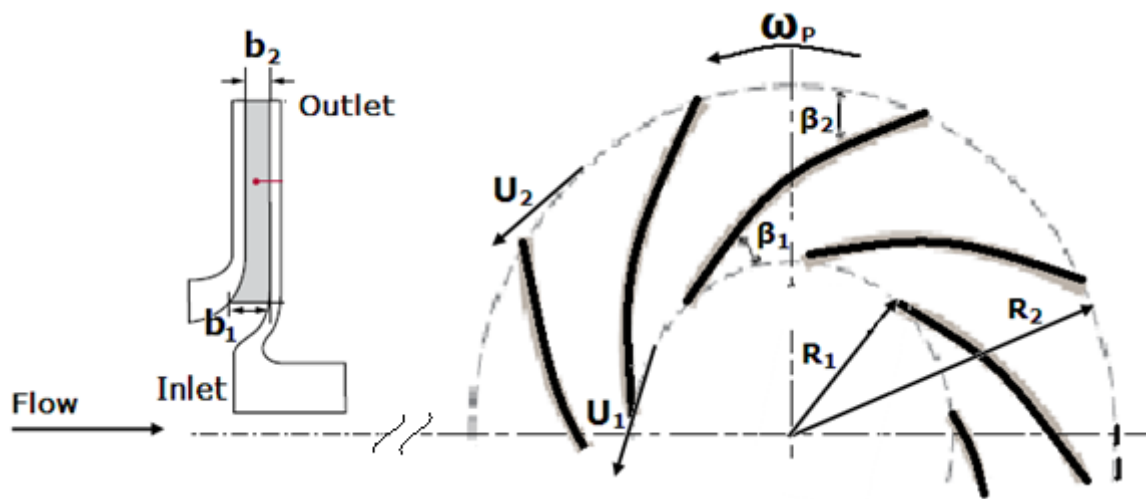


Figure 6.1 A centrifugal pump radial impeller (adopted from Grundfos technical sheet).

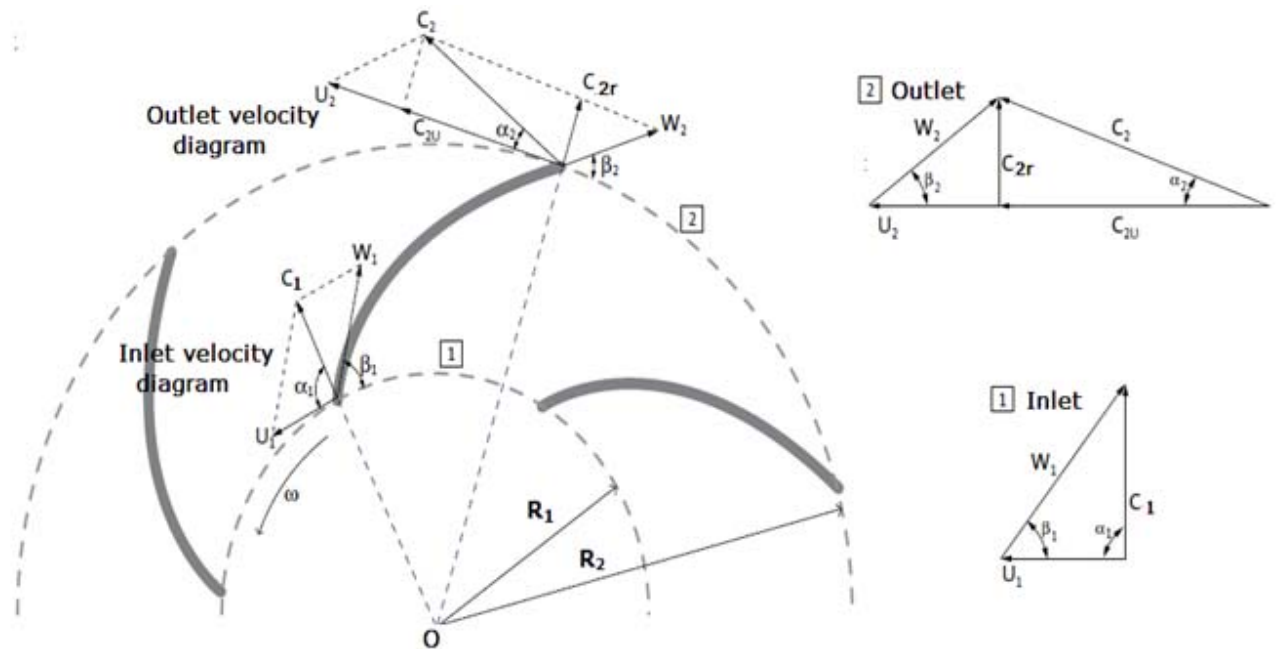


Figure 6.2 Velocity triangles positioned at the impeller inlet and outlet (adopted from Grundfos technical sheet).

6.2.1.1 Velocities triangles

If we consider a fluid flowing through a rotating impeller, there are three types of velocities (Kovats. A, 1964), these velocities are: (see figures 6.1 and 6.2)

- a- U is the velocity of a point on the impeller relative to the ground.
- b- C is the absolute velocity of a fluid particle flowing through the impeller relative to the ground.
- c- W is the velocity of fluid particle relative to the impeller.

It is important at this stage to investigate the flow inside the pump impeller and the relationship between the different velocities. We assume, as it is always the case in pump theory, that the flow is two dimensional, and we suppose also that the fluid follows the impeller blades exactly. These assumptions are aimed to simplify the problem. In reality the velocity distribution is very complex and dependent upon the number of blades, their shapes and thicknesses, as well as on the width of the impeller and its variation with radius. Also the real flow through an impeller is three dimensional.

From the velocities triangle (figure 6.2), the angles α and β are defined as the angle between C and U , and the angle between W and U respectively. The angle β is in fact the angle made by a tangent to the impeller blade and a line in the direction of motion of the blade. Figure 6.2 shows these angles at the inlet and outlet of the impeller. C_r is the radial (or normal) component of the absolute velocity C and C_u is its tangential component (e.g. figure 6.3).

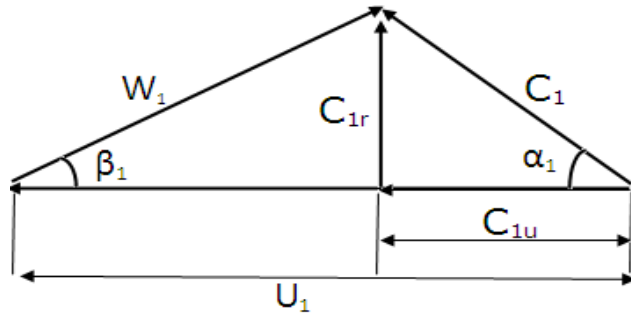


Figure 6.3 Velocities triangle at the impeller inlet.

6.2.1.2 Ideal head equation

Pump design is based on the “virtual head” equation, designated by $H_{vir,\infty}$, where the subscript ∞ signifies an infinite number of blades or perfect guidance of the fluid. $H_{vir,\infty}$ equation is based upon three assumptions (Church. AH, 1945):

- 1) The fluid is perfectly guided at the outlet.
- 2) The impeller passages are completely filled with actively flowing fluid at all times.
- 3) The fluid velocities are the same at similar points on all the lines.

The three assumptions represent an ideally designed pump. If turbulence and friction are neglected, the difference between the total energy of the fluid at the outlet and the total energy at the inlet will be the work put into the impeller. This is expressed as the “head of fluid” and equals, the total virtual head $H_{vir,\infty}$. The virtual head is made up of static energy (or pressure energy) and velocity energy, so that:

$$H_{vir,\infty} = \frac{U_2^2 - U_1^2 + W_1^2 - W_2^2 + C_2^2 - C_1^2}{2g} \quad (6.1)$$

And

$$H_{vir,\infty} = \left(\frac{U_2^2 - U_1^2}{2g} \right) + \left(\frac{W_1^2 - W_2^2}{2g} \right) + \left(\frac{C_2^2 - C_1^2}{2g} \right) \quad (6.2)$$

In the above expression, the first term denotes the energy used in setting the fluid into a circular motion about the impeller axis. The second term is the regain of static head due to reduction of relative velocity in the fluid passing through the impeller. The third term represents the increase of the kinetic energy of the fluid in the impeller.

From velocity triangles of figure 6.3, we have

$$\begin{aligned} W_1^2 &= U_1^2 + C_1^2 - 2U_1 C_1 \cos\alpha_1 \\ W_2^2 &= U_2^2 + C_2^2 - 2U_2 C_2 \cos\alpha_2 \\ C_{1u} &= C_1 \cos\alpha_1 \\ C_{2u} &= C_2 \cos\alpha_2 \end{aligned} \quad (6.3)$$

Substituting into (6.1),

$$H_{vir,\infty} = \frac{U_2 C_2 \cos\alpha_2 - U_1 C_1 \cos\alpha_1}{g} = \frac{U_2 C_{2u} - U_1 C_{1u}}{g} \quad (6.4)$$

Relation (6.2.1.2.4) is also known as Euler's equation.

6.2.1.3 Actual head equation

Applying Euler's equation to centrifugal pumps, the usual assumption is that the fluid enters the impeller blades radially, therefore

$$C_1 = C_{1r} \text{ and } C_{1u} = 0,$$

Hence, $\alpha_1 = 90^\circ$. And relation (6.4) is reduced to,

$$H_{vir,\infty} = \frac{U_2 C_{2u}}{g} \quad (6.5)$$

The major assumption underlying the considerations of the previous sections was of an infinite number of blades in the impeller. In practice, of course, the number of blades is finite and their spacing depends on a

particular impeller design and, therefore, may vary considerably. The influence of the final number of impeller blades (z) on the flow velocity of the fluid is taken into account by the introduction of the Pfleiderer correction factor, P_p (Braunstein. A, Kornfeld. A, 1981),

$$P_p = \frac{(1.2)}{(z)} \frac{1 + \sin\beta_2}{[1 - \left(\frac{D_1}{D_2}\right)^2]} \quad (6.6)$$

According to Pfleiderer the relation between the virtual head for an infinite number of blades and the theoretical head is:

$$H_{vir,\infty} = H_{vir}(1 + P_p) \quad (6.7)$$

Detailed explanations could be found in (Kovats. A, Desmur. G, 1958) or (Kovats. A, 1964).

So the pump water head correction is defined as:

$$\epsilon_p = \frac{1}{1 + P_p} \quad (6.8)$$

And the virtual head with a finite number of blades could be written as follows:

$$H_{vir} = \epsilon_p H_{vir,\infty} \quad (6.9)$$

Since $U = R\omega_p$, it follows that the tangential blade velocities at inlet and outlet are given by:

$$U_1 = R_1 \omega_p$$

$$U_2 = R_2 \omega_p \quad (6.10)$$

The flow at outlet is through cylindrical surface and the velocity component normal to it is C_{2r} , the flow rate delivered at the outlet for infinitely thin blades is given by:

$$Q = C_{2r} 2\pi b_2 R_2 \quad (6.11)$$

From the velocity triangle at the outlet we have:

$$C_{2u} = U_2 - \frac{C_{2r}}{\tan \beta_2} \quad (6.12)$$

By substituting (6.5), (6.11), (6.12) and $U_2 = R_2 \omega_p$ into (6.9) we obtain:

$$H_{vir} = \epsilon_p \frac{1}{g} [(R_2 \omega_p)^2 - \frac{Q \omega_p}{2\pi b_2 \tan \beta_2}] \quad (6.13)$$

This relation represents the virtual head delivered by the pump in a convenient way, since it gives the head as a function of the pump dimensions and, therefore could be applied to any centrifugal pump.

The actual head developed by the pump, denoted by H , is in fact less than the virtual head. This is caused by friction and turbulence losses inside the pump impeller, which give rise to the hydraulic efficiency, defined as the ratio of the actual head to the virtual head for finite number of blades.

$$\eta_h = \frac{H}{H_{vir}} \quad (6.14)$$

Thus, the actual head developed by the pump may be written as

$$H = \eta_h H_{vir} = \eta_h \epsilon_p H_{vir,\infty} \quad (6.15)$$

The actual head developed by the pump is then:

$$H = \eta_h \epsilon_p \frac{1}{g} [(R_2 \omega_p)^2 - \frac{Q \omega_p}{2\pi b_2 \tan \beta_2}] \quad (6.16)$$

6.2.2 Pump torque

What is meant by pump torque is the torque required for pumping a certain quantity of water. Conservation of momentum law, called also Euler equation, is used to describe the torque at the pump shaft.

The particles of a fluid stream will possess momentum, and, whenever the velocity of the stream is changed in magnitude or direction, there will be a corresponding change in the momentum of fluid particles. In accordance with Newton's law, a force is required to produce this change. For small masses moving to a Cartesian ($x; y; z$) coordinate system, Newton's equation is:

$$dF = \frac{\partial}{\partial t} (dmv) \quad (6.17)$$

And the torque on the mass is:

$$rdF = r \frac{\partial}{\partial t} (dmv) \quad (6.18)$$

This torque is denoted as dM_p . The right hand side of the above expression could be written in the form $\frac{\partial}{\partial t} (r \cdot dm v)$, and the moment of momentum dM_p is expressed as:

$$dM_p = \frac{\partial}{\partial t} (r \cdot dm v) \quad (6.19)$$

The torque for a finite system is obtained by integrating the above equation (Shames. H.I, 1962).

$$M_p = \frac{\partial}{\partial t} \iiint (r \cdot v) \rho ds \quad (6.20)$$

Where ds is a volume element.

The solution of equation (6.20) gives the expression for the torque developed by the impeller.

$$M_P = \rho Q (R_2 C_{2u} - R_1 C_{1u}) \quad (6.21)$$

The product ρQ is the rate of change of momentum with respect to time (a force). The tangential component of this force is QC_u , at inlet we have ρQC_{1u} which represents the force exerted by the water on the impeller at the entrance. Whereas ρQC_{2u} is a force exerted by the impeller on the water. The net torque exerted by the impeller on water is represented by expression (6.21).

From the velocities triangles at the impeller inlet and outlet we have

$$C_{2u} = U_2 - \frac{C_{2r}}{\tan\beta_2} \text{ at impeller outlet}$$

$$\text{And } C_{1u} = U_1 - \frac{C_{1r}}{\tan\beta_1} \text{ at impeller inlet} \quad (6.22)$$

Hence, the pump torque could be rewritten as follows:

$$M_P = \rho Q [R_2 \left(R_2 \omega_p - \frac{C_{2r}}{\tan\beta_2} \right) - R_1 \left(R_1 \omega_p - \frac{C_{1r}}{\tan\beta_1} \right)] \quad (6.23)$$

The continuity equation applied to inlet and outlet for incompressible flow for infinity thin blades gives (Douglas. JF, Gasiorek. JM, Swaffield. JA, 1985):

$$Q = 2\pi R_1 b_1 C_{1r} = 2\pi R_2 b_2 C_{2r} \quad (6.24)$$

Replacing C_{2r} from the equation above into equation (6.23) we have:

$$M_P = \rho Q [R_2 \left(R_2 \omega_p - \frac{R_1 b_1 C_{1r}}{R_2 b_2 \tan\beta_2} \right) - R_1 \left(R_1 \omega_p - \frac{C_{1r}}{\tan\beta_1} \right)] \quad (6.25)$$

It was supposed earlier as it is very often done, that water enters the impeller radially so that $\alpha_1=90^\circ$ and $C_{1r} = U_1 \tan\beta_1$. Therefore by replacing C_{1r} by its value and substituting the flow rate Q from equation

(6.24) into equation (6.25), the pump torque maybe rewritten as follows:

$$M_p = \rho 2\pi R_1 b_1 R_1 \omega_p \tan\beta_1 [R_2 \left(R_2 \omega_p - \frac{R_1 b_1 R_1 \omega_p \tan\beta_1}{R_2 b_2 \tan\beta_2} \right) - R_1 \left(R_1 \omega_p - \frac{R_1 \omega_p \tan\beta_1}{\tan\beta_1} \right)]$$

Or in a much more simplified form:

$$M_p = \rho 2\pi R_1^2 b_1 \omega_p^2 \tan\beta_1 \left(R_2^2 - \frac{R_1^2 b_1 \tan\beta_1}{b_2 \tan\beta_2} \right) \quad (6.26)$$

From the above equation it can be seen that the pump torque is proportional to the square of the rotational speed of the pump shaft.

A constant denoted by K_m , function of the impeller dimensions is defined, so that the torque could be expressed in the following simple form:

$$M_p = K_m \omega_p^2 \quad (6.27)$$

Hence, the expression of K_m is:

$$K_m = \rho 2\pi R_1^2 b_1 \tan\beta_1 \left(R_2^2 - \frac{R_1^2 b_1 \tan\beta_1}{b_2 \tan\beta_2} \right) \quad (6.28)$$

6.3 Hydraulic system head and operating Point

A centrifugal pump will operate on its $H=f(Q)$ characteristic where the generated head, at a given rotational speed, just matches the head required to overcome the sum of the static lift and frictional resistance in the pipes to which it is connected, as shown in figure 6.4. A change in the static head H_{st} will result in a new system curve parallel to the original one. The losses within the piping circuit are mainly due to friction and turbulence occurring in the pipes which include the suction and the

delivery piping. Turbulence losses are very difficult to evaluate so they are included with the friction losses. The latter are approximated by the Darcy equation (Douglas. JF, Gasiorek. JM, Swaffield. JA, 1985).

$$h_f = \frac{4k_f l v^2}{d^2 g} \quad (6.29)$$

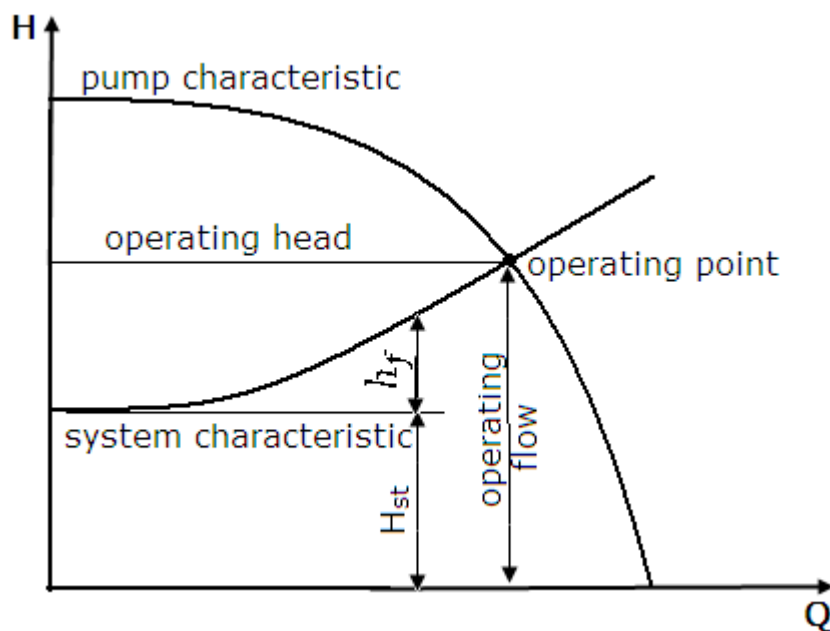


Figure 6.4 Pump and system characteristics

k_f is an empirical factor describing the friction loss, l is the length of the pipes including suction and delivery pipes, d is the diameter of pipes and v is the velocity of water in the pipes. In the case where suction pipe diameter is different from the delivery pipe diameter, the Darcy equation should be applied separately to suction and delivery pipe, and the total friction losses are calculated by adding the friction losses for both suction and delivery line.

At this point it may be useful to note that the value of friction factor quoted in many texts (especially American) is $4k_f$ in the notation

employed in this work. Knowing that $Q=v \pi d^2/4$. The Darcy equation could be expressed in the following form;

$$h_f = 4k_f \frac{8lQ^2}{d^5\pi^2g} \quad (6.30)$$

Expression (6.30) is a convenient way to representing the friction losses in the pipes, since the pump head is also expressed as function of the flow rate Q .

To the friction losses we should add losses in pipe fittings, bends and at pipe entry. Losses in pipe fitting are usually expressed in the following form (Douglas. JF, Gasiorek. JM, Swaffield. JA, 1985):

$$h = k \frac{v^2}{2g} \quad (6.31)$$

Where k is the fitting loss coefficient, It is a non-dimensional constant and its value is obtained experimentally.

Table 6.1 Head loss coefficients for a range of pipe fittings (Douglas. JF, Gasiorek. JM, Swaffield. JA, 1985)

Fitting	Loss coefficient, k
Pump foot valve	1.5
Return bend	2.2
90° elbow	0.9
45° elbow	0.4
Large radius 90° bends	0.6
Tee junction	1.8
Sharp pipe entry	0.5
Curved pipe entry	→ 0.0
Sharp pipe exit	0.5

The total head loss is then the sum of the friction head loss and the separation losses at changes of section, bend and fittings.

The system head, or as it is commonly called the system resistance, is the head loss in the pipeline due to flow rate Q . Thus, in order to maintain this flow rate, energy must be supplied to the pipe system. This energy is supplied by the pump. The pump will provide energy equal to the difference in levels (static head, H_{st}). At operating point then, we will have:

$$H = H_{st} + h_f \quad (6.32)$$

Where H is the head developed by the pump expression (5.2.1.2.15) which, if substituted in equation (6.32) will give:

$$H_{st} + h_f = \eta_h \epsilon_p \frac{1}{g} \left[(R_2 \omega_p)^2 - \frac{Q \omega_p}{2\pi b_2 \tan \beta_2} \right] \quad (6.33)$$

Where h_f is given by (6.30). For a particular pump rotational speed and for a known friction factor, equation (6.33) may be written in the following general quadratic equation form:

$$aQ^2 + bQ + C = 0 \quad (6.34)$$

Solutions of (6.34) are:

$$Q_{1,2} = \frac{-b \pm \sqrt{b^2 - 4ac}}{2a}, \quad a = 4k_f \frac{8lQ^2}{d^5 \pi^2 g} + \frac{8k}{\pi^2 d^4 g}$$

$$b = \frac{\eta_h \epsilon_p \omega_p}{2\pi b_2 \tan \beta_2 g}, \text{ and } c = H_{st} - \eta_h \epsilon_p \frac{R_2^2}{g} \omega_p^2 \quad (6.35)$$

From the relations (6.35) one can notice that a and b are both positive values and cannot be negative. Therefore one of the solutions of equation (6.34) is negative. A negative flow rate is meaningless in this case. The solution and the only solution of equation (6.34) is:

$$Q = \frac{-b + \sqrt{b^2 - 4ac}}{2a} \quad (6.36)$$

It should be noted that the value of the friction factor k_f must be selected so that the correct value of h_f will always be given by the Darcy equation, and so cannot be single-value constant. In fact, the friction factor k_f depends on several parameters namely, Reynolds number, pipe wall roughness size, spacing of the roughness particles and on the shape of the roughness particles. Thus, the calculation of friction factor is dependent on the use of empirical results, and the most common reference source is the Moody chart, which is a logarithmic plot of k_f versus Reynolds number for a range of relative roughness values (figure 6.5). The Moody chart, however, is not suitable for computer simulation programs but, it has been drawn using other equations. For laminar flow ($R_e < 2320$), the friction factor depends only on Re and is calculated from the Poiseuille equation:

$$k_f = 16/R_e$$

(6.37)

For relative roughness values less than 0.001, in turbulent flow, the curve approaches the Blasius smooth pipe curve, and for pipes having high values of relative roughness, the friction factor is constant. One way of calculating the friction factor for turbulent flow is to use the Colebrook-White equation is an iterative equation which expresses the relationship between k_f , R_e and the relative roughness k_p/d .

$$1/\sqrt{k_f} = -4 \log_{10} \left(\frac{10^{-3} k_p}{3.71 d} + \frac{1.26}{R_e \sqrt{k_f}} \right)$$

(6.38)

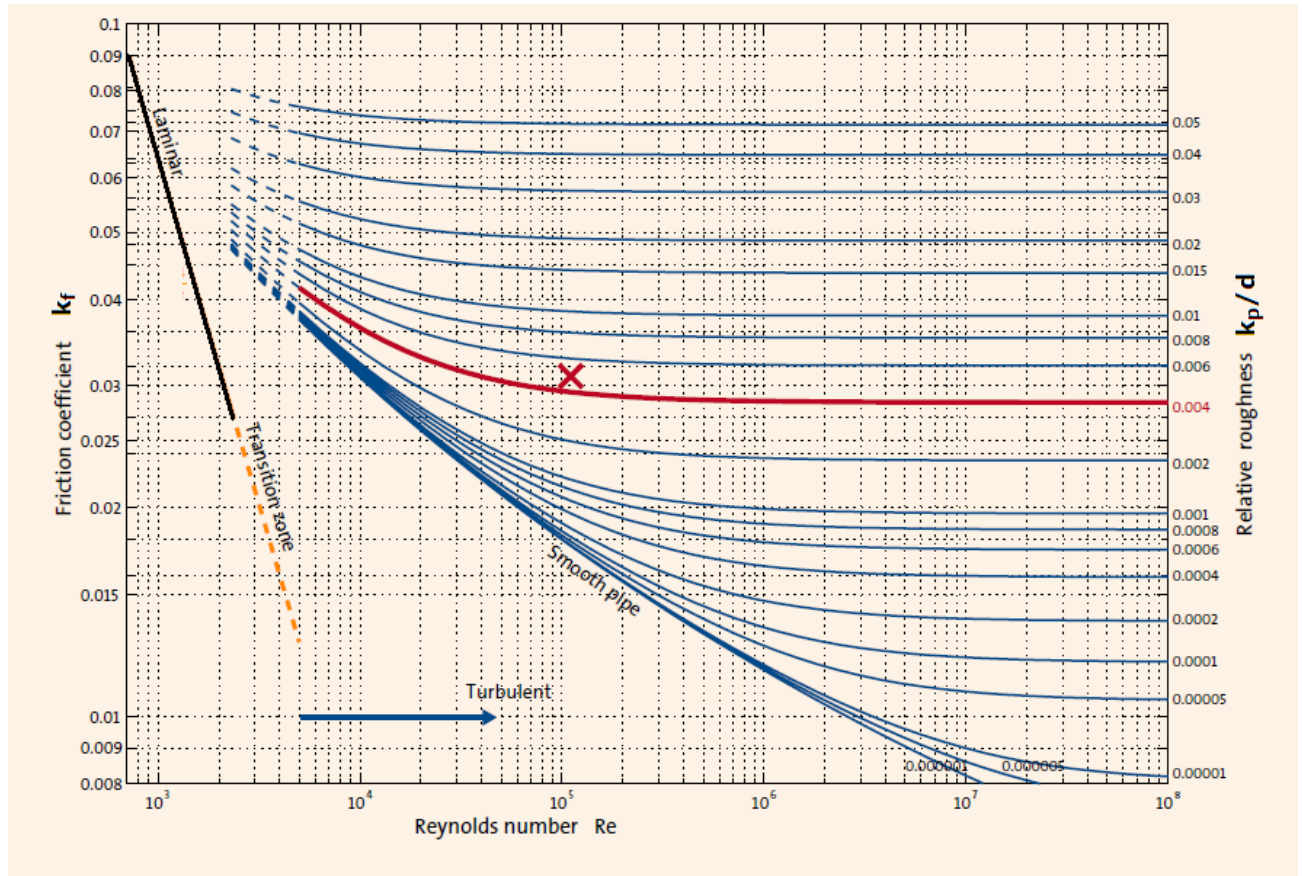


Figure 6.5 Moody chart showing friction factor k_f as function of Reynold's number and surface roughness for laminar and turbulent flows (adopted from Grundfos technical sheet).

CHAPTER 7.0

PV PUMPING SYSTEM FINAL MODEL AND EXPERIMENTAL TESTING

7.1 Introduction

We here describe the PV water pumping system performance prediction method based on system and site characteristics. The method can be described as composed of two parts, first, the solar data on the PV panel are processed and clustered so to enclose different types of climate conditions over a whole year, and then these data are presented as input to the second part of the simulation model which calculates the system performance. Sets of equations describing the performance of each component of the system compose the model. These equations are then solved numerically giving way to a unique set of performance information such as pump head, flow rate, voltage and current for a particular solar irradiance level and array temperature. The model assumes steady state conditions for an hourly used time interval. All components of the system from the PV array to the hydraulic system are considered as fully autonomous elements with feed-in feed-out interconnections.

7.2 Methodology

The model simulates the performance on an hourly basis and can integrate results. A fixed day length of 14 hours is considered all over the model. The array operating temperature is calculated for every hour as a function of ambient conditions. The hydraulic system includes the suction and delivery pipes with foot-valve. The model takes into account the head losses in the pipes. Complete PV operating water pumping system test bench was installed and monitored for several periods of the year. The

system can be configured for two different static heads. The testing continued for several years by first using a fixed DC power supply unit, and then by direct connection to the PV array. All relevant operational parameters for the system, such as solar irradiance, ambient temperature, load current, load voltage, rotational speed, pressure at pump outlet and flow rate were collected over the test period.

When a pump is driven by a photovoltaic powered motor, and if the friction and moment of inertia are neglected, which means that there is no-loss speed transmission between the motor and the pump, three conditions are always verified. Firstly, the motor torque is always equal to the pump torque, which was defined in earlier chapters as the torque required to pump a certain quantity of water, in the case where the pump is coupled to the motor shaft via a pulley or a gear box, the motor torque is equal to the pump torque multiplied by the ratio pump rotational speed to motor rotational speed, this study considers only the first case. Secondly, the voltage across the motor armature is equal to the voltage supplied by the photovoltaic array, resistive losses in the electrical connections are neglected. Thirdly, the current flowing in the motor armature is the same as the current delivered by the photovoltaic array. By considering the first condition and from relations relating the motor torque and the pump torque mentioned in chapters 5 and 6, and stated here again.

$$T_M = K_{Tp} I_a$$

$$M_P = K_m \omega_p^2$$

We obtain:

$$K_{Tp} I_a = K_m \omega_p^2 \quad (7.1)$$

From the equation above we have:

$$\omega_p = \sqrt{\frac{K_{Tp} I_a}{K_m}} \quad (7.2)$$

The motor voltage equation was expressed in the following form:

$$V_M = R_a I_a + K_{Sp} \omega$$

Substituting equation 7.2 into the motor voltage equation above gives:

$$V_M = R_a I_a + K_{Sp} \sqrt{\frac{K_{Tp} I_a}{K_m}} \quad (7.3)$$

From second and third conditions equation 7.3 can be rewritten as:

$$V = R_a I + K_{Sp} \sqrt{\frac{K_{Tp} I}{K_m}} \quad (7.4)$$

Equation 7.4 is in fact the transformed load characteristic from the mechanical plane into the electrical plane.

It is obvious that the key to analysing the performance of direct coupled PV pumping system is the electrical plane, where the motor–pump current versus voltage characteristics or I–V load curve and PV array family of I–V curves are required. These curves are drawn in figure 7.1.

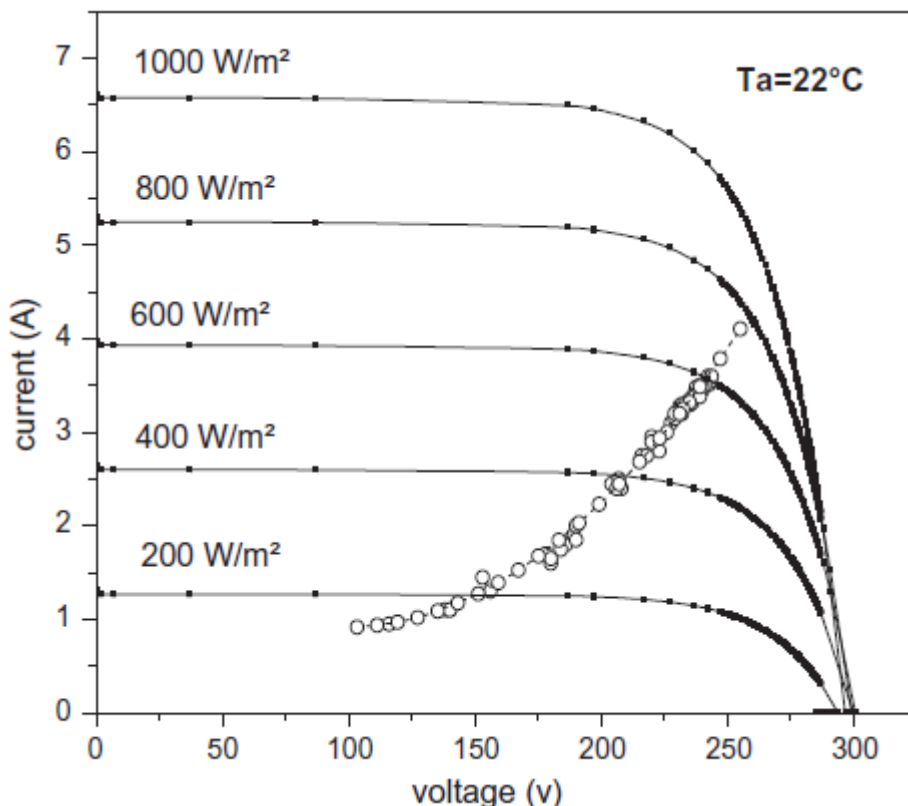


Figure 7.1 PV pumping system performance curves
(Mokeddem.A et al, 2011)

Since the photovoltaic array operates at a point on its characteristic given by the equations described in chapter 4, namely $V=f(I)_{G,T}$ where G and T are the irradiance level and the PV panel (array) temperature respectively.

Equation 7.4 can be solved numerically for I and the photovoltaic array voltage found from the equation describing the PV performance mentioned in chapter 4. The intercept between the I-V characteristics of the motor-pump and the PV array I-V characteristics fixes the operating point for steady state operation. The PV array characteristics for different irradiance level were drawn by using the model described in details in chapter 4. The combination of the solar irradiance, the photovoltaic array, the DC motor, the pump and the hydraulic system can be described as a non-linear negative feed-back system. The general block diagram is shown in figure 7.2. For every irradiance value and PV array temperature a chain reaction will occur according to the feed-back system.

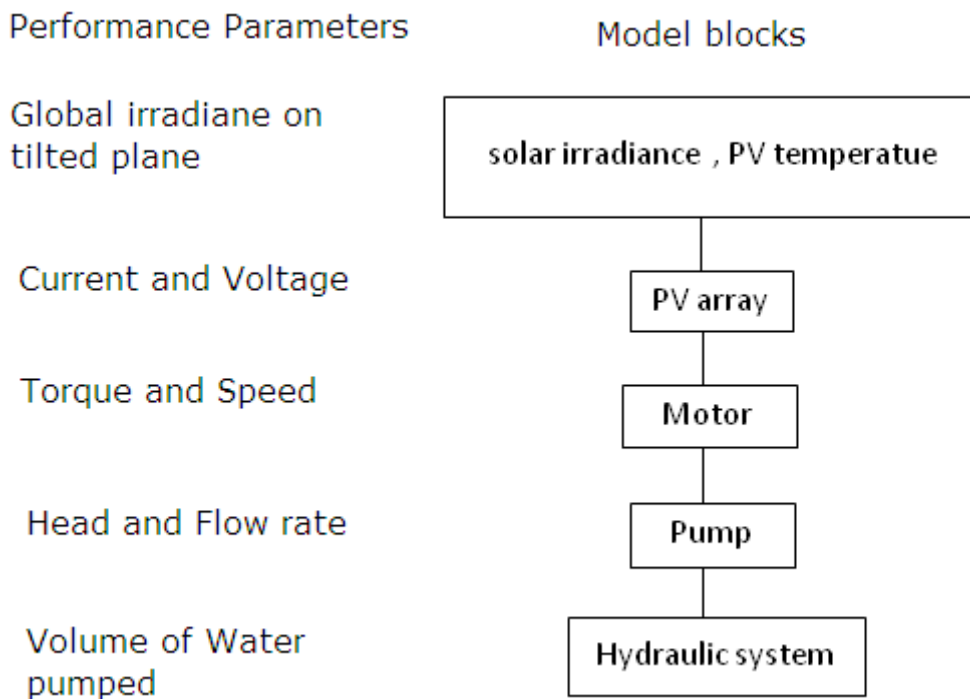


Figure 7.2 Photovoltaic pumping system model block diagram.

The photovoltaic pumping system analysed in this study by its performance ought to be defined through the characteristic specification of all its components, namely the motor characteristics, the pump impeller dimensions and the solar cell characteristics with the array configuration. It is very seldom that pump characteristics are available to user, in order

to overcome such difficulty we have had to dismantle (in all cases) the pump impeller and to acquire the relevant dimensions. The structural combination of different components of the photovoltaic pumping system is schematically represented in figure 7.3. It is obvious that, regarding the dynamic behavior of solar irradiance and the non linear nature of the analysis of the photovoltaic pumping system performance given earlier necessitate having recourse to computer simulation. Instead of developing a whole computer program to simulate the performance of the PV pumping system, which in our case was not an objective in its self, and also because of the fact that numerous professional simulation software are available on the net, we have had to simulate the performance of every system components independently by implementing equations which describe the components performance of every element of the system separately. I must admit that gathering each components data and feeding them to the next element of the system is rather exhausting, but in the same time can be full of inside data information.

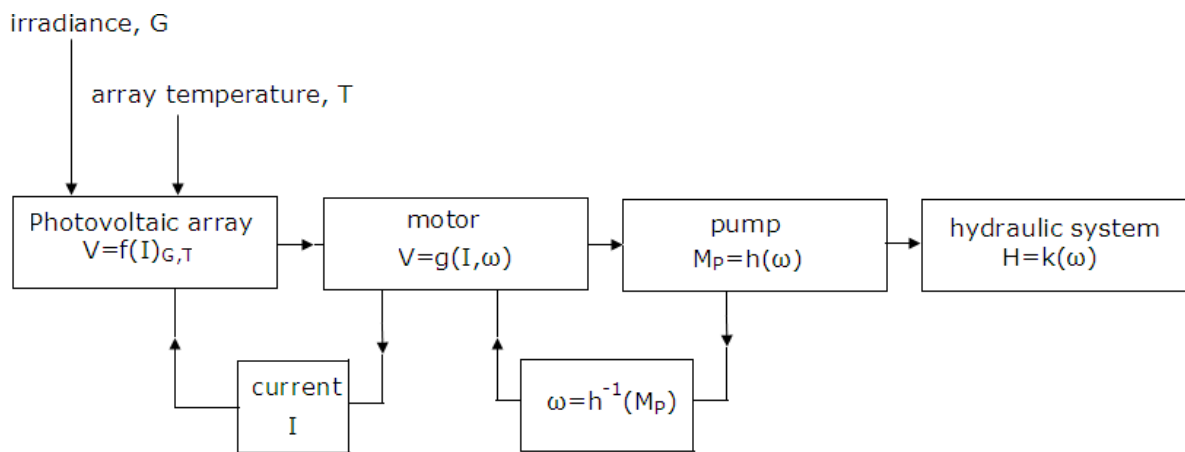


Figure 7.3 PV pumping system calculations structure.

Some of the early testing results are presented here. In figure 7.4 the sub-system (motor-pump) efficiency is presented for two static heads namely 0.6 m and 11m (low and high static head successively). It can be seen through the motor-pump efficiency figures that, the system as it is used is much more suited for low power pumping systems than high

power pumping systems. The maximum sub-system efficiency 26% agrees with the efficiency of most pumping systems that exist nowadays.

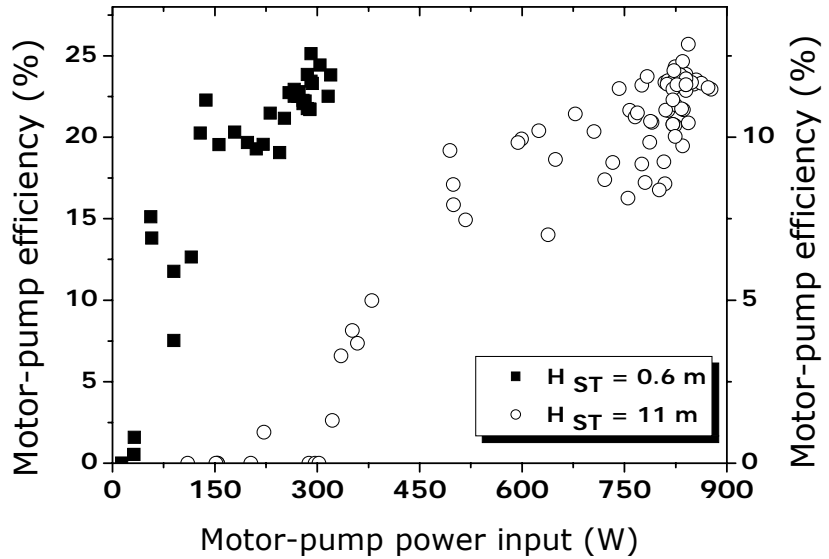


Figure 7.4 Sub-system efficiency for two static heads (recorded at USTO).

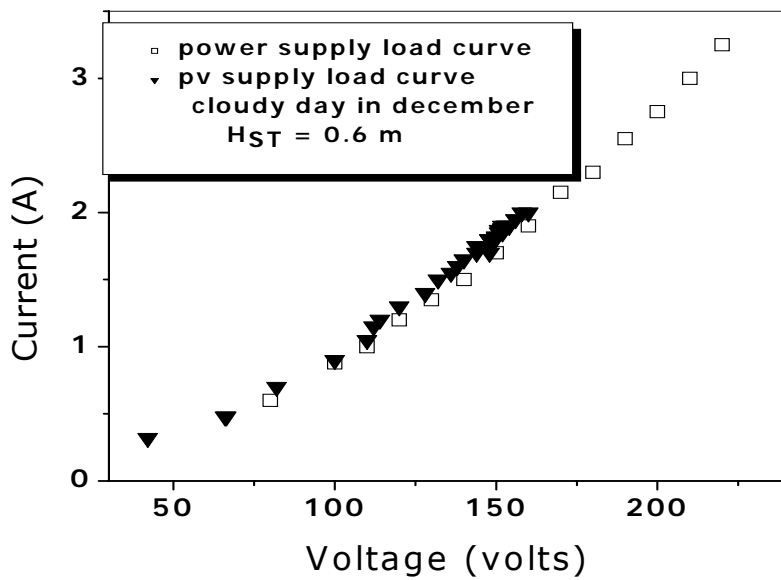


Figure 7.5 PV supply and fixed power supply performance comparison (recorded at USTO).

The figure 7.5 above shows the load curve recorded in the early stages of system testing via a fixed power source and the PV array for the low static

head. It shows that the PV array supplied load cannot go beyond a certain threshold at 0.6m of static head.

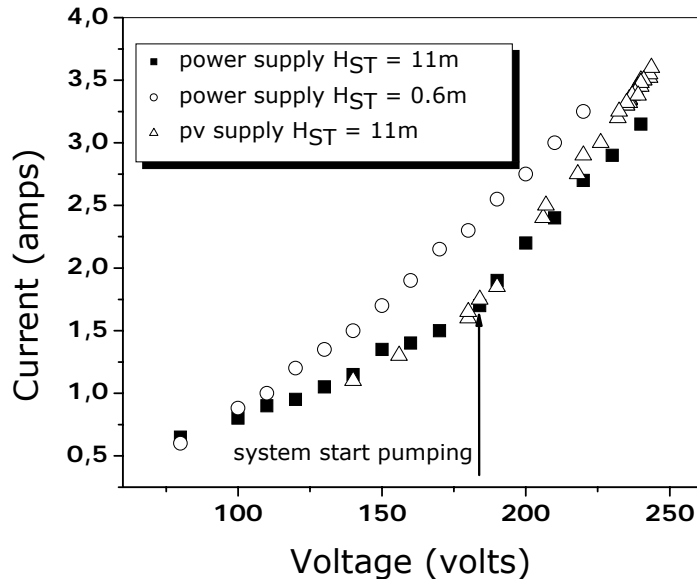


Figure 7.6 Load curve for two system configurations (recorded at USTO).

In figure 7.6 we can see how the power source load curve changes in form with the system configuration (static head). We can notice that the power source load curve at high static head is much flat than that of a low static head system configuration, it can also be seen that after the system start pumping the load curve is more steep.

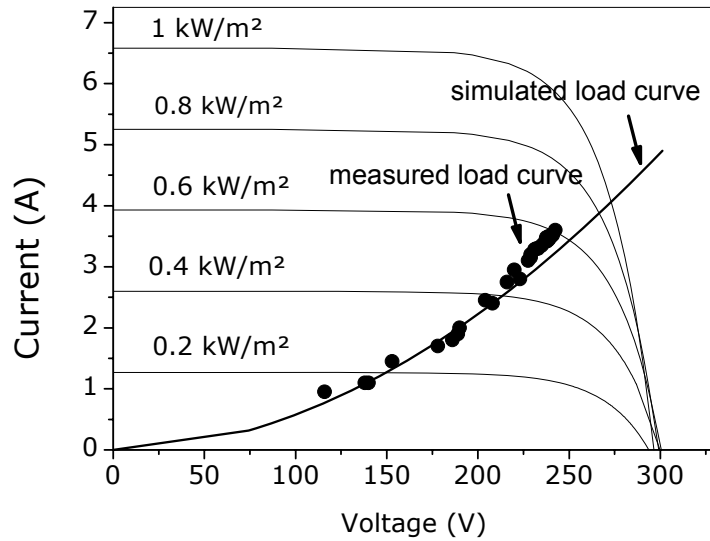


Figure 7.7 Predicted against measured load curve (recorded at USTO).

In figure 7.7 is plotted simulated and measured load curve as well as the I-V characteristics of the PV array for different solar irradiance values.

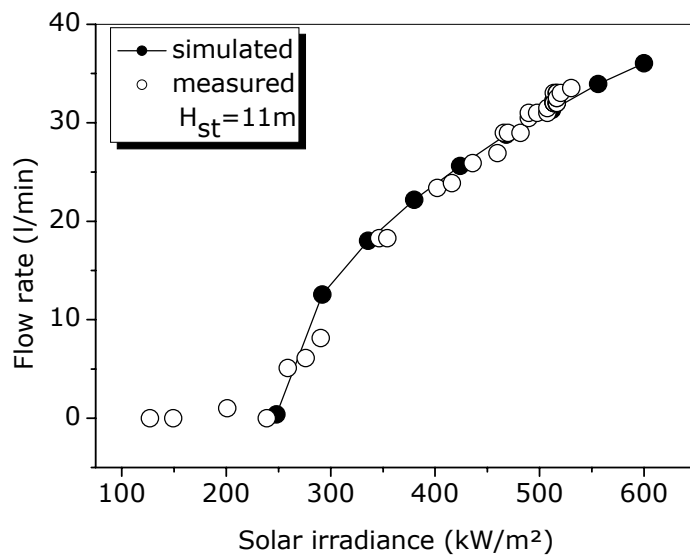


Figure 7.8 Predicted against measured flow rate values (recorded at USTO).

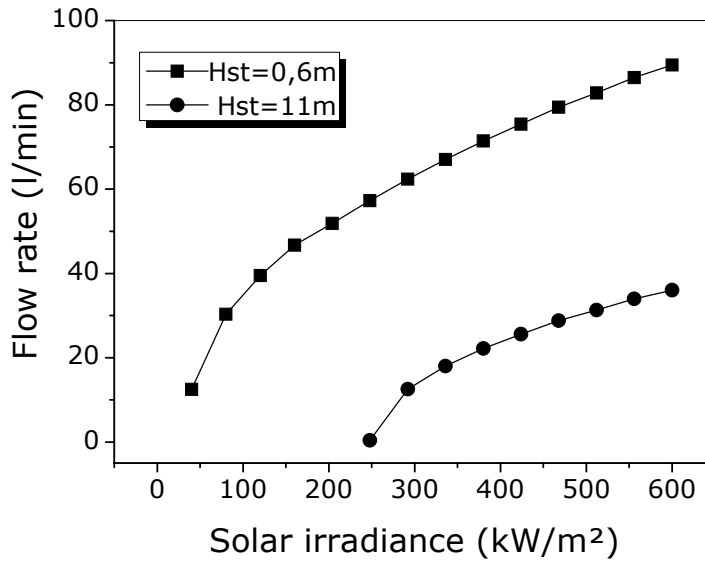


Figure 7.9 Predicted values of flow rate for two hydraulic system configurations (simulation).

Simulated values of flow rate as function of solar irradiance for two different hydraulic system configurations show a fairly good agreement with measured values (see figure 7.8). Predicted pumped water flow rate against irradiance values is plotted in figure 7.9 for static head values of 11m and 0,6m.

7.3 Components parameters measurements

Tests and experimental works described in this chapter are both indoor and outdoor testing, they were carried out at the University of Science and Technology of Oran at the department of Electronics. The testing procedure had to comply with the standard testing procedure described in numerous research studies (King. DL, 1996). PV panel calibration is a step of the procedure among others which provides a way of checking that the array output meets the manufacturer specifications, particularly when we know that the PV modules are over 15 years old. Series of measurements were made for the open circuit current and the open circuit voltage of the PV panel under clear sky conditions and different ambient temperatures.

Instruments used are voltmeter, ammeter, pyranometer (Kipp & Zonen CM11), and digital thermometer. A solar simulator would have been the best option for a comprehensive PV panel calibration unfortunately, this option was not feasible. Outdoor testing and calibration present an alternative, but it presents a serious problem which is the uncontrollable test conditions such as irradiance and temperature.

7.3.1 The PV array characteristics

The PV array consists of 15 modules connected in series with two strings connected in parallel. Each module contains 36 cells all connected in series with a sensitive cells area of 0.37 m^2 . According to the manufacturer's specifications, the characteristics of each of these modules "KYOCERA LA 361K51", under standard conditions (i.e. $T = 25^\circ\text{C}$, $G = 1000 \text{ W/m}^2$, AM = 1.5) are as given in table 4.1. The PV array was fitted with diodes for protection against reversed current flow. It was mounted in a fixed frame facing south with 35° inclination to the horizontal. The PV array is over 15 years old and has been exposed to dust accumulation on the surface, rain, pigeons and sea birds dejection. Special care was taken to avoid the effects of such outdoor elements, by thoroughly cleaning the array surface before any experiment. A small water storage tank was installed in the vicinity of the array for this purpose. A Kipp & Zonen Pyranometer fixed at the top of the PV array frame at same tilt angle as that of array was used for measuring the solar irradiation incident on the PV array surface. The data was recorded by a data acquisition system (CIMEL). The system components are shown in figure 7.10.



Figure 7.10 PV array insolation measuring equipment on top of roof at University of Science & Technology of Oran.

Figure 7.11 below shows a typical recorded data and plotting in the electrical plane. The PV characteristics curve fitting was done with the help of the model described in earlier chapters.

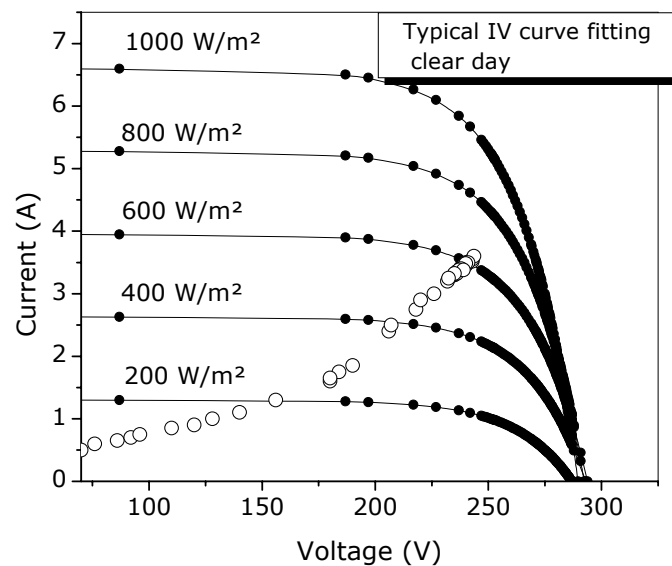


Figure 7.11 IV curve fitting for a clear day recorded at UST Oran.

The panel rear temperature was measured and its variation with ambient temperature and solar irradiation, the result is plotted in figure 4.14

7.3.2 The D.C. motor characteristics measurements

The motor used in this experimental work is a multi-purpose motor manufactured by LEROY SOMER, it requires one horse power at 1750 rpm with a nominal voltage of 180 V and current 4.9 A (see figure 7.12). Initial tests were carried out on the dc motor, and additional parameters such as armature resistance, rotational speed constant and torque constant, were determined. A permanent magnet dc motor as described in chapter 4, is assimilated to a voltage source in series with the motor's armature resistance R_a , and the back e.m.f. of the motor generated by the rotating armature, E , the motor equations can be written as follows:

$$V_M = R_a I_a + K_{SP} \omega$$

$$T_M = K_T V_M$$

The armature resistance was calculated by using the locked-rotor test results and motor equations by setting $\omega = 0$, it was found to be:

$$R_a = \frac{V_M}{I_a} = 2.8\Omega$$

From the no-load test results and motor equations the rotational speed constant and torque constant are equal to:

$$K_{SP} = \frac{V_M - R_a I_a}{\omega} = 0.8872 \text{ Vs/rad}$$

$$\text{and } K_T = 0.8872 \text{ Nm/A}$$

From the motor rated values and by substituting the locked-rotor test armature resistance value, the motor rotational speed constant is found to

$$\text{be: } K_{SP} = \frac{(180V) - (2.8\Omega)(4.9A)}{(183.26 \text{ rads}^{-1})} = 0.9078 \text{ Vs/rad}$$

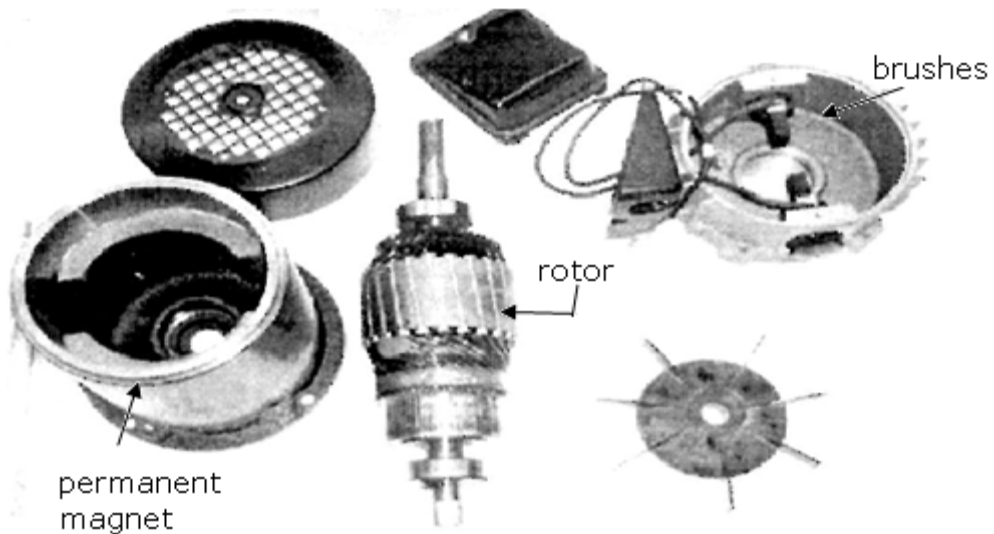


Figure 7.12 D.C. motor (LEROY SOMER) elements.

It has to be noted that the permanent magnet motor had extended brush life and never suffered any damage or malfunctioning during the whole testing period, more than that, the motor was used during the same period for a number of other projects, solar energy power vehicle among others.

7.3.3 The centrifugal pump characteristics

A multipurpose centrifugal pump ELECTROPOMPE CM100 (see figure 7.13), available in the local market was used. The pump has one impeller with a pumping capacity of 80 l/min and a maximum pumping head of 33 m at a nominal speed of 2850 rpm, requiring a power of 750 W. Since no additional data were given by the manufacturer, the pump was dismantled to obtain the relevant information especially the impeller dimensions, these are listed below:

Inlet impeller diameter $d_1 = 33.5$ mm.

Outlet impeller diameter $d_2 = 160$ mm.

Inclination angle of impeller blade at impeller inlet $\beta_1 = 38^\circ$.

Inclination angle of impeller blade at impeller outlet $\beta_2 = 33^\circ$.

Height of impeller blade at impeller inlet $b_1 = 5.4$ mm.

Height of impeller blade at impeller outlet $b_2 = 2.2$ mm.

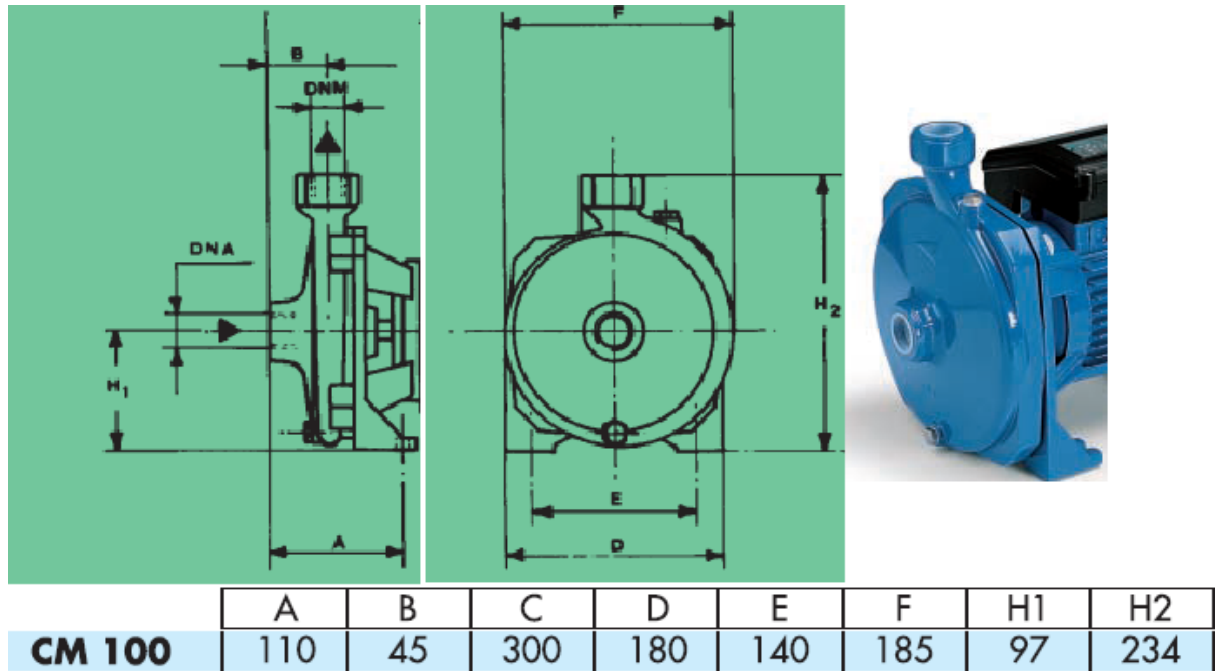


Figure 7.13 Centrifugal pump used in this work (ELECTROPOMPE CM100)
all dimensions in mm.

As it was already explained in chapter 6, the pump impeller develops a torque required to pump a specific quantity of water, this torque is expressed as a constant times the square of the rotational speed of the pump shaft (equation 6.27). The constant is function of the impeller dimensions, thus the pump torque is written as:

$$M_p = K_m \omega_p^2 , \text{ where } K_m \text{ is expressed as follows:}$$

$K_m = \rho 2\pi R_1^2 b_1 \tan\beta_1 (R_2^2 - \frac{R_1^2 b_1 \tan\beta_1}{b_2 \tan\beta_2})$, in our case and by substituting impeller dimensions, we get $K_m = 5.3730 \cdot 10^{-5}$. Figure 7.14 shows manufacturer pump product line and the data sheet provided, representing pumps head as function of flow rate at a specific rotational speed of 2850 min^{-1} .

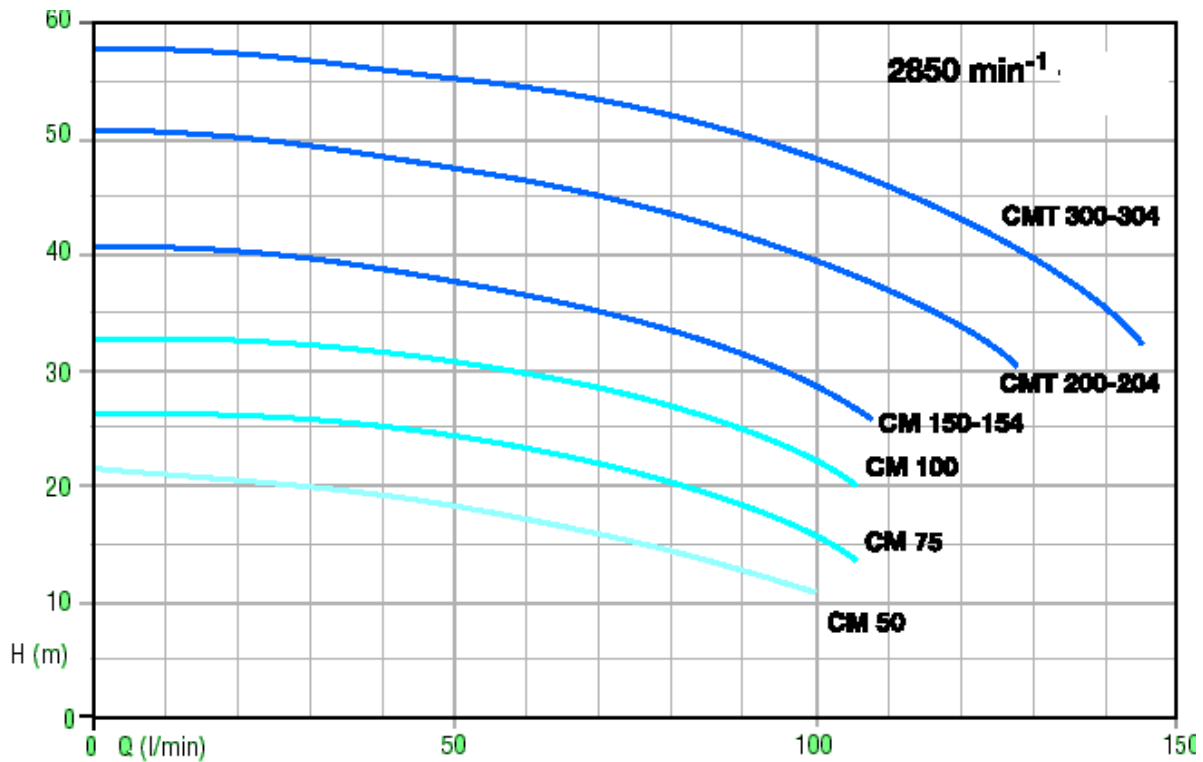


Figure 7.14 Manufacturer pump characteristics.

7.4 The experimental test bench

The experimental test bench installed at Oran University of Science and Technology on top of the department of electronics roof (latitude 35.69° , longitude -0.64°) is shown in figure 7.15. Three main design parameters that affect the performance of directly coupled PV systems at a given location (under particular climatic conditions) were taken into account during the early design of test bench. Based on these design parameters the installed directly coupled PV water pumping system comprises of:

- PV array – 30 PV modules, arranged in two parallel columns, each of 15 modules, connected in series,
- Motor-pump assembly – a permanent magnet dc motor coupled with a single impeller centrifugal pump,
- Water Storage Tanks – two identical storage tanks and a set of piping.

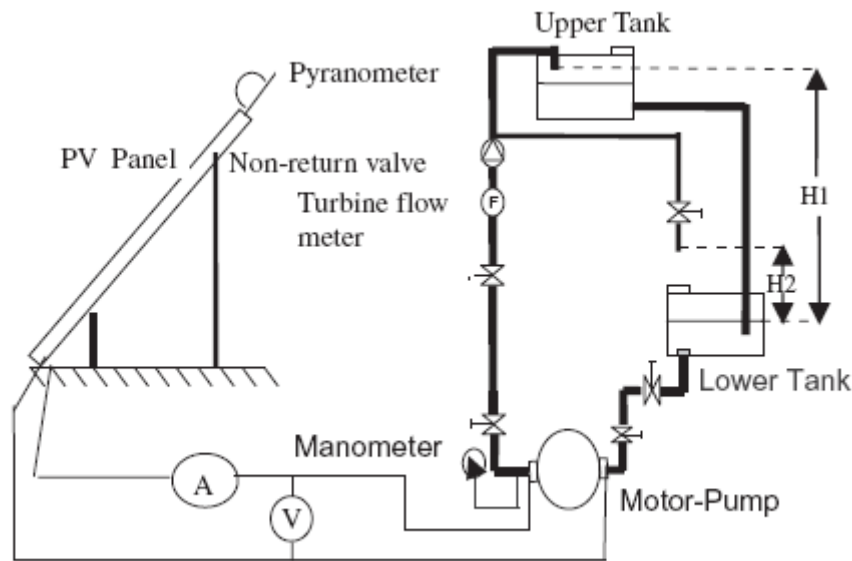


Figure 7.15 Schematic diagram of the closed loop test bench at UST Oran

Such a system serves similar purpose to that of battery storage and power point tracker systems. The later have improved efficiency, but are more expensive. A directly coupled system on the other hand is low cost most reliable PV system (Anis. WR, Nour. MA, 1994). The performance of such a system can be optimized by varying the size of the PV array (a predominant factor), its orientation and pump-motor- hydraulic system characteristics (Ghoneim. AA, 2006). With the exception of PV modules all system components are locally available. An off the shelf motor-pump is experimentally studied and mathematically modeled. The lower tank together with the motor-pump set and all measuring equipments were installed at the Power Electronics and Solar Energy Laboratory. The upper tank was installed on the roof of the double storey building, Department of Electronics. The experimental rig is a closed loop system, fitted with manual valves that enable to run the test with two static heads, 0.60 m and 11 m alternately. To assure the self-priming the pump was placed below the lower tank outlet level. The flow rate was measured with a plastic turbine flow meter installed in the delivery pipe line. Kipp & Zonen Pyranometer fixed at the top of the PV array frame at same tilt angle as

that of array was used for measuring the solar irradiation incident on the PV array surface. The equipment used for measuring various parameters and their accuracy are listed in table 7.1.

Table 7.1 Measuring instruments and their approximate accuracy.

Measured parameter	Instrument	Accuracy
Flow rate	Kobold DF sensor with frequency output	$\pm 2.5\%$ of full scale
Pressure (head) transmitter	Siemens SISTRANS P series Z 7MF 1563	$\pm 2.5\%$
Irradiance	Kipp & Zonen CM11 Pyranometer	$\pm 3\%$
Tension	Voltmeters	$\pm 0.5\%$
Current	Ammeters	$\pm 0.5\%$

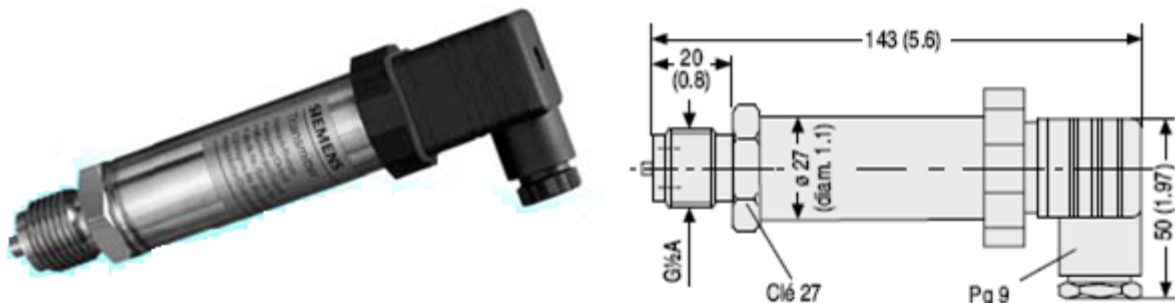


Figure 7.16 pressure transmitter 7 MF 1563 all dimensions in mm (inch)

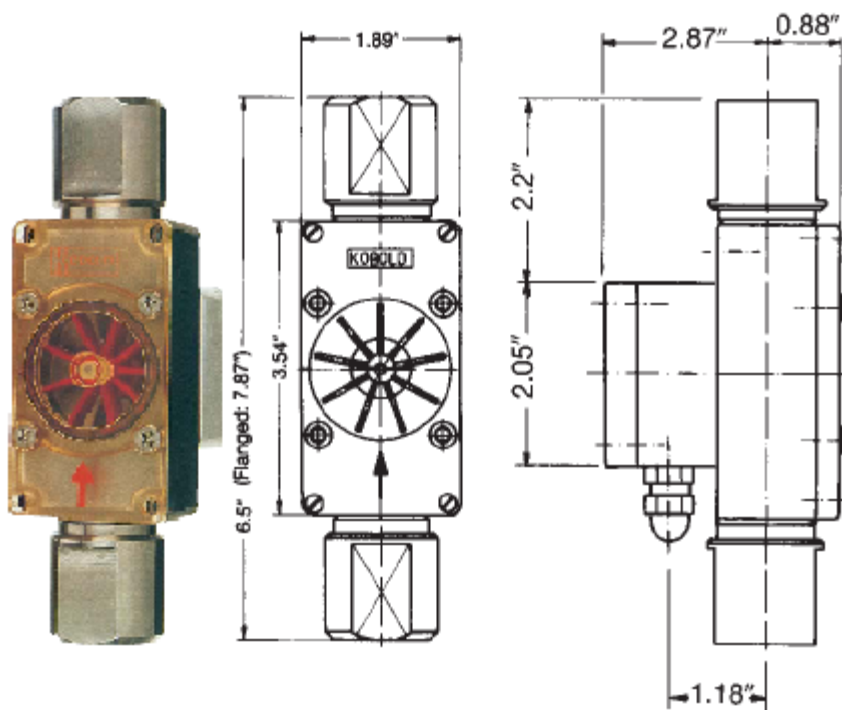


Figure 7.17 Flow meter Kobold DF dimensions

Figures 7.16-17 show the pressure transmitter (Siemens 7 MF 1563) and the plastic flow meter (Kobold DF) used to measure the pressure output of the pump and the water flow delivered in the hydraulic circuit respectively. The flow rate calibration diagram is shown in figure 7.18 below.

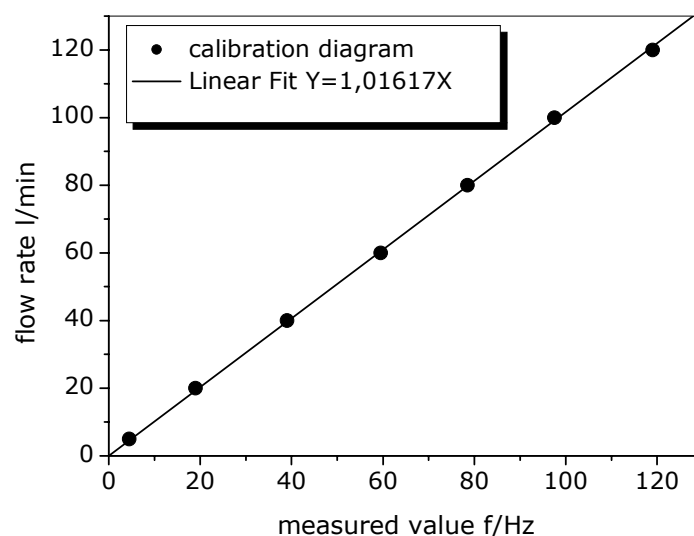
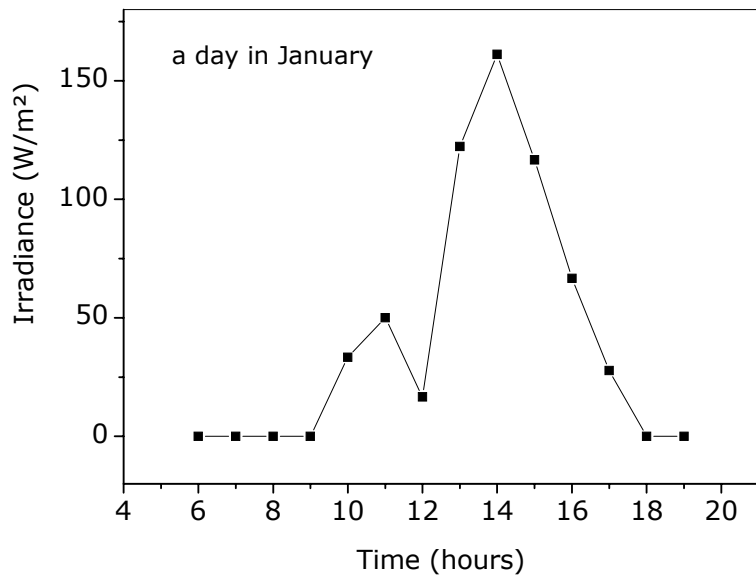


Figure 7.18 Flow meter calibration graph.

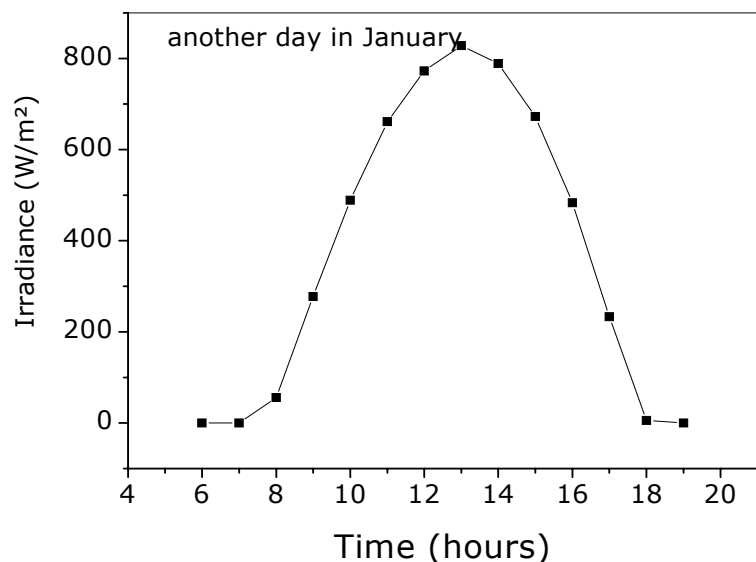
The hydraulic system comprises of two identical galvanized steel tanks, 2 m³ of capacity each, fitted with valves (one non-return valve), and flow meter. Galvanized steel pipes, 33 mm diameter were used because of their robustness, availability and low cost. The hydraulic system was divided into two operational sets as – a long and a short hydraulic system. The long hydraulic system consists of static head 11 m, suction line 4 m and delivery line 20 m, while the short hydraulic system has static head 0.60 m, suction line 4 m and delivery line 8 m.

7.5 Testing procedure and analysis

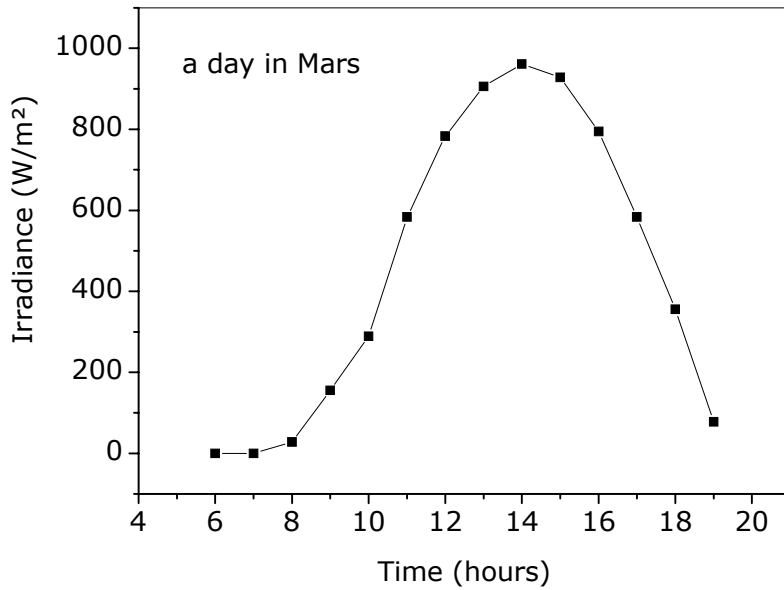
Performance of the installed PV operating water pumping system was monitored under outdoor conditions for over a year period in order to evaluate its performance under different atmospheric conditions ranging from completely overcast to totally clear sky. The system was tested with two different static heads. Prior to that the system was tested and all its elements calibrated by means of a fixed DC power source. All relevant operational parameters for the system, such as solar irradiance, ambient temperature, load current, load voltage, rotational speed, pressure at pump outlet and flow rate were collected over the test period. The aims of the test were, (i) to find how the system performance varies with changing climatic conditions, i.e solar irradiance, figures 7.19(A) to (F) illustrate changing diurnal solar irradiance values, hence different sky conditions, and (ii) to look at the effect of the hydraulic system configurations, i.e static head, on system performance. A comparative graphical representation of the daily solar irradiation for mean values and TMY values is represented in figure 7.20a and b.



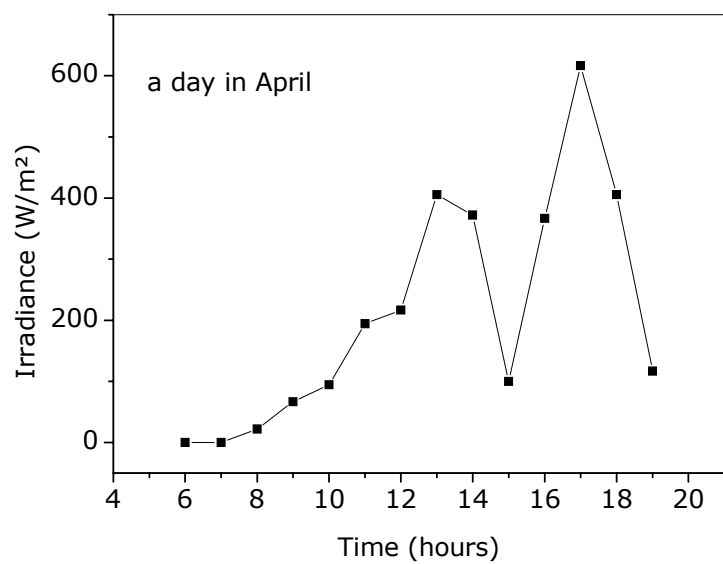
(A)



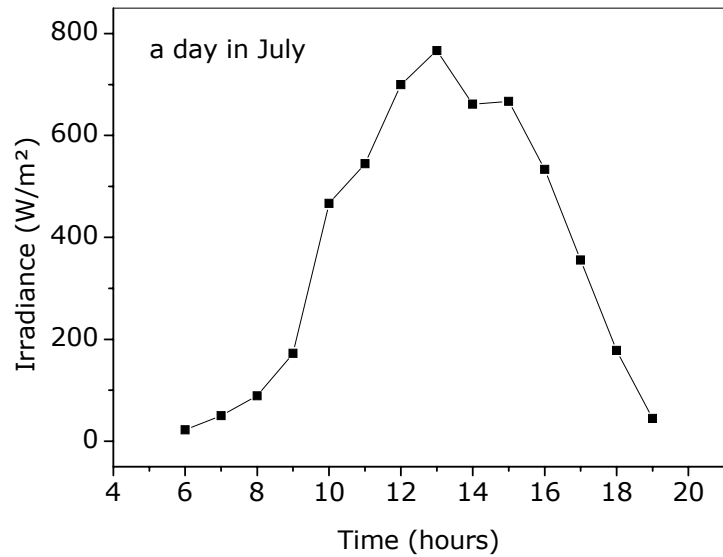
(B)



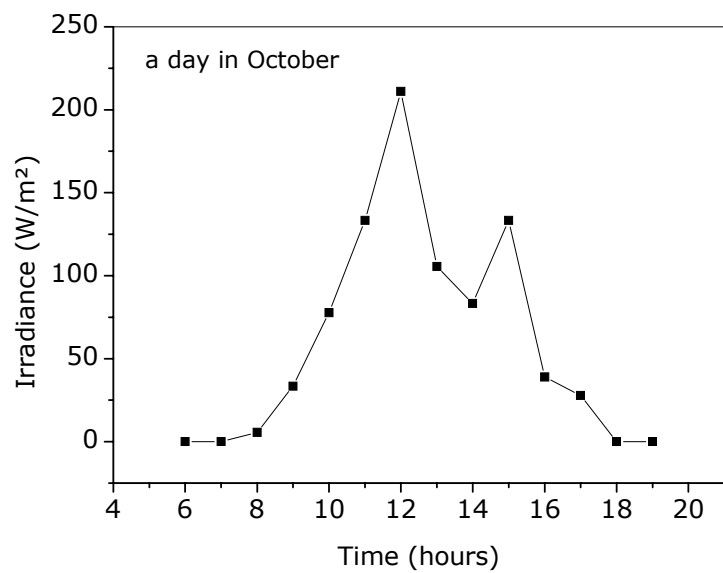
(C)



(D)



(E)



(F)

Figure 7.19 Daily solar irradiance recorded at UST Oran.

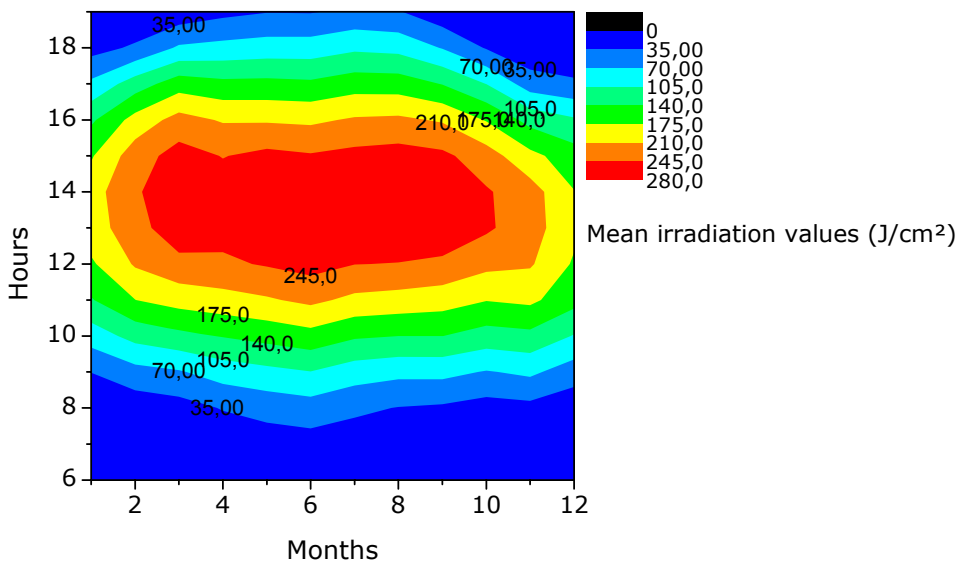


Figure 7.20a Daily mean solar irradiation distribution over a year recorded at UST Oran.

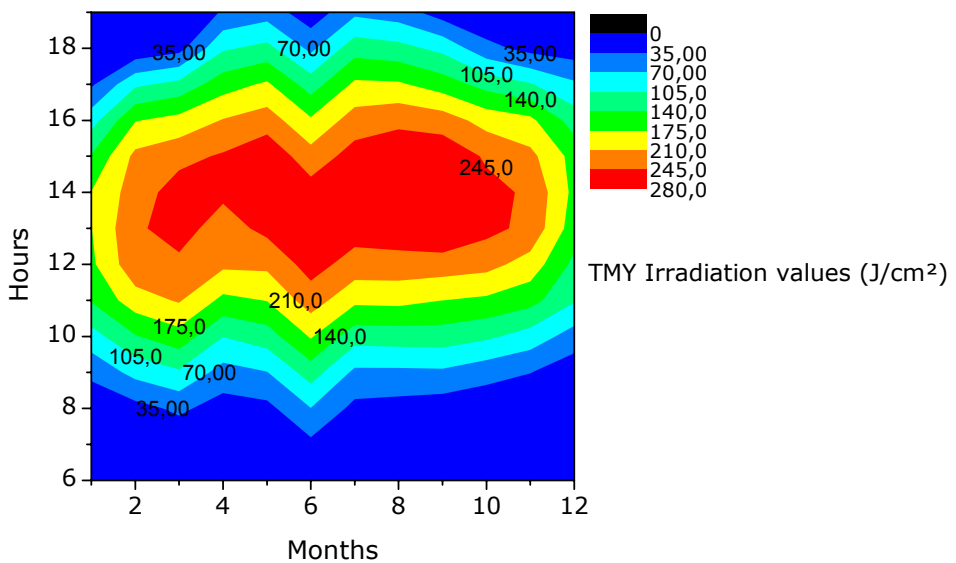


Figure 7.20b Daily mean solar irradiation distribution for a Typical Meteorological Year recorded at UST Oran.

It is obvious that the key to analyzing the performance of direct coupled PV pumping system is the electrical plane, where the motor–pump current versus voltage characteristics or I–V load curve and PV array family of I–V

curves are required. These curves are drawn in figure 7.21 by means of the model described in chapter 4, the operating point curve or load curve is also reported in that figure.

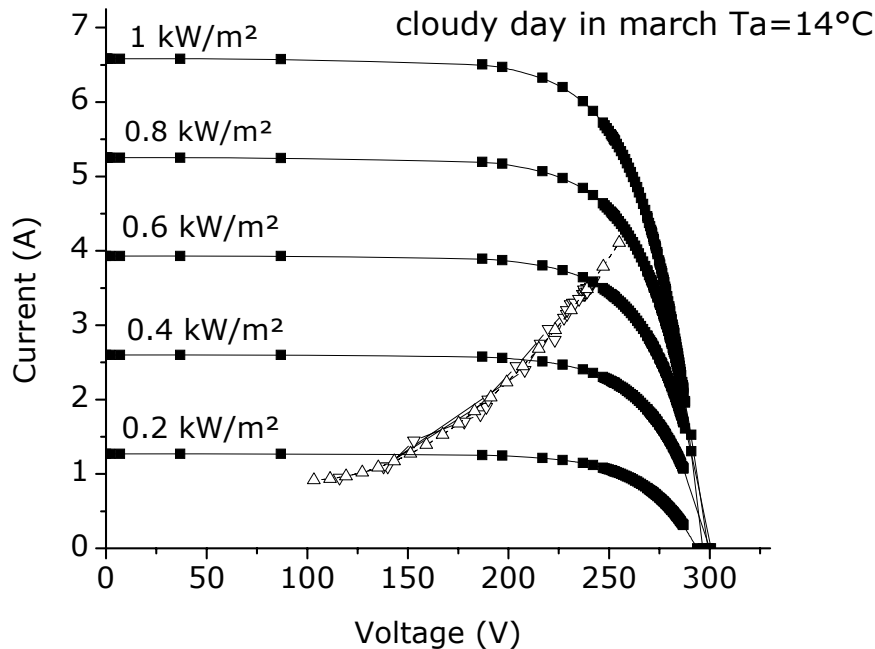


Figure 7.21 I-V characteristics of the PV array measured at UST Oran.

Starting and stopping the system was done manually. Pumping continued all through the year under different sky conditions and no significant malfunction was recorded, except the fact that the early morning starting varied according to climate conditions until the solar panels could deliver the energy needed to start pumping. Late afternoon at sun set PV panels could not deliver enough energy to the motor (pump), so the motor (pump) kept running empty (no pumping). To avoid the pump (motor) running on empty, the motor (pump) was connected to the panels only once the power delivered by the PV panel was sufficient to allow the pump to pump effectively (overcome the static head), which has required continuous surveillance of the system.

The system performance is presented in I-V curves in figure 7.21. As observed from the figure the system activates at irradiance of 160 W/m^2 and continues operating most of the day between 300 and 700 W/m^2 of irradiance. The system requires an activation current of about 1 A that corresponds to irradiance of 160 W/m^2 . The activation current is the value at the instant when voltage is applied to the motor and the system is at standstill (rotational speed nil). We may distinguish between activation current which is starting of system rotation and starting of water pumping which usually take place at different times (Singer S, Appelbaum J, 1993). The activation (starting) current, limited by the short-circuit current as expressed in equation 4.20, is a linear function of irradiance. As soon as the system starts rotating, the starting current decreases with increasing voltage until a steady-state is reached, which eventually corresponds to the operating point assuming a constant irradiance.

The flow rate versus day time for two typical days in December and March and for two static heads is plotted in figure 7.22. The system starts pumping at 09:00 h for a static head of 11 m in March (around 08:00 in June and July), whereas pumping did not begin until 10:00 h in December, even with a low static head (0.60 m). Depending on the solar irradiance and hydraulic system configuration the flow rates vary between 6 to 65 l/min and pumping hours from 6 to 8 h. Rapid fall in values are mainly due to scattered clouds obstructing incoming solar radiation.

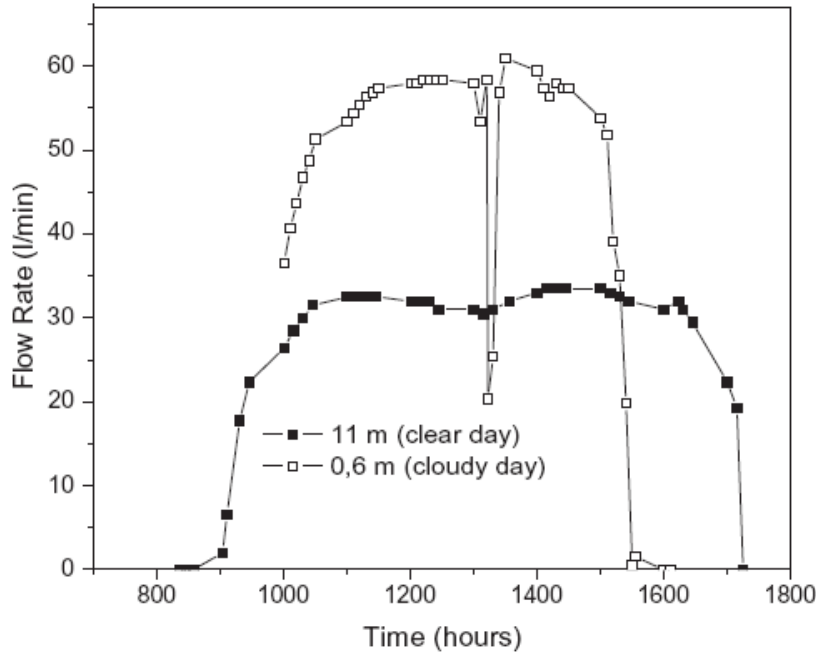


Figure 7.22 Daily flow rate for two static heads
(Mokeddem A. et al, 2011).

Relationship between flow rate and motor-pump input power is drawn in figure 7.23 As observed from the figure, the pump cannot overcome the static head until a minimum of 288W of power is supplied to the motor-pump at a static head of 11 m and 50W at 0.6 m. Flow rate as function of the solar irradiance is plotted for two worst cases in figures 7.24(a) and (b), where an irradiance threshold value of about 180 W/m² is needed for the system to operate at a static head of 11m, whereas a minimum of 100 W/m² of solar irradiance is needed for a static head of 0.6m. It should be noted that for the same value of irradiance the system does not necessarily deliver the same quantity of water. We also noted that pumping was more efficient during the second part of the day than during the first. This was probably due to the inertia of the motor-pump. The phenomena should be looked at more deeply in future investigations.

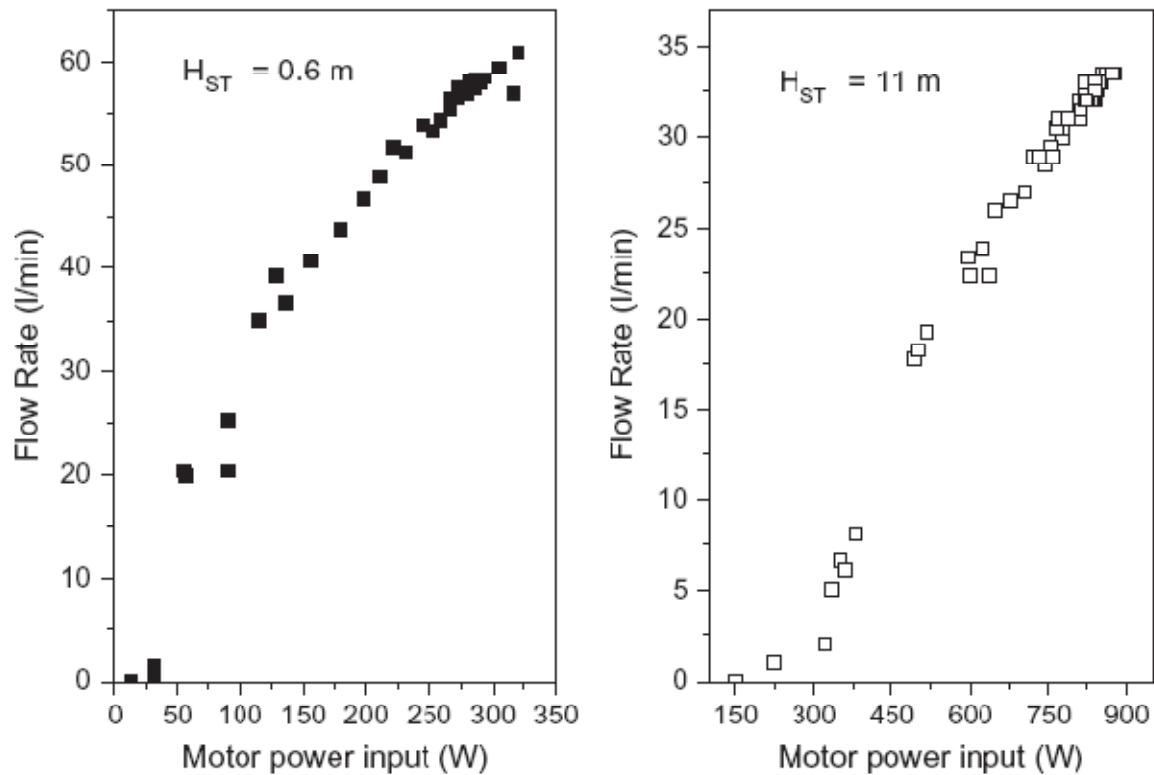


Figure 7.23 Flow rate variation with power motor-pump power input
(Mokeddem. A. et al, 2011).

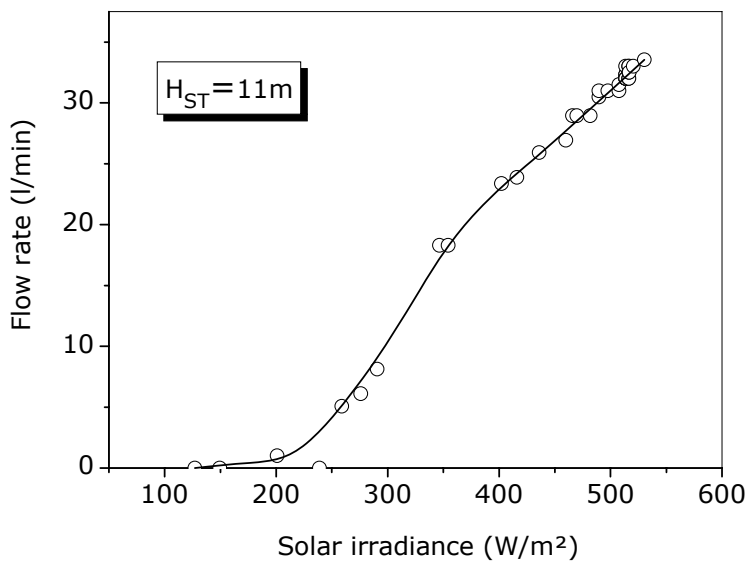


Figure 7.24(a) Flow rate versus solar irradiance (recorded at USTO)

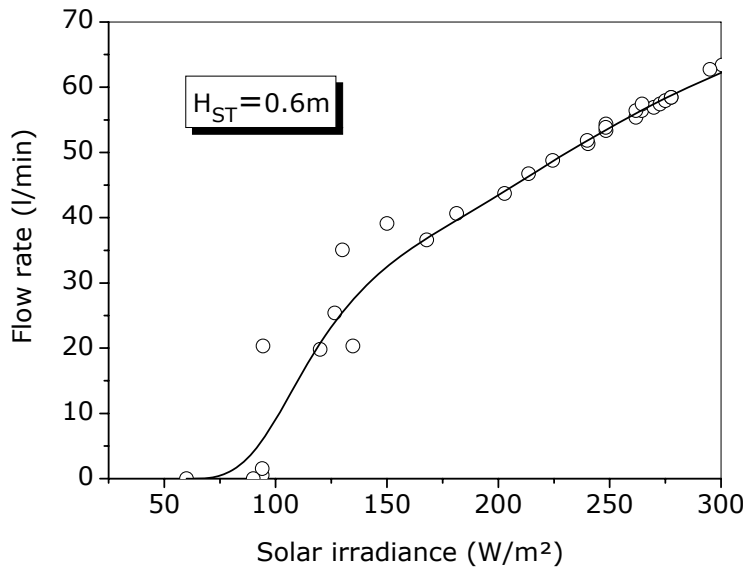


Figure 7.24(b) Flow rate versus solar irradiance (recorded at USTO)

In figure 7.25, the flow rate versus voltage profile shows, a minimum voltage required to start water pumping. The total head developed by the pump versus voltage curve for two static heads in figures 7.26(a) and (b) indicates that the pump starts to develop head soon after the voltage is above the start rotation threshold. However, flow does not begin until the pump develops enough head to overcome the static head, it shows also that the operating voltage is around 240 V for the most part of day (at $H_{ST} = 11\text{m}$) and around 140 V (at $H_{ST}=0.6\text{m}$). From figure 7.27 one can notice that motor-pump efficiency never reached 30% at static head of 0.6 m and just exceed 12% value at 11 m of static head. At low static head motor-pump operating rotational speed values were in the region of the motor rated speed, whereas at $H_{ST}=11\text{m}$ the motor-pump was operating beyond motor rated speed (2600 rpm). That also means, that the motor has greater impact on motor-pump overall efficiency than the pump. It has to be mentioned that the system had to be stopped late afternoon since the pump continued rotating without pumping. The dc motor used by Benlarbi et al (Benlarbi K, Mokrani L, Nait-Said MS, 2004) in their PV water pumping system has identical characteristics to those described in our work. Despite having the pump speed rate equal to the motor rating

speed, it was found that the system efficiency never exceed 9% with or without fuzzy optimization. The results are compared in figure 7.5.10, flow rate against pump speed.

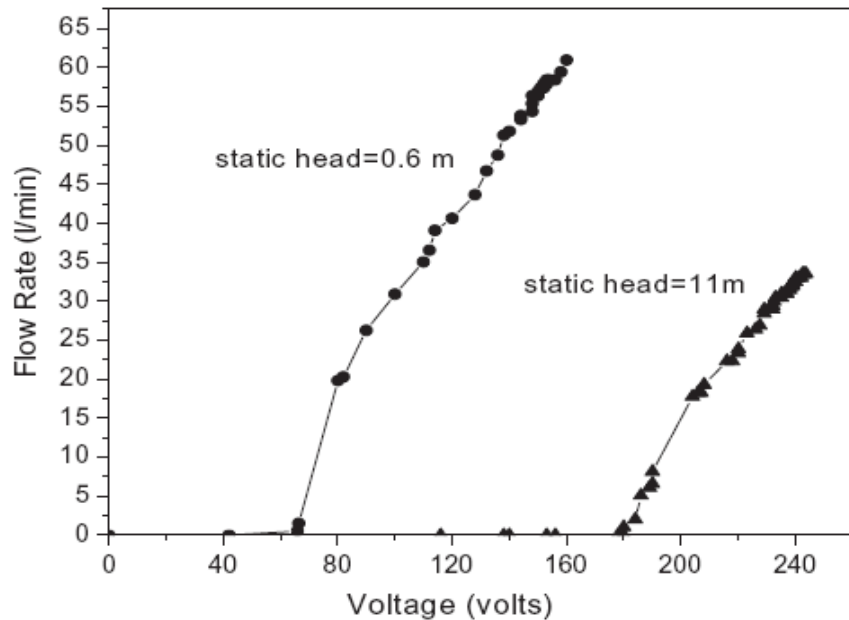


Figure 7.25 Motor-pump flow rate versus operating voltage (Mokeddem. A et al, 2011)

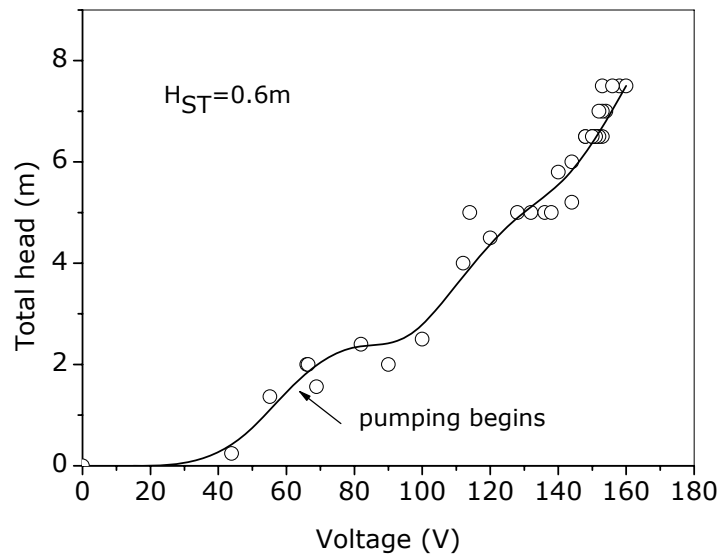


Figure 7.26(a) Pump head developed as function of the motor voltage input (recorded at USTO)

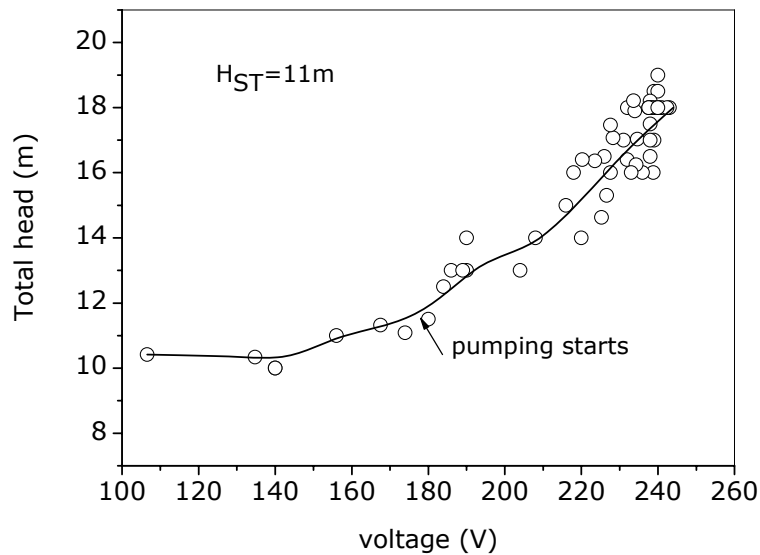


Figure 7.26(b) Pump head developed as function of the motor voltage input (recorded at USTO)

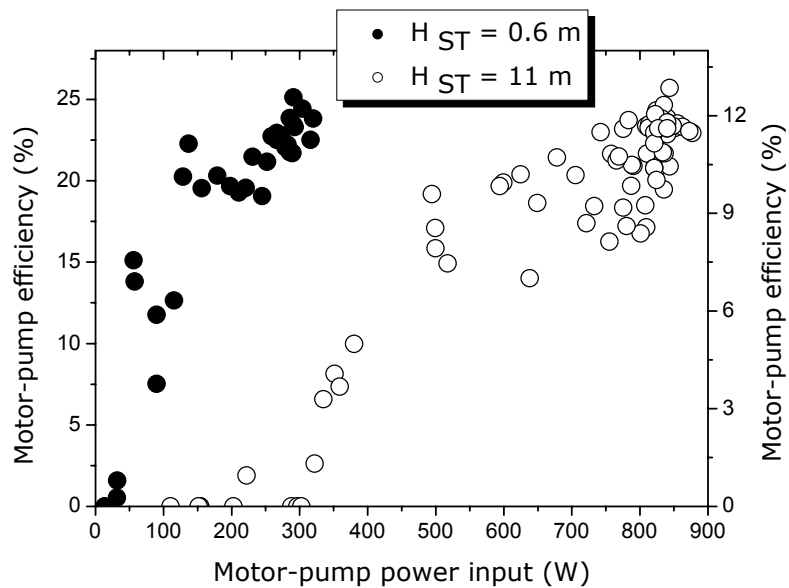


Figure 7.27 Subsystem efficiency as function of the power input (Mokeddem. A et al, 2011)

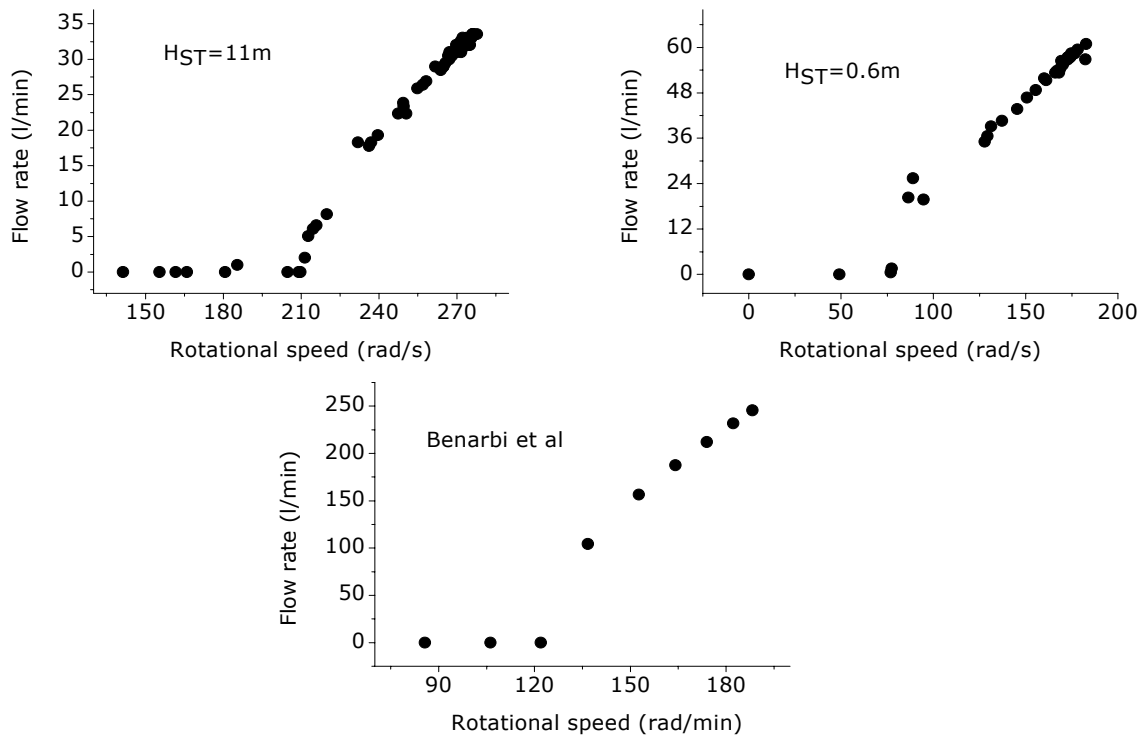


Figure 7.28 Flow rate versus rotational speed comparison with (Benlarbi et al, 2004).

GENERAL CONCLUSIONS AND PERSPECTIVES

We had fixed several goals to be achieved through this work outlined in early chapters. One of the aims is to establish a mathematical model for different elements of the photovoltaic pumping system, then to assemble a test rig for experimental testing, which is used to validate the mathematical model of different components of the system.

The system model was simplified down to its basic equations because we found, in preliminary testing, that most models reported in the literature are cumbersome with lengthy algebraic manipulations without providing a further improvement. The predicted overall system performance was also found to agree reasonably with the experimental measurements (figures 7.7-8).

The quantity of water delivered by the pump was measured for two different static heads only. It was hoped that the system could be configured for other static heads, not only, but also for changeable pipe diameter and type of pumps. Unfortunately, and because of limited facilities and funding at the power electronic and solar energy laboratory (LEPES), this was not possible.

The performance of the directly coupled PV water pumping system has been monitored at different conditions of varying solar irradiance values and two static head hydraulic system configurations. The system had to be and is a low cost design, using local components not necessary designed for photovoltaic pumping, without any complex electronic control and auxiliary systems. It has been observed that the system is suitable for low delivery flow rate applications.

The system pumps water during the day time for over 8 hours (09:00 to around 17:30 h). It runs without external intervention so long as sun is shining on the panels and pumped water is stored in the upper storage

tank before returning back by gravity to the lower tank. The system is switched off in the late afternoon to prevent motor-pump overheating.

It is clearly evident that such a system is simple, easy to install and would operate with minimum maintenance.

The system is useful for applications such as irrigation, watering cattle and maintaining domestic water supplies, particularly in remote areas where access to water (often low head communicating wells system such as traditional irrigation systems foggaras in the southern west of Algerian Sahara) is so much time and labor demanding, which evidently affects the community's life quality.

The efficiency of the system can be improved by carefully selecting the size of the array, its orientation and motor-pump system nominal characteristics.

To my knowledge no photovoltaic pumping system performance data in the region of Oran or even in the west of Algeria has been reported in the literature.

Monitoring the performance of such system and gathering as much information as possible, in a kind of chart, may give a better picture of how and where improvements have to be made. This work falls within the framework of a strategy which should present to local or even national decision makers to what kind and size of system fits better that kind of specification.

Local weather has proved to have a direct impact on photovoltaic pumping system performance. That is why we recommend, through this work the University of Science and Technology of Oran to acquire a micro climate station designed primarily in recording solar irradiance wind speed and ambient temperature parameters in order to build a specific climate database. Knowing that many laboratories within USTO are engaged to some extent in renewable energy projects the database will constitute the base of different solar energy research projects.

The enthusiasm aroused by the integration of solar energy in various sectors of national economy in general, agriculture in particular, has

encouraged many small farmers to consider favorably the photovoltaic option in their exploitations specially for pumping. However, communication work with these "exploitants agricoles" is still necessary to popularize the use of photovoltaic pumping which is the subject of this research. Farmers with whom we have made a survey are small (three to five hectares) "exploitants" most of them in isolated west high land (hauts plateaux) regions. The majority of these farmers see in the photovoltaic pumping an opportunity to resolve once and for all their main problem which is water for irrigation, because accessing to water, in their point of view, is prior to any kind of efficiency or economic issues. Installing small working photovoltaic pumping system at the University of Science and Technology of Oran may help to narrow the gaps and answer all kinds of questioning that actual or future user of photovoltaic pumping might ask. We have considered through this work only direct coupling of photovoltaic pumping systems because, and this is one of the results of our survey, direct coupling a DC motor to the PV array fits perfectly in the pedagogic work process that has to achieved and also any sophistication added to the system for efficiency improvement will have a negative response from the farmers. We are convinced that the introduction of renewable energies in general and photovoltaic pumping in particular is in one hand, a solution for the future of agriculture in isolated regions in Algeria and in the other hand, we are profoundly concerned to see things pedagogically and gradually done.

Broadening the use of DC motors implies necessarily the boost of manufacturing or assembly industry of this type of motors.

As it is said "a thousand miles journey starts with one step".

REFERENCES

Algerian ministry of energy and mines www.mem-algeria.org/.

Anis. WR and MA. Nour, Optimum design of a photovoltaic powered pumping system. Journal of Power Sources; 50, 1994, 1-9.

Anis. WR, MA. Nour, Switching mode photovoltaic pumping system. Energy Convers Manage 1994;35(9):765-73.

Appelbaum. JA, Operation of D.C. motors powered by photovoltaic converters. Electrical Machines and Electromechanics, 3(3), 209-220, 1979.

Appelbaum. JA and J. Bany, Performance analysis of D.C. motor-photovoltaic converter system-I. Solar Energy 21, 439-445, 1979.

Appelbaum. JA, Performance analysis of D.C. motor-photovoltaic converter system-II, series and shunt excited motors. Solar Energy 27, 421-431, 1981.

Appelbaum. JA, Starting and steady-state characteristic of D.C. motors powered by solar cell generators. IEEE Transactions on Energy Conversion, Vol. EC-1, March, 1986.

APRUE, Agence Nationale Algérienne de Promotion et de Rationalisations de l'Utilisation de l'Energie <http://www.aprue.org.dz/>, 2008.

Benlarbi. K, Mokrani. L, Nait-Said. MS, A fuzzy global efficiency optimization of directly coupled PV pumping system. Sol Energy 2004;77(2):234-44.

Braunstein. A, Kornfeld. A, Analysis of solar powered electrical water pumps. Solar Energy 27 (3), 235-240, 1981.

Chandratilleke. TT and J. Ho, A study of a photovoltaic array for water pumping. Solar & wind technology; 3(1), 59-71, 1986.

Church. A. H, Centrifugal pumps and Blowers. John Wiley and Sons, INC. New York, 1945.

Davis. M, Fanney. A, Dougherty. B, Prediction of Building Integrated Photovoltaic Cell Temperatures. *ASME Journal of Solar Energy Engineering*, Volume 123, Number 3, Pages 200-210, 2000 .

Del Cueto. J, Model for the Thermal Characteristics of Flat-Plate Photovoltaic Modules Deployed at Fixed Tilt. *Proceedings of the 28th IEEE PV Specialist Conference (PVSC)*, Anchorage, AK, 2000.

Douglas. JF, JM. Gasiorek and JA. Swaffiel, Fluid mechanics. Longman Scientific and Technical, England, 1985.

Duffie. JA, WA. Beckman, Solar engineering of thermal processes. John Wiley and Sons, New York, 1980.

Duffie. JA, Beckman. WA, Solar Engineering of Thermal Processes, third ed. John Wiley & Sons Inc., New York, 2006.

[El Paso Solar Energy Association, www.epsea.org](http://www.epsea.org), 2007.

Faldella.E, GC.Cardinali and PU. Calzolari, Architectural and design issues on optimal management of photovoltaic pumping systems. IEEE transactions on industrial electronics; 38(5), 1991, 385-392.

Firatoglu.ZA and B.Yesilata, New approaches on the optimization of directly coupled PV pumping systems. Solar energy; 77, 81-93, 2004.

Ghoneim. AA, Design optimization of photovoltaic powered water pumping systems. Energy Convers Manage;47(11–12):1449–63, 2006.

Grassie. T, MacGregor. K, Muneer. T, Kubie. J, Design of PV driven low flow solar domestic hot water system and modeling of the system collector outlet temperature. Energy Convers Manage;43(8):1063–78, 2002.

Green. MA, Emery. YK, King. DL, Hisikawa. Y, Warta. W, Proggress in photovoltaics : research and applications. Short communication, 2006.

Grundfos.com/doc/webnet/cr/int/technical.htm.

Hahn. A, Photovoltaic water pumps. Gate technical information E4e. GTZ-OE4429, May 2000.

Halcrow.w and partners in association with the Intermediate Technology Development Group Ltd, Small-scale solar powered irrigation pumping systems: Phase I project report: prepared for the World Bank. UNDP Project GLO/78/004, 1981.

Hamdy.MA, A new model for the current-voltage output characteristics of photovoltaic modules. Journal of power sources; 50, 11-20, 1994.

Hamid. M, Metwally. B, Anis. WR, Dynamic performance of directly coupled photovoltaic water pumping system using D.C. shunt motor. Energy Convers Manage;35(9):1407–16, 1996.

Hsiao. YR and BA. Blevins, Direct coupling of photovoltaic power source to water pumping system. *Solar energy*,; 32(4, (1984), 489-498, 1984 .

IEA PVPS , annual report, www.iea-pvps.org, 2008.

Kaldellis. JK, GC. Spyropoulos, KA. Kavadias and IP. Koronaki, Experimental validation of autonomous PV-based water pumping system optimum sizing, *Renewable Energy*, 34(4), 1106-1113, 2009.

Kamel. YK, Optimum Load matching in Direct-coupled Photovoltaic water systems-Application to resistive loads. *IEEE Transactions on Energy Conversion*, Vol. 5, N° 2, June 1990.

Kaneka, Products (Amorphous). Retrieved from:
<http://www.pv.kaneka.co.jp>, December 11, 2009.

Kenjo. TA, Nagamori. S, Permanent-magnet and brushless D.C. motors. Oxford Science Publications, England, 1985.

Khallat. MA, Rahman. S, A probabilistic approach to photovoltaic generator performance prediction. *IEEE Transactions on Energy Conversion*, Vol. Ec-1, N°.3, September, 1986.

King. DL, Photovoltaic module and array performance characterization methods for all system operating conditions. Proceedings of NREL/SNL photovoltaic program review meeting, November 18-22, Lakewood 1996 .

Klein. SA, Beckman. WA, Duffie. JA, A design procedure for solar heating systems. *Solar Energy*, 18, 113-127, 1975.

Kolhe.M, C. Joshi and DP. Kothari, Performance analysis of a directly coupled photovoltaic water-pumping system. IEEE transactions on energy conversion; 19(3), 2004, 613-618.

Kohonen. T, Self Organized Formation of Topologically Correct Features Maps, Biological Cybernetics, Vol.43, 1982.

Kohonen. T, Self-Organizing Maps, 2nd edition, Springer-Verlag, 1995).

Kohonen. T, Hynninen. J, Kangas. J, and Laaksonen. J, SOM_PAK: The self-Organizing Map Program Package, Technical Report A31, Helsinki University of Technology, Laboratory of Computer and Information Science, FIN-02150 Espoo, Finland, 1996.

Kovats. A, Desmur. G, Pumps, fans and compressors. Blackie and Son Ltd, London, 1958.

Kovats. A, Design and performance of centrifugal and axial flow pumps and compressors. Pergamon Press, London, 1964.

Luque. A et. Al, Handbook of Photovoltaic Science and Engineering. John Wiley & Sons Inc., New York, 2003.

MEM, Ministry of Energy and Mines, New and Renewable Energies, <http://www.mem-algeria.org/>, 2008.

MME, Ministry of Mines and Energy, Final Report "Feasibility Assessment for the Replacement of Diesel Water Pumps with Solar Water Pumps, MME; Windhoek, Namibia, 1996.

Moechtar. M, Juwono. M, Kantosa. E, Performance evaluation of a.c. and d.c. direct coupled photovoltaic water pumping system. Energy Convers Manage 1991;31(6):521-7.

Mokeddem. A, Midoun. A, Ziani. N, Kadri. D, Hiadsi. S, Test and analysis of a DC-motor pumping system, ICTON Mediterranean Winter Conference, ICTON-MW 2007, On page(s) 1-7, Volume: Issue: 6-8 December 2007.

Mokeddem. A, Midoun A, Kadri D, Hiadsi S, Raja IA, Performance of a directly-coupled PV water pumping system. Energy Convers Manage 2011; 52 (10):3089-3095.

Muller. JC, Amelioration attendues avec les nouvelles technologies PV : rendements, couts et cycle de vie. Energie et developpement durable. 14, 15 mars. 2007.

Muneer. T, Asif. M, Kubie. J, Generation and transmission prospects for solar electricity: UK and global markets. Energy Convers Manage 2003;44(1):35-52.

National Instruments, Part II- Photovoltaic Cell I-V Characterization Theory and LabVIEW Analysis Code. Solar Cell characterization web site.

Nozik. A., Efficiency of Converting Solar Irradiance into Electrical or Chemical Free Energy. Presentation, 2005, Golden CO: National Renewable Energy Laboratory. Retrieved from:
<http://www.lbl.gov/solar/pwfiles/plenary/Nozik.Berkeley.Mar05.ppt>

Oleksiy. N, Simulation, fabrication et analyse de cellules photovoltaïques à contacts arrières interdigités, Theses de doctorat, institut national des sciences appliquées de Lyon, 03 May, 2005.

Pokrovsky. OM, On the modeling of surface Meteorological Variable Diurnal Cycles by combining "fuzzy sets and neural networks". In the Proc. of 12th International Symposium "Computer Science for Environmental Protection 98", Metropolis-Verlag, Marburg 1998, pp. 331-345.

Ramos. JS, Ramos. HM, Solar powered pumps to supply water for rural or isolated zones: a case study. Energy Sustain Dev 2009;13(3):35-52.

Rao. VB, C++ Neural Networks and Fuzzy Logic, M&T Books, IDG Books Worldwide, Inc, 1995.

Ricco Rakotomalala, "TANAGRA : un logiciel gratuit pour l'enseignement et la recherche", in Actes de EGC'2005, RNTI-E-3, vol. 2, pp.697-702, 2005.

Risser. V et al, Linear regression analysis of flat plate PV-System Performance data. 5th EC Photovoltaic Conference, Athens, Dordrecht, 1983.

Roger. JA, Theory of direct coupling between D.C. motors and photovoltaic solar arrays. Solar Energy, 23, 193-198, 1979.

Saha Angshuman, Neural Network Based Clustering using Self Organizing Map (SOM) in Excel, 2001.

Schott. T, Operation temperature of PV modules a theoretical and experimental approach. Proc. Of the 6th E.C photovoltaic Solar Energy conf. London; 15-19 April 1985.

Short.TD and R.Oldach, Solar powered water pumps: The past, the present-and the future. Transactions of the ASME, February; 125 (2003), 76-82.

Siegel. MD, Klein. SA and Beckman. WA, A simplified method for estimating the monthly-average performance of photovoltaic systems. Solar Energy 26, 413-418, 1981.

Singer. S and J.Appelbaum, Starting characteristics of direct current motors powered by solar cells. IEEE transactions on energy conversion; 8(1), (19), (1993), 47-53.

Skoplaki. E, Boudouvis. A, Palyvos. J, A Simple Correlation for the Operating Temperature of Photovoltaic Modules of Arbitrary Mounting. Solar Energy Materials & Solar Cells, Volume 92, Pages 1392-1402, 2008 .

Smith.DV, Allison.SV, Micro irrigation with photovoltaics. MIT Energy laboratory, Report N°.MIT-EL-78-006, 1978.

Suehrcke.H, J.Appelbaum and B. Reshef, Modelling a permanent magnet dc motor/centrifugal pump assembly in photovoltaic energy system. Solar energy; 59, (1997), 37-42.

Takahashi. K, Konagai. M, Amorphous Silicon Solar Cells. North Oxford Academic, 1983.

Tiba. C, Barbosa. EM, Softwares for designing, simulating or providing diagnosis of photovoltaic water-pumping systems. Renewable Energy, 25. 101-113, 2002.

Twidell. JW, AD. Weir, Renewable energy resources. E&FN. Spon Ltd. London, 1986.

Twidell. JW, AD. Weir, Renewable energy resources. Taylor & Francis. Oxford, 2006.

Van Overstraeten. RJ, RP. Mertens, Physics, Technology and use of Photovoltaics. Adam Hilger Ltd. Bristol, 1986.

Xinchang. Products – Cell, Retrieved from: <http://www.e-polysilicon.cn>, December 11, 2009.

Xu. R, Wunsch. DC, Clustering, John Wiley & Sons, Inc., Hoboken, New Jersey, 2009.

Weiner. D and A. Levinson, An optimal operation design of photovoltaic D.C. motor coupled water pumping system. Electr. Mach. Power syst; 24(3), (1996):277-288.

WHO/UNICEF Joint Monitoring Programme, 2004.

Wolf. M, H. Rauschenbach, Series resistance effects on solar cell measurements. AIEE general meeting. Salt Lake City, Utah, August 23-25, 1963.

www.neal-dz.net

www.worldwatercouncil.org/

www.Orientalmotor.com

www.soda-is.com